Exploring the Luminescence Characteristics of Zinc Oxide Thin Films: The Role of Defects, Impurities and Metal Ad-Particles

A Scanning Tunneling Microscopy Study

Dissertation
zur Erlangung des akademischen Grades
Doctor rerum naturalium

eingereicht im
Fachbereich Physik der Freien Universität Berlin

Dipl.-Ing. Leandro Enrique Pascua Arcusin

Berlin, April 2015
angefertigt am Fritz-Haber-Institut der Max-Planck-Gesellschaft

Diese Dissertation wurde von März 2011 bis April 2015 in der Abteilung Chemische Physik am Fritz-Haber-Institut der Max-Planck-Gesellschaft unter der Anleitung von Herrn Prof. Dr. Hans-Joachim Freund angefertigt.

Gutachter:

1. Prof. Dr. Hans-Joachim Freund, Fritz-Haber-Institut der MPG
2. Prof. Dr. Katharina Franke, Freie Universität Berlin

Datum der mündlichen Prüfung: 26. Juni 2015

Dedicación

A mis maestros que en este andar por la vida influyeron con sus enseñanzas y experiencias en formarme como persona, como profesional y como deportista, preparándome para los retos que propone la vida en cada uno de estos campos, a todos y cada uno de ellos les dedico cada una de estas páginas de mi tesis.

Con todo mi cariño y amor para mis padres, Stella y Jorge, que hicieron todo en la vida para que yo pudiera lograr mis sueños, por la paciencia y el amor que dedicaron en mi camino, por transmitirme sus valores, por enseñarme el camino del deporte, de la concentración y de la constancia para alcanzar metas, a ustedes, por siempre en mi corazón, mi dedicación.

A mi hermana y compañera de la vida, Camila, por estar siempre a mi lado, por motivarme y darme la mano cuando sentía que el camino se terminaba, por sus incontables visitas, conversaciones y el tiempo compartido "de hermanos", por permitirme aprender de sus enseñanzas y transmitirme su pasión por el tango argentino, a ella, mi mejor amiga, esta dedicación.

“You can't put a limit on anything. The more you dream, the farther you get”

Michael Phelps

(American swimmer, 18 olimpic gold medals)

Abstract

Zinc oxide thin films have gained substantial interest in surface science during the last decades due to their important role in applications. In addition, zinc oxide is a unique material that exhibits semiconducting and transparence properties, making it as a promise candidate for the fabrication of optoelectronic and electromechanical devices. Two aspects are of particular interest for these applications: the structural properties and the optical luminescence. The aim of this thesis is to deepen the understanding of both properties of the ZnO oxide-film system. Particularly, the system that has been investigated is ZnO(0001) grown on gold (111) single crystals in ultra clean conditions and the main experiments were done by means of photon scanning tunneling microscopy (PSTM). Furthermore, we present the construction of a new scanning near field optical microscope (SNOM), which provides resonant light excitation and less damage to the samples. However, just the primary steps for this development are done in this thesis and no scientific question has been addressed using this technique.

The first aspect of this thesis concerns the growth modes of ZnO. Whereas a layer-by-layer growth is reveled in oxygen excess, formation of oxide nanorods with large height-to-diameter ratio prevails at lower oxygen chemical potentials. We attribute the formation of 3D nanostructures in the latter case to traces of gold atoms on the surface that promote trapping and dissociation of the incoming oxygen molecules. On the other hand, for the case of thin films growth, ZnO develops a (0001)-oriented coincidence lattice that gives rise to a well ordered hexagonal Moiré pattern with 2.2 nm periodicity, which is in turn explained by the lattice mismatch with the gold substrate beneath. The superstructure disappears at 4 ML and films thicker than 10 ML already exhibit bulk properties in terms of conductance and light emission.

The second aspect of this work provides new insights into the local photon emission of the ZnO thin films. STM-based luminescence reveals the bandgap recombination as well as sub-band-gap energies due to the presence of defects in the wurtzite lattice. To understand their nature, we systematically change the preparation conditions, e.g. by laser radiation, high temperature annealing as well as hydrogen reduction. By analysing the variation in the emission response, we assign the subgap peaks to specific zinc and oxygen defects in the lattice. Aiming to study the n-type conductivity of ZnO, we also prepare nitrogen-doped ZnO films. The intensity of the oxygen defect peak increases when growing the film at reducing conditions or inserting nitrogen into the oxide lattice. This fact suggests that not the nitrogen impurities but oxygen vacancies are responsible for the defect emission and that the nitrogen incorporation only facilitates the formation of oxygen defects.

The last part of the work concerns the modification of the optical spectra and is studied by growing and embedding silver metal particles on top of the films. The influence on both (1,0) and (1,1) plasmon resonances with focus on the shape and dielectric environment of the particles is discussed.

Zusammenfassung

Aufgrund ihrer Wichtigkeit in verschiedenen mikrotechnologischen Anwendungen stehen Zinkoxid-Nanostrukturen in den letzten Jahrzehnten im Zentrum des wissenschaftlichen Interesses. Zinkoxid ist ein einzigartiges Material mit halbleitenden und transparenten Eigenschaften, und dient vor allem der Herstellung von opto-elektronischen und elektro-mechanischen Bauelementen. Ziel dieser Arbeit ist eine Verbesserung des Verständnisses zweier fundamentaler Eigenschaften von ZnO, seiner Morphologie und Defektstruktur sowie der daran gekoppelten Lumineszenzeigenschaften. Dazu wurden ultradünne ZnO Filme auf Gold Einkristallen gewachsen und mit Hilfe eines Rastertunnelmikroskops untersucht. Zusätzlich wurde der Aufbau eines neuartigen optischen Nahfeld-Rastertunnelmikroskops (SNOM) zur optischen Untersuchung von Oberflächen entwickelt und im Rahmen dieser Arbeit präsentiert.

Der erste Aspekt der Arbeit behandelt das Wachstum von Zinkoxid-Schichten auf Au(111). Während bei Sauerstoffüberschuss ein Lagen-Wachstum beobachtet wird, bilden sich bei kleinem chemischem Sauerstoffpotential ZnO-Nanotürmen mit großen Aspektverhältnissen heraus. Der Grund für die Entstehung dreidimensionaler Strukturen liegt in der katalytischen Wirkung von Spuren von Goldatomen an der Oberfläche, welche die Dissoziieren ankommender Sauerstoffmoleküle begünstigen und das ZnO Wachstum lokal fördern. Flache Zinkoxid-Schichten wachsen hingegen in einem, dem Goldsubstrat angepassten, (0001) orientierten Wurtzit Gitter. Aufgrund einer Gitterfehlanpassung kommt es zu einer Moiré Struktur mit 2.2 nm Periodizität. Das Muster verschwindet oberhalb 4 ML Filmdicke und ab 10 ML Dicke zeigen die Zinkoxid-Filme bereits typische Volumeneigenschaften bzgl. Leitfähigkeit und Lumineszenz.

Der zweite Schwerpunkt dieser Arbeit liegt auf einer Untersuchung der lokalen optischen Eigenschaften der ZnO Dünnschichten. Mit Hilfe der STM-Lumineszenzspektroskopie konnten sowohl die Bandlücken-Rekombination bei 373 nm als auch eine Vielzahl niederenergetischer Emissions-peaks nachgewiesen werden, welche auf die Anwesenheit von Fehlstellen im ZnO Gitter hindeuten. Um ihren Ursprung zu analysieren, wurde die Probenpräparation systematisch modifiziert. Beispielsweise wurden gezielt Sauerstoff-Fehlstellen in den ZnO Filmen generiert, z.B. mittels Laserstrahlung, Hochtemperatur-Behandlung oder Wasserstoff-Reduktion. Durch Analyse der entsprechenden Änderungen in den optischen Spektren konnten somit die charakteristischen Lumineszenzpeaks für Sauerstoff- und Zinkfehlstellen im Gitter zugeordnet werden. Eine gezielte Änderung des optischen Verhaltens wurde auch durch Stickstoffdotierung der ZnO Filme erreicht. Dabei konnte ein starker Anstieg der O-Defektlumineszenz beobachtet, was einen deutlichen Hinweis auf die präferentielle Ausbildung von O-Fehlstellen bei Anwesenheit von Stickstoff im Gitter liefert.

Im letzten Teil der Arbeit wurden die optischen Spektren von ZnO durch das Abscheiden bzw. Einbetten von Silber Nanopartikeln modifiziert. In beiden Fällen wird ein deutlicher Einfluss der ZnO-Umgebung auf die orthogonalen (1,0) und (1,1) Plasmonresonanzen beobachtet, ohne dass es umgekehrt zu einer Verstärkung der ZnO-Lumineszenz kommt.

List of Symbols and Abbreviations

$\theta_i, \theta_r, \theta_t$	Incident, reflected and transmitted angle
Φ_t , Φ_s	Workfunctions of the tip and sample
E_V	Formation energy of a defect
E_i,E_F	Energy of the initial and final state
I_t	Tunneling current
L_i	Depolarization factor
U_t, U_s	Bias voltage
e^-, h^+	Electron, hole
$\vec{k}$	Wavevector $\left(\lvert\vec{k}\rvert = \frac{2\pi n}{\lambda}\right)$ of incident electromagnetic wave $\vec{k} = (k_x, k_y, k_z)$
k_B	Boltzmann constant
m_e, m_h	Effective mass of electron and hole
ε_0	Dielectric function of vacuum
ε_{Diff}	Activation energy of difussion
μ_0	Chemical potential
ρ_s , ρ_t	Density of states of sample and tip
ψ_i, ψ_f	Wavefunction of initial and final state
ω_p	Plasmon frequency
ϑ_{ext}	Optical extinction cross section
Å	Angstrom = 1x10^{-10} m
$A_\parallel$, $A_\perp$	complex amplitudes of the incident field parallel and perpendicular to the incident plane
c	Speed of light in vacuum
$\hbar$	Reduced Planck constant $\hbar = h/2\pi$
n	Optical index in medium
$R_\parallel$, $R_\perp$	Complex amplitude of the reflected field perpendicular to the incident plane
$T_\parallel$,$T_\perp$	Complex amplitude of the transmitted fields perpendicular to the incident plane
v	Velocity of light in medium
Ω	Solid angle
P	Radiated power
T	Temperature
e	Electron charge
j	Tunneling current density
m	Electron mass
p	Partial pressure
α, α_{st}	Polarizability, static polarizability
ω	Angular frequency

AFM	Atomic Force Microscopy
CB	Conduction Band
E_F	Fermi Energy
FER	Field Emission Resonance
HE	Hot Electron
IET	Inelastic Tunneling
IETS	Inelastic Electron Tunneling Spectroscopy
IRAS	Infrared Reflection Absorption Spectroscopy
LCD	Liquid Crystal Display
LDOS	Local Density of States
LEED	Low Energy Electron Diffraction
LN_2	Liquid Nitrogen
MEMS	Micro Electro Mechanical Systems
ML	Monolayer
NFO	Near-Field Optics
OLED	Organic Light-Emitting Diode
PSTM	Photon Scanning Tunneling Microscopy
RF	Radio Frecuency
SNOM	Scanning Near-Field Optical Microscopy
SPM	Scanning Probe Microscopy
STM	Scanning Tunneling Microscopy
STS	Scanning Tunneling Spectroscopy
TFT	Thin Film Transistors
TIP	Tip Induced Plasmons
TSP	Titanium Sublimation Pump
UHV	Ultra-High-Vacuum
VB	Valence Band
VLS	Vapor Liquid Solid
XPS	X-Ray Photoelectron Spectroscopy
ZnO	Zinc oxide

Contents

Chapter 1

Introduction and Motivation

"Over the history of computing hardware, the number of transistors in a dense integrated circuit doubles approximately every two years" [1]. Well known as Moore's law, it was empirically formulated in 1975 and the trend is kept until present times, thanks to the advances in nanotechnology and the availability to produce smaller transistors with higher densities. With the invention of the field-effect transistor, thin film oxides turned to play a key role in this trend, as they demonstrated their importance for reducing dimensions and production costs of such devices.

The general importance of oxides, however, goes beyond electronic applications. Also the fields of catalysis, micro electro mechanical systems (MEMS) and optics benefit from oxide properties. Particularly interesting is the field of heterogeneous catalysis, where oxides are used to stabilize small metal particles as the chemically-active species [2]. Oxides do not only act as passive substrates, but also actively influence the chemical performance of the catalyst [3, 4]. Depending on the film thickness, oxide layers can either act as reasonable models to mimic the situation of bulk materials or exhibit properties in their own right [5]. In particular, ultrathin oxide films of 1-3 ML thickness develop properties that are unknown for bulk materials. In spite of the many advantages in terms of applications, oxides materials exhibit difficulties to be analyzed, as they have low conductivity and complex morphology. Nevertheless, the introduction of model systems, such as clean oxide surfaces, helps to overcome this barrier [6]. Typically, this is done via an *ex situ* cutting and polishing of the bulk single crystal followed by an *in situ* treatment by sputtering and subsequent annealing in ultra-high-vacuum (UHV) environment. Through such a process, a sufficient number of defects is created in the near surface region and in the bulk to promote conductivity of the material, as for example on TiO_2. As a result, electron spectroscopies as well as STM can be applied [7, 8]. Surface science tools like scanning tunneling microscopy (STM) [6], X-ray photoelectron spectroscopy (XPS) [9, 10] and infrared reflection absorption spectroscopy (IRAS) [11, 12] have already demonstrated their ability to study oxide surfaces.

However, even model systems are not perfect, as native lattice defects, interstitial atoms, step edges, particles of different sizes and molecules are present on the surface, making the system inhomogeneous [13]. Definitely, the role of these defects needs to be investigated in a local way and therefore a tool with outstanding spatial resolution is needed, such as the scanning probe techniques [14, 15]. STM methods are hereby suited to probe two fundamental properties at once, the oxide morphologies and their related electronic structure.

Oxides are also recognized as excellent materials for photocatalysis due to their high photosensitivity, non-toxic nature and suitable band gaps in the visible region. Also the optical properties of oxides are inhomogeneous and should be probed with high spatial resolution. New local optical sensitive approaches are therefore needed. In my thesis,

two approaches have been used to explore the local optical properties of oxides. The first one is the established Photon-STM method, as described already in [16-18] and the other one is the scanning near field optical microscopy (SNOM) [19-21]. The second concerns a completely new setup, which brings many advantages with respect to the Photon-STM, for instance in terms of light excitation. It is a purely optical method that permits resonant excitation, control of the polarization of light and is, in addition, nondestructive. In chapter 3 of my thesis, I will describe how a SNOM-setup was planned and later constructed. Although some first results were obtained, the setup is not yet fully functionable and no scientific questions have been addressed so far. The main experiments in this thesis were therefore performed with the Photon-STM, exploring the properties of ZnO thin films.

By exploiting the advantages of oxides, thin film transistors (TFTs), a type of the field-effect transistors mentioned at the beginning, provide a common and inexpensive method of adressing individual pixels in LCD and OLED displays [22]. Particularly, high electron mobility and visible transparency make zinc oxide (ZnO) thin film transistors an attractive alternative to the classical amorphous silicon TFTs [23-25]. Acting as support material for high-*k* dielectric layers in these transistors, ZnO offers a large bandgap, which leads to a desired level of transparency of the transistor itself. Thus, knowledge on the relation between optical and structural properties of ZnO is desired and its acquisition has been the main topic of this PhD work. It is known that the optical response of wide bandgap oxides such as ZnO is connected with the presence of imperfections in the crystal lattice, e.g. lattice vacancies or interstitial sites [26-28]. These imperfections exhibit pronounced spatial variations across the surface. Structural defects play an important role in the luminescence, as they act as trapping centers for excitons (electron-hole pairs) that recombine later via the emission of photons with specific energies. So far, correlation between the various defect types on the surface and their optical activity in ZnO is only based on non-local optical measurements on powders or single crystals and model calculations [29-31]. Typically, they rely on the comparison of measured and calculated photon energies [26]. As a consequence, local structural and optical information is needed to verify this assignment on a completely experimental base, which is in turn feasible by means of emission spectroscopy with the STM. Finding a correlation between surface optical and structural properties in (0001) terminated ZnO surfaces is the main goal of this PhD work.

Chapter 2 provides a brief overview over the theory and working principle of both local techniques: STM and SNOM. The mechanisms that provide light emission in a STM tip-sample junction and the plasmons in metal particles are described. Details of both experimental setups employed in this PhD work are presented in chapter 3. The first steps of the construction work during my PhD period are presented. Chapter 4 of this thesis concerns the experimental data and the scientific discussion of ZnO thin films. The preparation and growth morphology of ZnO model systems is discussed, putting special emphasis on the possibility to grow either flat or nano-structured oxide films. The experiments aim at generating a correlation between the surface morphology, defect landscape and optical luminescence of differently thick ZnO films grown on a Au(111) single crystal. In addition, the interaction of ZnO substrates with metal particles is treated from the plasmonic point of view at the end of the chapter. Finally, a summary and outlook section is given in chapter 5.

Chapter 2

Theoretical Background

2.1 Scanning Tunneling Microscopy

The technique of scanning tunneling microscopy is considered nowadays as one of the most interesting methods for the analysis of solid surfaces. The main reason lays in its ability to explore the surface of solids in real space and at atomic scale at the same time. It is mainly based on the tunneling effect of a quantum particle through a potential barrier, which was invented with the advent of quantum mechanics in the early years of the 20th century. The method was first developed by Binning and Rohrer in 1982 and has been awarded with the Nobel Prize in 1986 together with Ernst Ruska (electron optics and first electron microscope)[32]. In the present, a variety of different versions exists, which are able to go into detail of different sample properties. In addition to the topographic information, the method also provides the possibility to locally probe the conductance of the surface or of adsorbed species. This possibility is achieved via the method of scanning tunneling spectroscopy (STS) [33-35]. Moreover, Inelastic Electron Tunneling Spectroscopy (IETS) provides a tool to investigate the vibrational properties of molecules on surfaces or the surface itself [36-39]. Furthermore, magnetic domains, Kondo systems and even spin orientation of surface atoms can be studied by means of Spin Polarized STM [40-43], which applies magnetic fields and introduces magnetically polarized tips. Also non polarized STM is used to get information on superconducting and magnetic effects [44, 45]. The STM tip can furthermore be used for the manipulation of the spin state, the conformation of molecules and the lateral arrangement of surface atoms. Also artificial structures can be constructed by manipulating the position of adsorbates in order to get insight into the quantum-mechanic nature of such systems.

The STM is widely known due to the broad range of regimes in which it can be used, e.g. in Ultra High Vacuum (UHV), air or solutions. In addition, the range of operating temperatures is very broad ranging from 1300K [46] to liquid nitrogen, liquid helium regimes, down to a few mK [47, 48]. This powerful tool is used in many kinds of scientific disciplines, e.g. surface science, material science, biology or nano-electronics.

The quantum-mechanical effect of electron tunneling was first described by Gurney and Gordon in 1928. This effect represents the fundamental basis of the STM [49]. Figure 2.1 shows the one dimensional tunneling effect. Here, the electron is described by its wavefunction and penetrates an energy barrier of the height ϕ. In contrast to the classical case, in which the electron is reflected as long as its energy E is smaller than the barrier height, there is now an exponential decay of the quantum-mechanical wavefunction into the barrier. Thus, the electron has a non-zero probability to be transmitted even for $E < \phi$. The STM takes advantage of this effect, so that an atomically sharp metal tip is approached to a conductive or semi-conductive surface to distances, in which tunneling becomes feasible. This principle can achieve distances of a

few Å, which may imply an applied voltage to the junction and a measurable tunneling current in the range of *p*A to *n*A.

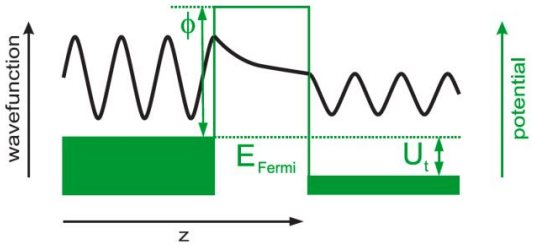

Figure 2.1. A one-dimesional tunneling junction. The electron is reflected at the potential step on the left side. However, the corresponding wavefunction exhibits an exponential decay inside the barrier. This leads to a non-zero wavefunction on the right side of the barrier. Adapted from [50].

In a first and very simple consideration, the tunneling current can be described as being proportional to the exponent of the distance d:

$$I_t \propto U_t \exp\left(-2\sqrt{\frac{2m\Phi}{\hbar^2}}\, d\right) \tag{2.1}$$

with U_t representing the bias voltage and Φ the work function. The work function Φ of a metal surface is defined as the minimum energy required to remove an electron from the bulk to the vacuum level. In general, the work function depends not only on the material but also on the crystallographic orientation of the surface [35]. The exponential decay is the main reason of the high sensitivity of STM in the *z*-direction (see Figure 2.1) [51].

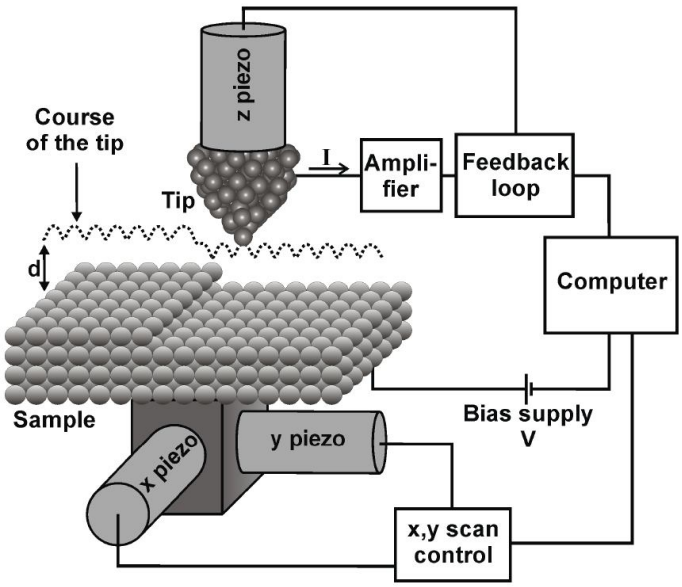

Figure 2.2. Schematic representation of the principle of STM. The *x*- and *y*-piezo's are responsible for the line-by-line scanning. The tip reproduces the sample topography by changing the distance, which is mainly done by the *z*-piezo. The feedback-loop controls the tip-sample separation [51].

The piezo electric crystals (piezo's) help to produce a three dimensional image of the surface. Thus, the sharp tip is scanning line by line. There are two modes of operation used to acquire topographic data. In the *constant height* mode, the I_t signal is plotted versus the *x*- and *y*-coordinates. The height of the tip does not change in this mode, which leads to rather fast scanning up to video frequencies [52]. This is useful to study dynamic processes such as film growth or diffusion on surfaces [53, 54]. On the contrary, heavily corrugated samples cannot be scanned because it could lead to tip damages. Nevertheless, the *constant current* mode is more appropiated for corrugated surfaces. In this case, the tip is prevented from damages at the price of larger acquisition times. The *z*-displacement carries the information to create the image by keeping the distance evolution between tip and sample. The distance changes constantly during scanning because the feedback-loop controls the z-piezo in such a way, that the current signal is equal a pre-set value. Therefore, the tip follows the topography of the surface. The *constant current mode* was particularly used in this work.

2.1.1 Theoretical Considerations of STM

The exponential dependence of the tunneling current on the tip-sample distance is the main basis of the STM, as described in equation (2.1). However, this expression is not descriptive enough for an exact representation of the real experimental situation. It does not take into account several important parameters such as the electronic states in tip and sample, the tip geometry or the existence of inelastic tunnel interactions. Thus, several models have been developed that take into account these parameters. Nevertheless, an exact theoretical description would be extremely hard and would require a permanent improvement of these models.

In 1961, Bardeen *et al.* developed one of the first and more widely used models to describe tunneling processes [55]. The one dimensional perturbation theory was used to describe a layer system, which consists of two metal electrodes separated by an insulator. The two independent electrodes on both sides of the barrier (insulator) are described by their overlapping eigenfunctions. The transition probability from an initial state $|i\rangle$ on one side to a final state $|f\rangle$ on the other side is calculated in the presence of a small perturbation of the potential. The Fermi's Golden rule gives the transition probability:

$$w_{i,f} = \frac{2\pi}{\hbar} \left|M_{i,f}\right|^2 \delta\left(E_i - E_f\right) \tag{2.2}$$

with the transition matrix:

$$M_{i,f} = -\frac{\hbar^2}{2m} \int \left(\psi_f^* \nabla\psi_i - \psi_i \nabla\psi_f^*\right) d\vec{S}\,, \tag{2.3}$$

where the integration is done over an area between tip and sample electrode and ψ_i and ψ_f are the wavefunctions of initial and final state in tip and sample, respectively. In the case of small voltages and a temperature of 0*K,* the Fermi-Dirac distribution $f(E)$ is described by a step function. Thus, the tunnel current is described by the following expression:

$$I_t = \frac{2\pi}{\hbar}\, e^2\, U_t \sum_{i,f} \left|M_{i,f}\right|^2 \delta(E_i - E_F)\ \delta\left(E_f - E_F\right) \tag{2.4}$$

where E_i and E_f are the energy of the initial and final state, respectively, E_F stands for the Fermi energy and $\delta(E)$ is the Dirac's delta function.

The first steps in understanding the STM from a theoretical point of view were done by Tersoff and Hamann [56, 57]. After adapting the approach of Bardeen, the three dimensional approach was considered by modelling the STM tip with a spherical potential with only *s*-like eigenfunctions. The tunnel current is proportional to the convolution of the local density of states (LDOS) of the sample at the position of the tip. Following the Wentzel-Kramers-Brillouin (WKB)-approximation, I_t is described by:

$$I_t \ \propto \int_{-\infty}^{+\infty} \rho_s(E)\rho_t(E - eV_s)T(d, E, eV_s)\ [f(E - eV_s, T) - f(E, T)]\ dE\ . \tag{2.5}$$

ρ_s and ρ_t represent the density of states of sample and tip, respectively and the transition probability is given by:

$$T = \exp\left(-2d\ \frac{\sqrt{2m}}{\hbar}\ \sqrt{\frac{\Phi_s + \Phi_t}{2} + \frac{eV_s}{2} - E}\right), \tag{2.6}$$

which depends on the tip-sample separation d, the workfunctions of the tip Φ_t and sample Φ_s and the applied potential eV_s. Assuming the same conditions mentioned above (small bias and 0*K*), the formula (2.5) is simplified to:

$$I_t \ \propto \int_0^{eV_s} \rho_s(E)\ \rho_t(E - eV_s)\ T(d, E, eV_s)\ dE\ . \tag{2.7}$$

This last equation implies that in the case of constant current mode the observed corrugation is the plane of constant integrated LDOS on the surface. This is used as the starting point for the interpretation of STM data. This also stresses the fact that the observed topography does not only come from purely geometric facts but from a convolution of both geometric and electronic contributions.

2.1.2 Light Emission in STM

In this work, the main advantage of the STM concerns its ability to perform electronic and optical spectroscopies with high lateral resolution. This ability allows local investigations of optical properties on the nanometer scale (single atoms and molecules) [58-60]. In fact, light emission from a STM junction was observed in different experiments. Nevertheless, the spectral distribution and the intensity of the emitted light do not only depend on the properties of the sample, as classical optics predicts. Indeed, the material and the shape of the STM tip turned out to be decisive for the measurements as well [61].

Light emission from an STM junction is generated by tunneling electrons, which loose part of their energy within the junction. Two main possible mechanisms can cause photon emission of a tunneling electron: *(i)* inelastic tunneling (IET), where the energy of the electron is released in the region between tip and sample and *(ii)* hot electron decay (HE), where the photon is emitted due to electron recombination just

after the tunneling process, i.e.: inside the band gap of the sample material. Figure 2.3 depicts the two situations [34, 51].

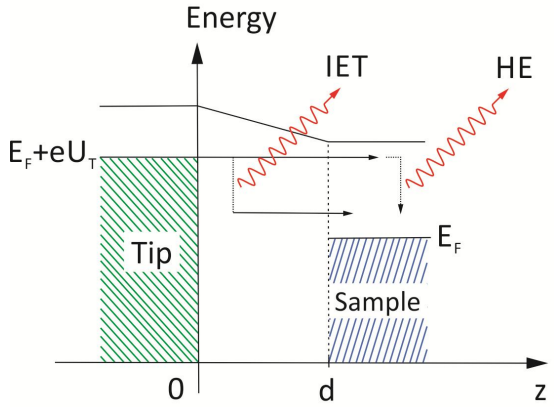

Figure 2.3. Two possible mechanisms for photon emission from a STM junction. IET: Inelastic tunneling and HE: Hot electron decay

The probability of the IET and HE processes in the STM junction determines the intensity and quantum yield of the emitted radiation [34, 62]. However, the inelastic currents make only a very small contribution to the total tunneling current and the associated photons are therefore difficult to detect. The photon yield is also dependent of the degree of coupling between the tip and sample, which in turn is governed by the dielectric properties of the tip and sample materials. IET is predominant in metal-metal junctions where excitations of the free-electron gas take place. On the other hand, HE decays are found to be responsible for light emission from semiconductor and oxide surfaces as well as from single molecules [34].

The detection of optical information can help to compensate for the lack of chemical sensitivity of STM in some cases. Even though Scanning Tunneling Spectroscopy (STS) can probe the LDOS, which would be another possibility to obtain chemical information, STM-Luminescence spectroscopy allows to investigate the unique optical properties of chemical species. The local optical transitions can be compared to a broad amount of optical data, which may extend the knowledge on the electronic structure of an adsorbed species. The main reason lies on the correspondence of the energy of the emitted photons with the intrinsic electronic transitions of specific elements or compounds. This interplay between electronic and optical data was known already in the nineteenth century. Nevertheless, it was first in 1950 when a more specific use came up by using chemical analysis techniques like atomic absorption spectroscopy (AAS) [63, 64].

Lambe and Mc Carthy first observed light emission from a tunnel junction (metal-oxide-metal) in 1976 [65]. But it was only in 1988 when light emission from STM was observed for the first time. The work was done by Gimzewski *et al.* using a Ta tip on Si(111) surface [66]. These experiments served as a starting point for a deeper investigation of mechanisms that induce the light emission in STM. A typical bias dependence of the integrated photon intensity from a STM junction is shown in Figure 2.4. It is evident that both parameters, the applied bias and the tip-sample separation, are decisive for the collected light emission. At smaller distance (small bias), the photon intensity suddenly increases, reflecting the strong interaction between tip and sample

at distances much smaller than the emitted wavelength. On the other hand, long acquisition times are necessary when working at high bias due to the small intensity collected [34].

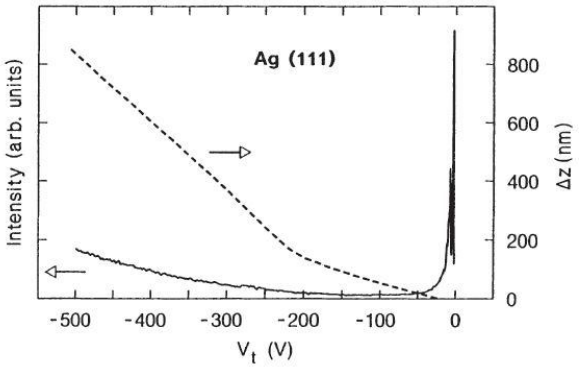

Figure 2.4. Light emission intensity in function of the voltage applied to the STM tip (left, bold line). The dashed curve on the right represents the associated tip sample distance [50].

An energetic electron impinging on a metal surface can produce electromagnetic radiation in three different processes: *(i)* initiation of radiative inter-band transitions, *(ii)* surface plasmon excitations and *(iii) bremsstrahlung*. The contribution of the last process is significant for $|V_t| \geq 250V$ as it can be appreciated in the exponential shape of the black curve in Figure 2.4. The voltages used in this work are below this value, so that the cross section of *bremsstrahlung* turns to be small. Therefore, its contribution is neglected.

The remaining two mechanisms influence the light emission in a tunnel junction in a strong way, as it has been studied in the last 20 years. Inelastic tunneling between tip and sample can activate optical modes in the junction, as the electron energy is transferred to this mode. In addition, the electron beam from the tip, which is spatially confined, may act as a source for cathodoluminescence. In this case, the optically active mode is located directly at the surface.

The issue of the photon intensity plays an important role in both cases. The usual quantum efficiency for these processes is in the range of 10^{-11} photons per electron. This value is close to the detection limit, even for classical luminescence experiments. Nevertheless, photon emission from a silver covered Si substrate investigated with an Ir tip was first observed by Gimzewski *et al.* in 1989 [67]. Two experimental facts were to be distinguished. First of all, there was a cutoff wavelength $\lambda_c = hc/eV_t$ in the spectral distribution of the emitted light when increasing the excitation bias eV_t. Secondly, for voltages $V_t \geq 3V$ the energetic position of the peak did not change any more. With these two facts, the authors concluded that the light emission was caused by an inelastic excitation at exactly this energy. Later, Johansson *et al.* confirmed their idea [68].

As long as the tip is in close proximity to the surface, the probability that plasmon modes are excited by inelastic electron tunneling is rather high. Also radiative decay of hot electrons is likely to occur. Whereas collective electron excitations (plasmons) are preferentially found in materials in which electrons can move with low difficulties, for example in metals, the exciton recombination (electron-hole pairs) is limited to band-

gap materials, like semiconductor or oxide materials. However, the rather high photon intensities are not only due to these emission mechanisms. Quantum efficiencies of 10^{-5} to 10^{-3} photons per electron are also possible. They are related to field enhancement effects. These enhancement effects are developed in the cavity composed of tip and surface. The interpretation of Tip Induced Plasmons (TIP) explains this enhancement issue. This theory was first proposed by Johansson [68] and will be further described in the next paragraph.

2.1.3 Tip Induced Plasmons (TIP)

Before the following concept was introduced, the preferred explanation for light emission was the radiative decay of surface plasmons, which were excited by tunneling electrons [65, 69]. In that case, the conservation of parallel momentum allows radiative de-excitation only if the surface translational symmetry is broken, i.e. by surface roughness or imperfections. In the model described by Johansson *et al.* [61] the symmetry reduction is realized by the tip. An antenna effect was also considered, as the geometry of the tunnel junction can provide an electric field enhancement.

Johansson in his model separated the calculation of the emitted light intensity from an STM into two parts. First, the electric field in the cavity formed by the tip in close proximity to the surface, is determined. This electric field results only from electromagnetic coupling between the two electrodes and requires no current. This is achieved in the non-retarded approach, which fits with a basic picture of the mechanism. Secondly, the variation in the tunneling current is considered as the source of excitation. The experimental results confirmed the theoretical predictions in many cases. More recent explanations were developed, which explain some particular experimental data, for instance the emission of polarized light due to asymmetric tips, in a better way [70, 71].

In the first part of the Johansson calculation, the electric field $E(\vec{r},\omega)$ is considered in large distance between sample and tip. The reciprocity theorem of electrodynamics is then connected to the induced field $E_{ind}(\vec{r},\omega)$ and the tunneling current density $j(\vec{r}',\omega)$ by the following expression:

$$E(\vec{r},\omega) = \frac{1}{j_0}\int E_{ind}(\vec{r},\vec{r}',\omega)\, j(\vec{r}',\omega)\, d^3r \ , \tag{2.8}$$

where the right term represents the electric field $E_{ind}(\vec{r},\vec{r}',\omega)$ at the position of the tip. This results from a delta-shaped current density $j_0\delta(\vec{x}-\vec{r})$ below the tip. Figure 2.5 illustrates the situation [33, 50, 61].

E_{ind} comes from solving the Laplace equation of electrodynamics taking into account the geometrical and the material properties of the tip. The expression of the current density $j(\vec{r}',\omega)$ in equation (2.8) can be defined by:

$$j(\vec{r}',\omega) = -i\,\frac{e\hbar}{2m}\left(\frac{\partial\psi_f^*}{\partial z'}\,\psi_i - \psi_f^*\,\frac{\partial\psi_i}{\partial z'}\right)(\vec{r}') \tag{2.9}$$

in which ψ_i and ψ_f are the initial and final states in tip and sample, respectively. After inserting this expression into equation (2.8) it turns to:

$$E(\vec{r},\omega) = \frac{\omega}{c^2}\frac{e^{i\vec{k}\vec{r}}}{\vec{r}}\frac{e\hbar}{2m}\int G(\vec{r}',\omega)\left(\frac{\partial\psi_f^*}{\partial z'}\psi_i - \psi_f^*\frac{\partial\psi_i}{\partial z'}\right)d^3\vec{r}' \quad . \tag{2.10}$$

In a very simplified frame, the tip induced plasmon can be considered as the coupling of the surface plasmon in the tip and the sample surface. However, this model is only valid for the case that the two electrodes are close to each other. This is the case of a tunnel junction, in which the distances between tip and sample are in the range of 5-10 Å. Then, these interactions are rather strong and the model is adequate. In a more general view, these field enhancement effects are normally appreciated when die dimensions of the junction are in the range of the wavelength of light.

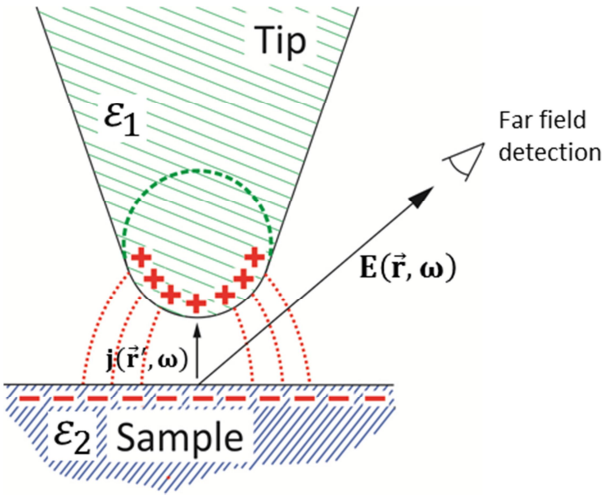

Figure 2.5. Schematic view of the model used by Johansson *et al.* used to obtain the electromagnetic field distribution inside the junction

As defined by Johansson et al. [62], the total radiated power, which is the intensity of photon emission per unit solid angle Ω and unit photon energy as measured by a far-field detector is then:

$$\frac{d^2P}{d\Omega d(\hbar\omega)} = 2c\varepsilon_0\sum_{i,f} r^2|E(\vec{r},\omega)|^2\,\delta\big(E_i - E_f - \hbar\omega\big), \tag{2.11}$$

where $E(\vec{r},\omega)$ was already defined in equation (2.10), ε_0 and c are the dielectric function and the light velocity in vacuum, respectively. Note again the δ-function including $\hbar\omega$ for the inelastic electron loss.

2.1.4 Field-Enhancement Effect

The enhancement function $G(\vec{r}',\omega)$, which is found in equation (2.10), shows a strong dependence on the dielectric functions of tip and sample and the geometry of the junction. This function can be found by solving Laplace's equation for the electrostatic potentials induced at the tip and sample with the correspondent boundary conditions [62, 72]. The enhancement factor G for a junction is calculated by replacing the far field

detector with an hypothetical far field source in Fig. 2.5 and is and represented in Figure 2.6b. These curves correspond to the case of an iridium tip and a silver bulk sample for different tip radii. The Ir tip is modelled as a sphere [72]. The factor G increases proportional to the tip radii. This effect is due to the polarizability of the cavity. The enhancement shows a drop for energies above 3.5 eV, which is mainly caused by the decoupling of the tip and sample electron gases. Exactly at this energy the real part of the dielectric function of silver reaches a value of -2. This represents the condition for the plasmon resonance in a Ag sphere in the quasi-static regime (see section 2.1.6, equation (2.12) [73]. The coherent collective electronic excitation (plasmon) vanishes due to the decoupling of the Ir sphere from the Ag sample. The strong influence of the Ag sample on the enhancement function G is demonstrated by this fact. The imaginary part of the complex dielectric function $\varepsilon(\omega)$ dominates the structure of G in the junction. In the case of noble metals, this imaginary part is rather small, which means lower damping in the material and intense light emission.

The spectral distribution of the G function is shown in Figure 2.6b as a function of the sample bias. The energy of the highest initial state of the electron in the tip limits the maximum energy of emitted photons. All possible radiative transitions between $E_i = E_F + eU_s$ and $E_f = E_F$ in equation (2.11) are contained in the emitted light. For values of U_s between 1.5V and 3.5V a fast increase of the light intensity is observed. The increasing number of decay channels involving transitions at around 2.5eV is responsible for the increase of light intensity due to the maximum of G at that point. For sample voltages above 4V the intensity decreases again. This decrease is due to an enhanced tip-sample distance, which turns bigger in order to keep the tunneling current constant. Therefore, the electromagnetic coupling across the junction is reduced. As a consequence, the field enhancement G and thus, the emitted light strength follow the inverse of the tip-sample distance, as seen in Figure 2.6a [62].

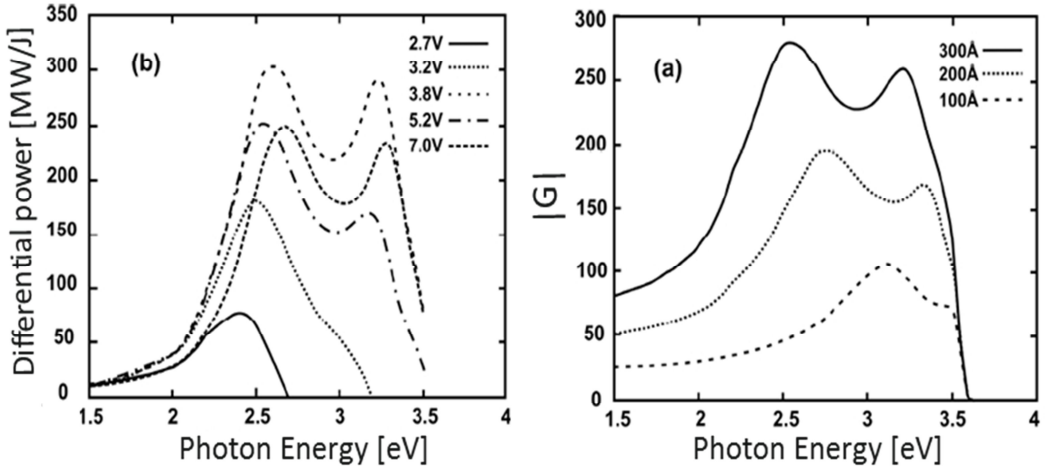

Figure 2.6. Enhancement characteristics for a tip-sample junction: Ir tip and Ag sample. (a) Dependence of emission power on sample bias. As higher bias leads to larger tip sample distance, there is a maximum for 3.8 V. The radiated power is obtained for a tip radius of 300Å and tunneling current I=300nA, as function of sample bias U_s. (b) Dependence of the field enhancement on the tip radii [62]

2.1.5 Tip-Metal Particle Junction

In 1992 Persson and Baratoff developed a model, which allowed to calculate the probabilities of competing radiative and non-radiative processes inside a metallic particle [74]. The model assumed tunneling from an s-like orbital at the apex of the tip to a spherical free-electron like metallic particle. If the tunneling electron excites the dipole plasmon resonance of the metallic particle, enhanced emission takes place. On the contrary, direct processes like radiation-band-transition were found to be rather low. Dipolar plasmon excitations are described in Figure 2.7. Inelastic tunneling processes have a relative high probability ($\approx 10^{-2}$) due to the large magnitude of the dipole moment associated (Figure 2.7a). This probability is, however, still low compared to elastic tunneling (≈ 1) but clearly dominates over the excitation via hot-electron decay ($\approx 10^{-4}$) (Figure 2.7b). Dipole resonances have two possibilities to decay once they are excited: *(i)* into electron-hole pairs (≈ 1) or *(ii)* via photon emission ($\approx 10^{-1}$). After applying extended probabilities, inelastic tunneling produces a photon with $P \approx 10^{-3}$ and hot electron decay happens only with $P \approx 10^{-5}$. This is in reasonable agreement with experimental photon emission intensity of Ag granular films [74].

The tip has also an effect in the plasmon resonance of the metallic particles. The coupling with the free-electron gas of the tip increases the particle polarizability and therefore shifts the plasmon frecuency to lower frequency. The amount of shift depends on the tip-sample coupling strength [75].

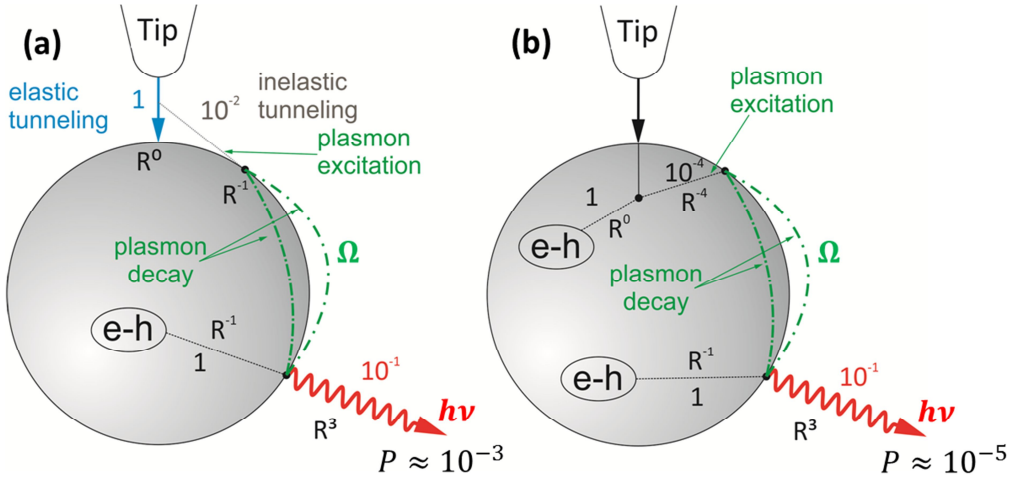

Figure 2.7. The picture indicates the branching probabilities for both excitation processes: (a) inelastic tunneling and (b) hot electron decay. *P* indicates the probability of radiative decay in both cases.

2.1.6 Plasmons in Metal Particles

Metal particles show interesting optical properties, which in many cases differ from the ones of the bulk. These properties come from collective oscillations of conductive electrons inside the particle. These collective oscillations are called *Mie plasmons* [73]. When the electromagnetic waves interact with the particle, two regimes can be distinguished, depending on the particle size. The first one is the so called *quasi-static*

regime. This regime is characterized by the condition that the excitation wavelength is much larger than the particle radius, which means that $\lambda \gg R$. In case of excitation, the volume of the particle is homogeneously polarized. The particle is only affected by the time dependence of the field but not by the spatial dependence. Under these conditions the excited plasmon mode is a dipole. In the other regime, in which the condition $\lambda \leq R$ is satisfied, the electromagnetic fields are modulated inside the particle. As a result, multipolar polarization and retardation effects are observed, which lead to higher plasmon modes [73].

The Mie Theory describes the optical response of small metal particles in the quasi-static regime [73, 76]. It gives an accurate representation of the optical extinction spectra of a single sphere of a given material. By solving Maxwell's equations, this theory finds adequate functions for the electromagnetic fields. It considers the size and shape of the particle, its dielectric function $\varepsilon(\omega)$ and the function of the embedding medium ε_m.

In the case of a spherical particle with radius R, the polarizability is described by the following expression [73]:

$$\alpha = \alpha_{st} \frac{\varepsilon(\omega) - \varepsilon_m}{\varepsilon(\omega) + 2\varepsilon_m} , \tag{2.12}$$

in which α_{st} stands for the classical static polarizability of a metal sphere and takes into account the radius and the vacuum dielectric constant:

$$\alpha_{st} = 4\pi\varepsilon_0 R^3 . \tag{2.13}$$

Thus, the optical extinction cross section ϑ_{ext} can be introduced and then related to the polarizability through:

$$\vartheta_{ext} = k\, Im\{\alpha\} + \frac{k^4}{6\pi} |\alpha|^2 , \tag{2.14}$$

where k is the wave vector defined by $k = 2\pi/\lambda$, $Im\{\alpha\}$ and $|\alpha|^2$ represent the imaginary part and the square modulus of the polarizability, respectively [77].

The light absorption is described by the first term of equation (2.14). This term is also connected to electron energy losses. The second term, on the other hand, represents losses caused by scattering. The frequency at which the strongest absorption is observed corresponds to the Mie plasmon. This situation takes places when the denominator in equation (2.12) turns to zero, which means $\varepsilon(\omega)/\varepsilon_m = -2$. In a first calculation, only the real part of $\varepsilon(\omega)$ is considered to obtain the frequency of the Mie plasmon [73].

Equation (2.12) shows the isotropic polarizability of a spherical particle. This equation presents a single optical absorption peak. However, there is a three-fold degeneracy of the corresponding Mie mode. This degeneracy is lifted due to the loss of isotropy in the particle's polarizability. Figure 2.8 shows a spherical particle on a substrate, in which the symmetry of the medium is broken. The polarized sphere induces image dipoles in the substrate that couple via Van der Waals's forces and produce anisotropy in the particles' polarizability. Evidently, the coupling is different along the *z*-axis than in the (x, y) plane. Whereas the dipole-dipole interaction is destructive parallel to the surface plane, it is constructive in the perpendicular direction (*z*-axis). Therefore, the coupling increases the perpendicular polarizability, but reduces

the parallel one. The result is two different Mie plasmon modes. According to the (L, m) representation for spheroids, the plasmon modes are defined as $(1,0)$ and $(1,1)$ and are assigned to be perpendicular and parallel to the surface, respectively. L represents the order of multipoles, and $L = 1$ is the case for dipole modes. Depending on the value of L, there are $L + 1$ *eigenmodes* associated, assigned with the magnetic quantum number m [73]. The particle polarizability is related to the plasmon resonance ω_p by the following reduced expression:

$$\omega_p^2 = \frac{Ne^2}{m_e\, \alpha_{st}}\ , \tag{2.15}$$

which shows an inverse relationship between them. Here m_e stands for the electron mass, N the number of conduction electrons and α_{st} the static polarizability.

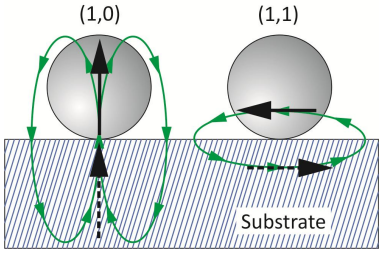

Figure 2.8. Induced image dipoles in the substrate caused by interaction of (1,0) and (1,1) dipole modes. Perpendicular interaction strengthens the (1,0) mode and increases the total polarizability (left). In plane interaction weakens the (1,1) mode and decreases the total polarizability (right).

However, there is a second issue related to metal clusters supported on solid substrates. Wetting effects give rise to intricate cluster shapes and play an important role in the optical absorption. Surface energy causes metal clusters deposited on a dielectric substrate to form regular oblate ellipsoids with varying axial ratios. This effect was studied by Royer *et al.* [78, 79] and shows the (1,0) mode shifted to the blue and the (1,1) mode shifted to the red sides of the spectrum (Fig. 2.9).

The geometrical depolarization factors L_i determine the shape of the ellipsoid, with $i = a, b, c$. Only two of the three are independent, as the sum rule $\sum L_i = 1$ applies. Thus, a general ellipsoid with three different axes has $L_a \neq L_b \neq L_c$. For these particles the electric polarizability α_i is described by:

$$\alpha_i = \varepsilon_0\, \frac{\varepsilon(\omega) - \varepsilon_m}{\varepsilon_m + [\varepsilon(\omega) - \varepsilon_m]\, L_i}\, V_{cluster}\ , \tag{2.16}$$

where $V_{cluster} = (4/3\,\pi)\, abc$ represents the cluster volume.

The angle formed between the polarization vector of the wave and the principal axis i is decisive for the response of the polarizability to an incoming electromagnetic wave. This can be seen in the denominator of equation (2.16). The aspect ratio c/a, where $a = b > c$ or $a = b < c$ (oblate or prolate shape, respectively), is the key parameter for the polarizability of the particles. The depolarization factor along the principal axes depends strongly on the aspect ratio [80]. A decrease of the aspect radio heads to an increase of L_c and to a decrease of L_a and L_b when changing from a sphere to an oblate cluster. Hence, the (1,0) and (1,1) plasmon modes of the particle are blue-

and red-shifted, respectively. This mode shift follows the same direction with a decrease of the aspect ratio.

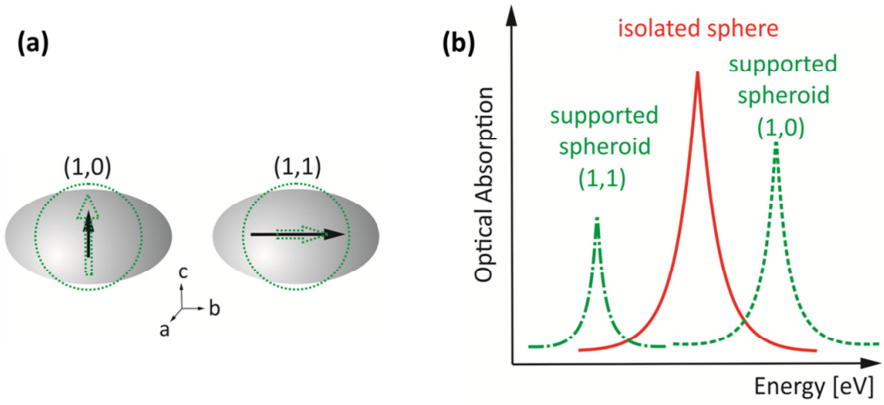

Figure 2.9 (a) (1,0) and (1,1) dipoles in an oblate cluster in comparison with the ones of a spherical particle. (b) Optical absorption cross section for an isolated and a supported spheroidal particle. Note the red and blue shift of the (1,0) and (1,1) modes, respectively, caused by the increment of the polarizability along the axes *a* and *b* and a correspondent reduction in axis *c*.

In addition, more effects on plasmon positions are observed when a spherical particle is present in an environment of more particles. The interparticle dipole-dipole interaction is one of the reason for this effect. This type of interaction depends strongly on the particle-particle distance. Figure 2.10 shows the different types of couplings that depend on the plasmon modes [51]. The polarizability increases along the particle axis and decreases perpendicular to it. Two new different plasmon modes result from this coupling [73].

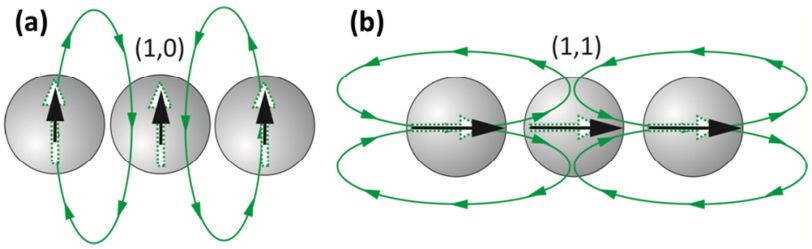

Figure 2.10. Schematic of dipolar couplings in a chain of particles: (a) destructive coupling in the (1,0) mode and (b) constructive coupling along the chain. The green dotted arrow filled with white depicts the dipole strength corresponding to the isolated particle.

In addition, more interaction mechanisms should be taken into account to analyse the optical behaviour of a realistic particle system. The spatial distribution of particles of the surrounding medium does also play a key role. Several models have been already developed, like the Maxwell-Garnett model [73], which allows a good understanding of the optical behaviour of real systems.

To sum up, three factors are decisive for the photon emission from metal-metal junctions which support tip induced plasmons: *(i)* the density of states of tip and sample, which determines the inelastic tunneling current, *(ii)* the dielectric function of the tip and sample materials that provides the field enhancement, and *(iii)* the geometry of the junction in which the tip shape plays a key role. For an isolated surface

without tip, the decisive parameters are: *(i)* the particle shape (depolarization factor L_i), *(ii)* the coupling between particles and support, and *(iii)* the interparticle coupling (ensemble effects).

It becomes obvious that more details of the tip shape enable a better and more precise description of the radiation features of an STM cavity. In the literature, the authors make use of the boundary charge method [72]. This method describes the tip shape with a hyperbolic geometry, like in Figure 2.5 and allows calculation of induced charge density at the interfaces. Thus, the more descriptive shape of the tip, the better information about the tunneling junction can be obtained. In general terms, the shape of the emission spectrum is governed by the aperture of the tip. Furthermore, the curvature of the apex influences the intensity. Simulations of electromagnetic coupling inside the junction are done for different tip and sample materials. They are in agreement with experiments [34, 81]. Also multiple tip effects have been investigated [82, 83]. Furthermore, the emission behaviour is also determined by the local electronic structure, which is related to the sample topography and the chemical composition of the sample surface. This effect has been already observed in atomically resolved photon emission measurements [34, 58, 59].

2.2 Aspects of Photon-STM and SNOM

With the introduction of scanning probe microscopy (SPM) in the early 80's, tip-sample distances of a few angstroms (Å) could have been achieved as a consequence of tunneling currents. The control of such small distances allowed the introduction of near optical field techniques, which make use of optical excitation as well as light collection in a full way. A schematic picture of Photon-STM and Scanning Near Field Optical Microscopy (SNOM) is depicted in Figure 2.11.

The STM techniques described in this thesis perform electron excitation and probe the far optical field. On the other hand, SNOM techniques work with both photon detection and excitation, so that they can probe both far and near optical field. The optical near field provides a complete new perspective, which brings new information as well as new physics. Here, we will explain some of the concepts in which the near field physics is based.

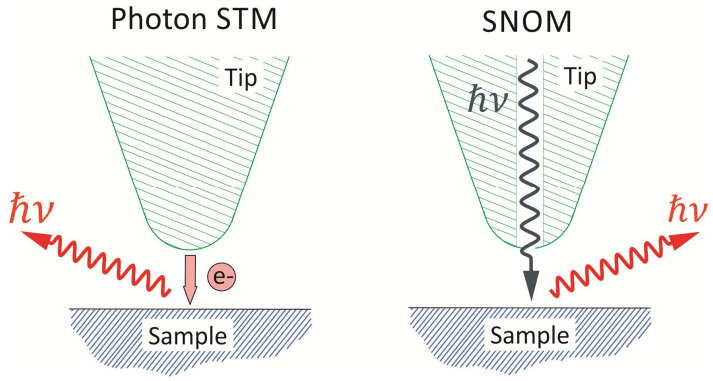

Figure 2.11. Photon-STM configuration in comparison with SNOM. Whereas the sample is excited with electrons in the first one, fully optical excitation is achieved in the latter.

2.2.1 Introduction to Evanescent Optics

The aim of this part of the thesis is to introduce the fundamental basis of the near field optics. The diffraction limit is associated with the optical far-field, which is formed by propagating waves. On the other hand, the evanescent counterpart is what dominates the near-field of radiation and is therefore important for the near field optics.

The first attempts at using evanescent waves in optics were introduced by Newton's experiments on light. The peculiar behaviour of total reflection has been studied both theoretically and experimentally by well-known scientists such as A. Fresnel. Evanescent waves, which are generated by total reflection, are often called *Fresnel evanescent waves*. E. Hall presented the first experimental results dealing with the behaviour of the evanescent wave versus incident angle, polarization, wavelength and denser medium characteristics [84]. In terms of theory, several studies have been done to study the energy flow with the notion of exponential decay [85, 86].

Evanescent waves never occur in a homogeneous medium but are inevitably connected to the interaction of light with in homogeneities. The simplest case of an inhomogeneity is a plane interface and will be described in the next paragraphs.

Theory of Fresnel 's evanescent waves. Reflection and refraction laws

The following situation considers a plane wave impinging on a flat interface between two media of different indices. It is widely known that the light beam is split into two: a transmitted beam propagating into the second medium and a reflected beam propagating back in the first medium. The boundary between the two media is perfectly flat and infinite. Thus, it can be assumed that the two waves generated by interaction of the incident beam on the sample are also perfectly plane, see [87]. According to the work of Born and Wolf [88] the following set of parameters can be defined:

v_1 is the velocity of light in medium 1,

v_2 is the velocity of light in medium 2,

ε_1 is the dielectric constant of medium 1,

ε_2 is the dielectric constant of medium 2,

n_1 is the index in medium 1,

n_2 is the index in medium 2,

θ_i is the incident beam angle,

θ_t is the transmitted beam angle,

θ_r is the reflected beam angle,

$A_{\parallel}$ is the complex amplitude of the incident field parallel to the incident plane, often referred to as *p* or *TM* mode,

$A_{\perp}$ is the complex amplitude of the incident field perpendicular to the incident plane, often referred to as *s* or *TE* mode,

$R_{\parallel}$, $R_{\perp}$, $T_{\parallel}$ and $T_{\perp}$ are the complex amplitudes of the reflected and transmitted fields, respectively.

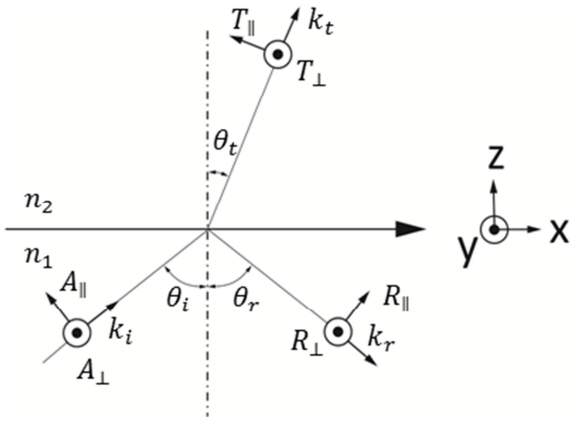

Figure 2.12. Interaction between a plane wave and a plane surface interface between two different media

From Maxwell's equations, the value of the reflection and transmission coefficients can be easily determined and deduced from the above-mentioned parameters. They take the well-known expressions:

$$\left.\begin{aligned} T_\parallel &= \frac{2\, n_1\, \cos\theta_i}{n_2\, \cos\theta_i + n_1\, \cos\theta_t}\, A_\parallel \\ T_\perp &= \frac{2\, n_1\, \cos\theta_i}{n_1\, \cos\theta_i + n_2\, \cos\theta_t}\, A_\perp \\ R_\parallel &= \frac{n_2\, \cos\theta_i - n_1 \cos\theta_t}{n_2 \cos\theta_i + n_1 \cos\theta_t}\, A_\parallel \\ R_\perp &= \frac{n_1 \cos\theta_i - n_2 \cos\theta_t}{n_1 \cos\theta_i + n_2 \cos\theta_t}\, A_\perp . \end{aligned}\right\} \quad (2.17)$$

These equations are called *Fresnel's formulae*, as they were established by A. Fresnel in 1823. From this set of formulae it is possible to describe any optical situation and more particularly the case of *total internal reflection*. The complex amplitude of the transmitted field can also be deduced for both the electric and the magnetic fields:

$$\vec{\boldsymbol{E}}(x,y,z,t) = \left(-T_\parallel\, \cos\theta_t\, \check{\boldsymbol{\imath}} + T_\perp \check{\boldsymbol{\jmath}} + T_\parallel \sin\theta_t\, \check{\boldsymbol{k}}\right) e^{-i\tau_t} \quad (2.18)$$

and

$$\vec{\boldsymbol{H}}(x,y,z,t) = \left(-T_\perp\, \cos\theta_t\, \check{\boldsymbol{\imath}} - T_\parallel \check{\boldsymbol{\jmath}} + T_\perp\, \sin\theta_t\, \check{\boldsymbol{k}}\right) \sqrt{\varepsilon_2}\, e^{-i\tau_t} \quad (2.19)$$

where

$$\tau_t = \omega \left(t - \frac{x\, \sin\theta_t + z\, \cos\theta_t}{v_2}\right) \quad (2.20)$$

and $\check{\boldsymbol{\imath}}, \check{\boldsymbol{\jmath}}, \check{\boldsymbol{k}}$ indicate the x, y, z directions, respectively.

Total internal reflexion

Assuming $n_1 > n_2$, the Snell-Descartes relation leads to

$$n_1 \sin\theta_i = n_2 \sin\theta_t \,. \tag{2.21}$$

This condition can be fulfilled when medium (1) is denser than medium (2) provided that the incident angle θ_i exceeds the value of the critical angle θ_{ic} defined as

$$\sin\theta_{ic} = \frac{n_2}{n_1} = n_{21}. \tag{2.22}$$

In the case that θ_i reaches the critical angle value θ_{ic}, the transmitted angle θ_t tends towards 90° and the light beam propagates along the boundary surface. In order to explain this behavior, one condition should be assumed: the light beam enters the second medium and *then* goes back into the denser medium. This phenomenological description seems to prove that light propagates in the second medium *before* getting back into the denser medium. This is known as *Goos-Hänchen shift*.

From the previous equation (2.21) and (2.22) it can be deduced that:

$$\cos\theta_t = \pm i\sqrt{\frac{sin^2\theta_i}{n_{21}^2} - 1} \tag{2.23}$$

leading to the term containing the phase factor of the transmitted wave:

$$e^{-i\tau_t} = e^{-i\omega\left(t - \frac{x\sin\theta_i}{v_1}\right)} e^{\mp\frac{\omega z}{v_2}\sqrt{\frac{\sin^2\theta_i}{n_{21}^2}-1}}. \tag{2.24}$$

The last equation (2.24) can be interpreted as an inhomogeneous wave that propagates along the *x*-direction and varies exponentially in the *z*-direction. Assuming that the rarer medium is infinite, only the negative sign in the argument of the exponential term must be kept. If this is not the case, the amplitude would increase exponentially tending towards to infinity with *z*. However, if the rarer medium is limited by another medium of denser index, the two terms should be taken into account.

According to equations (2.18) and (2.20), the TE and TM transmitted electric fields can be rewritten as

$$\vec{\boldsymbol{E}}(x,y,z,t)_\perp = T_\perp e^{-i\omega\left(t - \frac{x\sin\theta_i}{v_1}\right)} e^{-\frac{\omega z}{v_2}\sqrt{\frac{\sin^2\theta_i}{n_{21}^2}-1}}\,\check{\boldsymbol{j}}, \tag{2.25}$$

and

$$\vec{\boldsymbol{E}}(x,y,z,t)_\parallel = \left\{-T_\parallel\cos\theta_t\check{\boldsymbol{\imath}} + T_\parallel\sin\theta_t\,\check{\boldsymbol{k}}\right\} e^{-i\omega\left(t - \frac{x\sin\theta_i}{v_1}\right)} e^{-\frac{\omega z}{v_2}\sqrt{\frac{\sin^2\theta_i}{n_{21}^2}-1}}. \tag{2.26}$$

Whatever the polarization, from equations (2.25) and (2.26), the field $\vec{\boldsymbol{E}}(\boldsymbol{x},\boldsymbol{y},\boldsymbol{z},\boldsymbol{t})$ can be rewritten in the following compact form:

$$\vec{\boldsymbol{E}}(x,y,z,t) = \vec{\boldsymbol{E}}(x,y,t)e^{-d_p z} \tag{2.27}$$

with

$$d_p = \frac{\omega}{v_2}\sqrt{\frac{\sin^2\theta_i}{n_{21}^2} - 1}. \tag{2.28}$$

From Fresnel's formulae (2.17) applied to the particular case of evanescent fields, it can be easily deduced that

$$|R_{\parallel}| = |A_{\parallel}| \ , \ |R_{\perp}| = |A_{\perp}| \ , \tag{2.29}$$

which means that the totally reflected components are equal to the respective incident components.

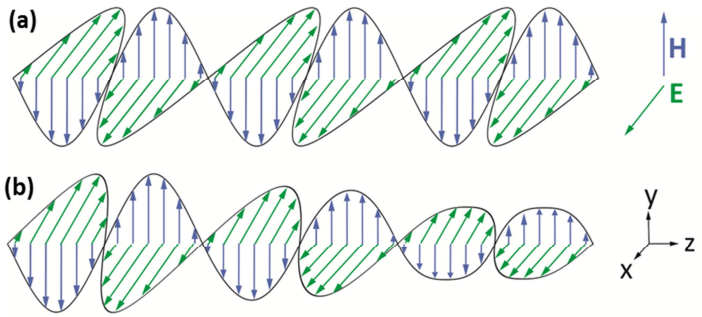

Figure 2.13. (a) propagating wave and (b) evanescent wave

The complete wave in equation (2.27) provides a term with exponential decay, which means that the amplitude of the wave decreases as long as the wave propagates, as it can be appreciated in Figure 2.13. These waves are the so called evanescent waves and represent the fundamentals of near-field optics, which will be described in detail in the following part of this thesis.

2.2.2 Angular Spectrum Representation

From a mathematical point of view, a powerful tool to describe wave propagation is the angular momentum representation. In this model, the electric field $\vec{E}$ in the detector plane at *z* can be considered as a superposition of harmonic waves of the form $e^{\vec{k}\vec{r}-\omega t}$. They have amplitudes $\vec{E}(k_x, k_y, z=0)$ that come from the source place at $z = 0$ [21, 89].

$$\vec{E}(x,y,z) = \iint_{-\infty}^{\infty} \vec{E}(k_x, k_y, z=0)\, e^{i(k_x x + k_y y)}\, e^{\pm i k_z z}\, dk_x\, dk_y \tag{2.30}$$

In this expression $\vec{k}$ represents the wave vector and describes the propagation direction of the wave. Its components are $\vec{k} = (k_x, k_y, k_z)$ and its length is defined by the wavelength of the light λ and the refractive index of the medium n through the following expression:

$$|\vec{k}| = \sqrt{k_x + k_y + k_z} = \frac{2\pi n}{\lambda} \tag{2.31}$$

If $n = 1$ and the wave is limited to the *x*-*z* plane, which means no dependence of *y*, the following relation applies:

$$|k_z| = \sqrt{\left(\frac{2\pi}{\lambda}\right)^2 - (k_x)^2} \tag{2.32}$$

In equation (2.30) the term $e^{\pm ik_z z}$ dominates the propagation of the corresponding wave. Two cases can be distinguished:

(i) if $k_x \leq 2\pi/\lambda$, the component k_z is real and the associated wave propagates in *z* direction with an oscillation of $e^{-ik_z z}$, and

(ii) for $k_x > 2\pi/\lambda$, the component k_z turns complex and the expression $e^{-|k_z|z}$ describes an exponential decay. Thus, this last case is related to an evanescent wave. As a consequence, only waves with $k_x \leq 2\pi/\lambda$ can propagate and contribute to the field far from the source.

In general, the wave amplitudes of the electric field come from a two dimensional Fourier-transformation of $\vec{E}$. This mathematical transformation represents a correlation between time and frequency domain. In this correlation, a short optical pulse requires a broad frequency spectrum. In the same way, a sharp field distribution requires a broad spectrum of spatial frequencies k_x. Due to the fact that only waves with spatial frequencies limited to $k_x \leq 2\pi/\lambda$ can propagate, the spectral width decreases quickly as long as the distance from the source *z* increases. That leads to a fast broadening of the electric field distribution in real space, as depicted in Figure 2.14 [21]. Propagation is seen as a low pass filter with cut-frequency $k_{x,max} = 2\pi/\lambda$. The far-field contains limited spatial frequencies and therefore equivalent limited spatial information. There are two ways to overcome this limitation: *(i)* new approaches should be considered in the far-field optics, or *(ii)* information should be obtained from the near-field. Section 3.1 of this thesis is dedicated to a development related to the second case.

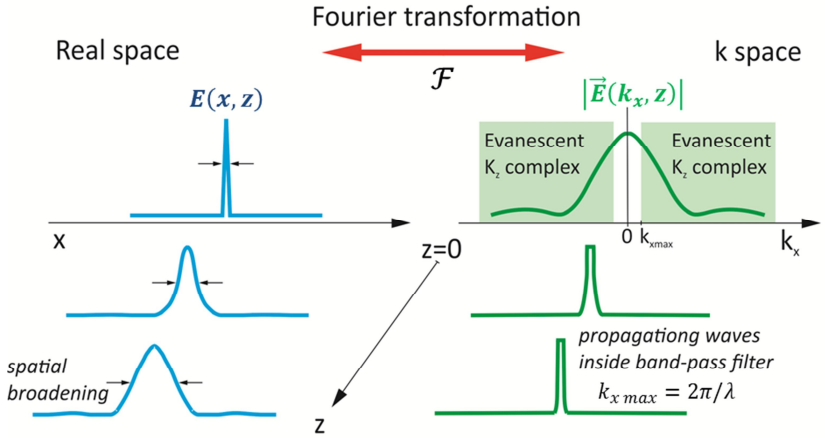

Figure 2.14. Propagation of waves and loss of spatial information. On the top: initial field distribution and its angular spectrum. Both evanescent and propagation waves are contained in the spectrum. Middle and bottom: development of the field when the distance in *z* increases. The decay of high spatial frequencies leads to spatial broadening and threfore loss of spatial information.

Since fast exponential decay is related to higher spatial frequencies, high resolution images in the near-field require probe-sample distances of a few nanometers, which is in turn achievable with scanning tunneling techniques. Therefore, near-field microscopy is limited to surface or subsurface studies.

To sum up, the concept of evanescent field was introduced and related to the basis for the understanding and necessity of the near field optics. A further description of the construction of the SNOM microscope is the focus of the next chapter of this thesis.

Chapter 3

Experimental Methods

This chater aims to describe the experimental techniques used for the experiments in this thesis. The first section of the chapter deals with the new microscope and explains the construction steps as well as the first measurements. The second section is related to the already well known Photon-STM and some of the secondary tools [16].

3.1 Scanning Near-Field Optical Microscopy (SNOM)

The aim of this section is to give a general introduction of Scanning Near-Field Optical Microscopy and to describe the system developed in our group. In the future, we plan to use this microscope to do optical measurements on dielectric films with a resolution lower than 5nm. The measurements will imply luminescence of doped oxides, scattering of particles, molecular luminescence as well as reflection and absorption of base oxides, as depicted in Figure 3.1.

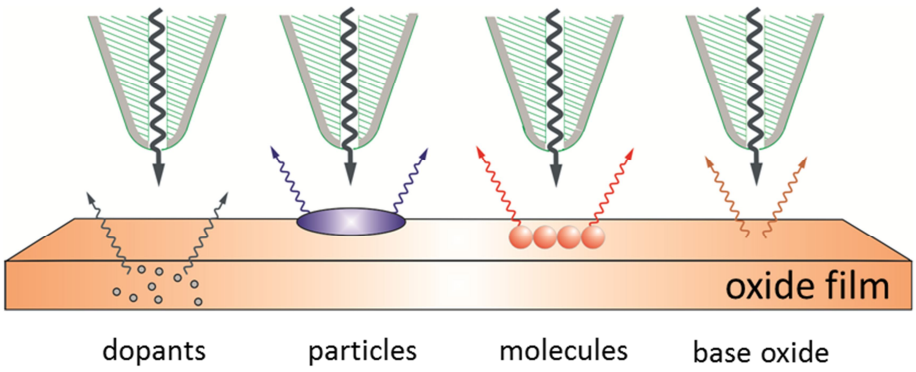

Figure 3.1. Schematic of the luminescence obtained from different effects of oxides films for what the microscope is being constructed

The optical system has never been invented: it is one of the five senses of most living beings and for a very long time man has tried to improve his ability to see [87]. Along the history of science, the concept of *image* has always been present. Starting from a physical entity called *object*, the definition of its image results from a given transformation of itself. The similarity between object and image is not mandatory. For instance, what we consider an image of a star is barely related to the star itself. From a mathematical point of view, the Fourier spectrum of a certain field distribution is also an image. However, we are much more familiar with the normal concept of an image. This concept tends to relate the object and the image through a simple transform or similarity.

$$Object \xrightarrow{T} Image$$

As the object itself is normally a three-dimensional piece of matter (a star, a bacteria, an atom…), the relation between an object and an image is never simple. In contrast to the object, its image typically consists of a two-dimensional distribution of light intensity.

To describe an imaging system as simple as possible, the light beam is considered as a bundle of elementary light rays. These rays respond to the classical conservation laws (Maupertius's principle, Fermat's principle, Clausius statement, etc.). Such an interpretation is accurate enough for usual applications and the physical reality is rather correctly reflected. This interpretation takes into account that each light ray is infinitely thin and can be considered independent from the others. The possibility of light diffraction is indirectly discarded, as light behaviour is completely characterized by only energy conservation laws. In this way, if the system is free of aberration, the image can be a quasi-perfect copy of the object.

In order to understand microscopic effects, such a rough model is not enough and the wave theory is necessary. E. Abbe was one of the first scientists who applied wave theory to image systems [90]. He demonstrated that every object acts as a grating, diffracting in part of the light going through it. For small grating periods, the diffraction angle is large and the image lens only collects a small amount of light. On the other hand, when the period is large, the light beam is slightly diffracted and the lens catches the maximum of light. It is now easy to understand that high frequencies will be less easily transmitted than low frequencies. In addition, any detector system shows a cutoff frequency due to its geometry.

According to Abbe´s theory, a light beam impacting on a flat object (in this case a 2D entity) is diffracted by the object features. Due to the diffraction properties, the smaller the details, the higher the diffraction orders. Typical optical microscopes always start from simple single-lens based designs and evolve towards more complicated advanced microscopic configurations. These advanced configurations can improve the amplification capability and decrease the effect of chromatic aberrations. Along the past years, the resolution issue has always been the key topic of optical microscopy. The final resolution is strongly dependent on imperfections and misalignments in the lenses. From a physical point of view, one of the fundamental limiting factors lies in the light diffraction. The ideally focused light spot (Airy disc) that a perfect lens with a circular aperture can produce is defined by light diffraction. The Abbe's diffraction limit $d = \frac{\lambda}{2\,n\,\sin\theta}$ is the crucial parameter which describes the fundamental resolution limit of any optical system [90]. This limit is related to the smallest distance that is distinguishable between two objects. Nowadays, the numerical aperture $n\sin\theta$ can reach values of about 1.4. This indicates that the resolution is limited to about half of the excitation wavelength due to diffraction effects. As the minimal wavelength normally corresponds to ultraviolet-visible zone, the resolution of optical microscopy lies at the scale of a few hundreds of nanometers.

In the early 1980s, scanning probe microscopy (SPM) methods were introduced to obtain information from surfaces, as described in section 2.1. They consisted of a fundamentally different approach with even better lateral resolution [32]. An alternative approach is the scanning near-field microscope (SNOM or NSOM). It combines scanning probe concepts and optical microscopy. A SNOM probe is scanned

very close to the sample surface in the region called the optical near field, as mentioned before. The use of a small aperture to image a surface with the resolution smaller than the wavelength of light is the fundamental concept of the optical near-field. This idea was first proposed in 1928 by E. Synge, an Irish scientist [91]. In his proposal he introduced the use of a strong light source behind a thin, opaque metal film with a 100 nm diameter opening. A very thin biological sample should be locally illuminated by the tiny spot of light. To assure local illumination, he proposed the condition that the aperture in the metal film should be less than 100 nm away from the object, being the similar order of magnitude as the aperture diameter. Using a sensitive photo detector, the images were to be recorded point by point by detecting the transmitted light from the sample. Even though Synge was well ahead of his time with his proposal, he never tried to realize his idea. In 1932, he discarded his original scheme due to the difficulties of the approach and he proposed an alternative [92]. In his new proposal, he replaced the aperture with the image of a point light source as the optical probe. The image was to be generated by an ellipsoidal mirror which would provide, in modern terms, the largest possible numerical aperture. However, also his second idea was never realized.

In 1984, nanometer-scale positioning technology was available thanks to the invention of the scanning tunneling microscope [93] and an optical microscope similar to Synge's idea could be addressed again. Pohl and coworkers together with Denk and Duering at the IBM Rüschlikon Research Laboratory re-invented the forgotten scheme [94-96]. Independently, Lewis and his group at Cornell University proposed a similar scheme [97-99]. They produced a subwavelength optical aperture at the apex of a sharply pointed transparent probe tip that was coated with a metal. Similar to the STM configuration, they implemented a feedback loop to maintain a constant gapwidth of only a few nanometers. In such configuration the sample was raster scanned in close proximity to the fixed probe.

In order to extend the power of optical microscopy beyond the diffraction limit, several configurations were proposed and further developed along the time. Such configurations are capable of getting optical images with 10-50 nanometer resolution. These configurations differ in the way how the light excitation is done, as depicted in Figure 3.2. Classical aperture SNOM, in which an aperture probe illuminates a small area of a sample surface, is shown in Figure 3.2b. In this work, the light reflected by the sample is collected by means of a parabolic mirror, which converts the light in parallel rays and delivers them to a detector. This way of collecting light is similar to the one used in our Photon-STM equipment that has been developed before by *Nilius et al* and is described in [16]. In other cases, light is collected by a hemispherical medium, which allows capturing all the radiation from the probe-sample interaction zone into the far field [100, 101].

The principle of apertureless near-field optics methods is shown in Figure 3.2c [102]. This configuration implies a strongly confined optical field situated at the apex of a tapered or a solid probe tip. This tip is iluminated by an external far-field. Using different channels, the relevant near field optical (NFO) signal should be extracted from a huge background of far-field scattered radiation. Resolutions ranging from 1-20 nm have been reported [103-105]. Nowadays, this configuration is typically combined with

atomic force microscopy (AFM) techniques to obtain topographic as well as optical sample information at the same time.

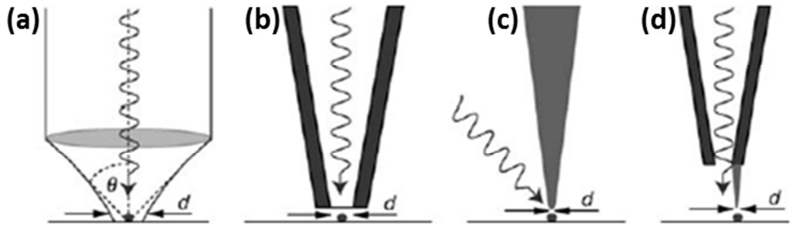

Figure 3.2. (a) Far-field focusing using a lens, as used in confocal microscopy. (b) Aperture-SNOM, (c) tip-enhanced SNOM and (d) tip-on-aperure (TOA) approach [21]

Based on localized light excitation, our microscope brings many advantages for surface science experiments. As an example, it would be very convinient to study dopant properties in oxides films using the full optical methodology. Cathodoluminiscence techniques, as used in other chapters of this work, often imply high energy excitations with a 50 eV threshold in some cases. For excitations energies below this value, no luminescence is seen. Futhermore, other undesirable effects do normally take place, like electron-hole pair or Auger excitations in the oxide host, impact ionization and electron cascades or field emission resonances (FER). On the other hand, exciting with light brings many advantages like the possibility of local and resonant excitation, the control of polarization as aditional parameter and the feasibility of time-dependent measurements. The following list aims to make a comparison of both experimental techiques treated in this thesis:

Properties	**STM**	**SNOM**
excitation	electrons	light
detection	electrons	light
distance control	tunneling current	tunneling current
resolution	1-5 Å	1-5 nm
observable information	topographic, electronic structure, optical properties	optical properties, luminescence, non-elastic processes

3.1.1 The aperture SNOM

An aperture is a very confined light source without any background. In contrast, in the apertureless techniques, a rather large intensive laser spot is focused onto a tiny tip apex. In the aperture case, which is developed in this work, a laser light of suitable wavelength is coupled into an optical fiber. This optical fiber has an aperture probe at its far end, which acts as an ilumination spot. In most developed aperture microscopes, the control of the polarization and spectral filtering of the light should be done before coupling the light into the fiber. However, this point was not reached in our microscope and should be further developed. A schematic picture of the idea is depicted in Fig. 3.3. The tip is mounted onto a thin stainless steel tube, which acts as a holder and provides

electrical conductivity at the same time. This thin tube is wire connected to the electronic controller in order to detect the tunneling current for the feedback purposes. The feedback in our setup is based on constant tunneling current, which in turn mantains the gapwidth between tip and sample.

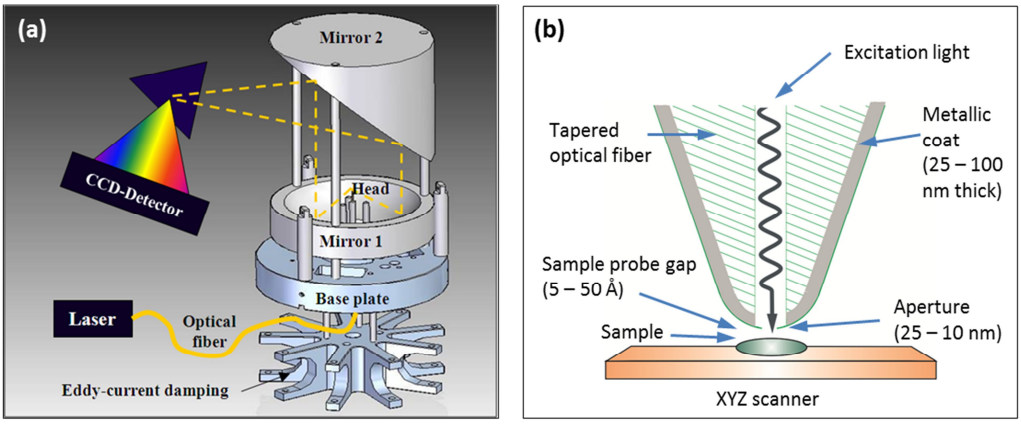

Figure 3.3. Schematic drawing of (a) head system design and (b) SNOM aperture tip

Light that is emitted by the aperture locally interacts with the sample. On well prepared sample systems, light can be absorbed, phase shifted or produce local fluorescence. In any case, light coming from the interaction zone has to be collected with the highest possible efficiency. For this purpose, two parabolic mirrors were mounted. The first one sorrounds the sample and has its focus point situated at the tip apex. The configuration is similar to the Photon-STM system described in section 3.2 and in the literature [16]. This first parabolic mirror (Mirror 1 in Fig. 3.3a) collects the light released from the sample and delivers it to another parabolic mirror situated on the top (Mirror 2). This second mirror takes the parallel rays and focusses them to a photodiode or a CCD detector coupled to a grating spectrograph. Figure 3.3 depicts the configuration with the two mirrors, the optical fiber, the laser for the excitation, the base plate to support the SNOM setup, the Eddy-currend damping system for vibrational isolation and the detector.

3.1.2 Fabrication of Near-Field Optical Probes

The fabrication of the fiber-based optical probes used for experiments implies two main steps: *(a)* creation of transparent taper tips with a sharp apex, and *(b)* subsequent metallic coating to obtain an enterely opaque film on the cone walls and to create a transmittive aperture at the apex. Regarding the first step, two methods are already well known to obtain tapered optical fibers. These methods provide sharp tips with reasonable cone angles: *(i)* the “heating and pulling” method, and *(ii)* chemical etching.

The heating and pulling method is based on local heating of the fiber with a laser or a filament, which is subsequently pulled apart by mechanical forces. The advantage of this method is that the glass surface on the taper is very smooth, which provides a higher quality of the evaporated metal layer. However, this technique was not used in this work due to the absence of a suitable fiber puller.

The second method employs chemical etching of the optical fibers in acid solutions. This method is well known as the Turner's etching technique [106, 107]. It involves dipping the fiber into an acid solution covered with an overlayer of an organic solvent. In our case, the solution was made of 2ml of HF at 40% conentration and 0.6 ml of Brome Decane. Tips were dipped 1mm deep into this solution for 2 hours. Tip formation takes place at the meniscus that forms at the interface between HF and solvent across the fiber, as shown in Figure 3.4. The principle of this etching mechanism lays on the fact that the meniscus height is a function of the remaining fiber diameter. This method allows more reproducible production of larger quantities of probe tips in a single step. Our configuration allowed to etch up to three tips at the same time. One of the advantages was that the taper angle could be tuned by varying the organic solvent of the overlayer. The solution and quantities mentioned above turned out to be the optimum parameters for etching tips at 90° with respect to the liquid solution, as seen in Figure 3.4.

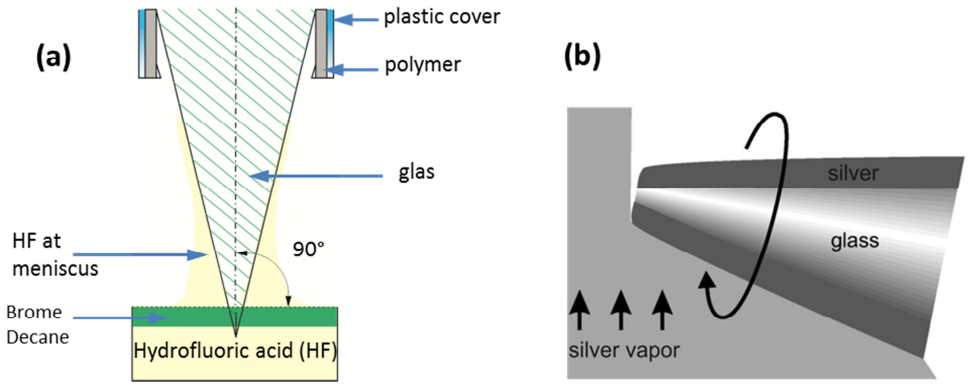

Figure 3.4. (a) Representation of etching procedure. (b) Geometry of the evaporation procedure. The deposition rate is definitely smaller at the apex than on the side walls due to the slighty angle and the rotation movement (adapted from [20]).

A major disadvantage of our approach is the microscopic roughness of the glass surface on the taper walls. However, this problem was solved by introducing the so called tube etching method [108, 109]. The improvement of this procedure is that the fiber was not completely stripped before dipping it into the acid. The thin polymer layer between glass and outer layer was not removed. Now, tip formation took place insde a small volume defined by the polymer coating due to convective flow of the HF. This method turned out to be less prone to produce roughness on the taper and, however, provided relatively small cone angles. Nevertheless, for the same amount and depth of the fibers in solution, different angles were obtained (see Figure 3.5). In general, optical tapers produced by HF etching were relatively sharp. While this is good for the achievable spatial resolution, it made the tip unstable against mechanical load forces. In particular, the tips had a high tendency to break during further handling. A larger opening angle was thus desirable for the tapered fiber. So far, the issue of optimal angle that provides both mechanical stability as well as reasonable spatial resolution could not be solved in this PhD work and further research is required in this aspect.

In both cases, the aperture is intended to be covered with a highly reflecting metal coat via evaporation in the next step. For this porpouse, we tried with gold, silver and

aluminium. Silver turned out to be the most efficient with respect to the evaporation parameters, as aluminium melted easily in our evaporation setup. The parameters for the e-beam evaporation were the following: 800V for the acceleration voltage, ~2.0 A for filament current, 20mA for emission current. Using this configuration, a flux of 10 µA was measured at the top of the evaporator. Evaporation was done in two periods of 24 minutes. With these parameters, a covering layer of approximately 100 nm was achieved. In principle, the formation of the aperture was caused due to the difference in metal depostion rate at the apex and on the sides of the tip. As there is a certain angle from behind, the deposition rate at the apex was much smaller than at the sides. This geometrical shadowing effect leads to the self forming of an aperture at the tip apex [20], as depicted in Figure 3.4b.

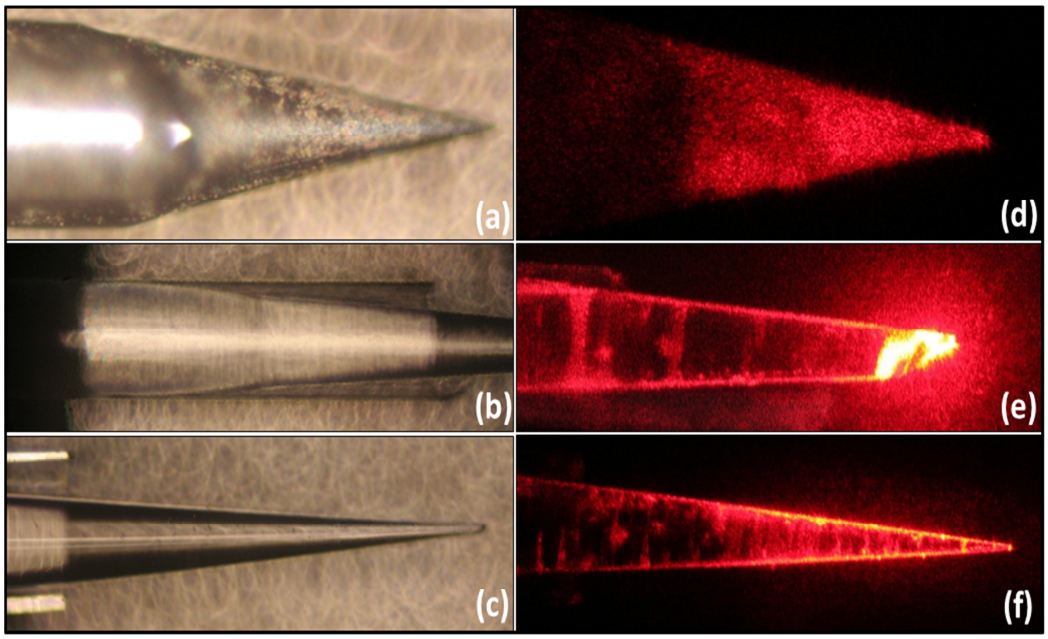

Figure 3.5. Glas fiber tip etched 2mm deep in 2ml HF and 0.6 ml Brome Decane: (a) without and (b,c) with polymer layer. Note the different cone angles obtained and the volume for the HF between glas and polymer in (b). (d-f) Light emitted by different coated tips

Light was coupled into the fiber by using a small stainless steel wire-coupler. It conected light coming from the He-Ne laser to the fiber. The corresponding wavelength was 632nm. The light coupling into the apex has been tested for tips with different cone angles and also for arbitrary shaped tip apexes. In Figure 3.5(d) and (f), it is seen how light is homogenously emitted along the entire cone. In case (e), it is revealed however, how the light gets concentrated on the apex, in spite of its irregular termination. In the case of Figure 3.5d, the cone angle is suitable but the metallic coating is too thick, while in Figure 3.5e, the opening in the coating is fine but not symmetric. On the other hand, the coating of the tip in Figure 3.5f might be too thin. We were not able to achieve reproducible light emitting tips. The difficulties were mainly to obtain the opening in the coating of the fiber, which turned to be the main problem of the experiment. New approaches are needed in this field, probably by means of wet chemical precipitation.

3.1.3 Microscope Head and First Experiments

The microscope architecture consists of a Beetle-STM, which is based on the Besocke design. The system with its four piezoelectric tubes, the sample plate and the ramps is described in section 3.2 of this work and in the literature [16]. The design combines large piezoelectric scan ranges of up to 10x10x1 μm^3, the implementation of hardware-linearized piezoelectric scan stages and flexible coarse positioning.

The new setup was first tested and used as normal STM. Here, it proved to be capable of doing tip approach and retract as well as scanning processes. The results of the first test are found later in this chapter. As a first step, bare gold wires were used as a tip. This ensured reliable and stable tunneling conditions as well as approach and retract of the sample. A bare gold (111) sample was used for the first imaging tests, showing step edges and large terraces. The system was operated in air conditions and it has been mounted to a spring isolation damping system. This damping system consists of three springs. The spring constant *k* was chosen such, that the setup elongated by roughly three times its initial length, after adding the base plate. The microscope head was hanging from a support on an optic table to improve the stability conditions. Figure 3.6 shows the system with the mounted mirrors and the tip, from which light is being emitted.

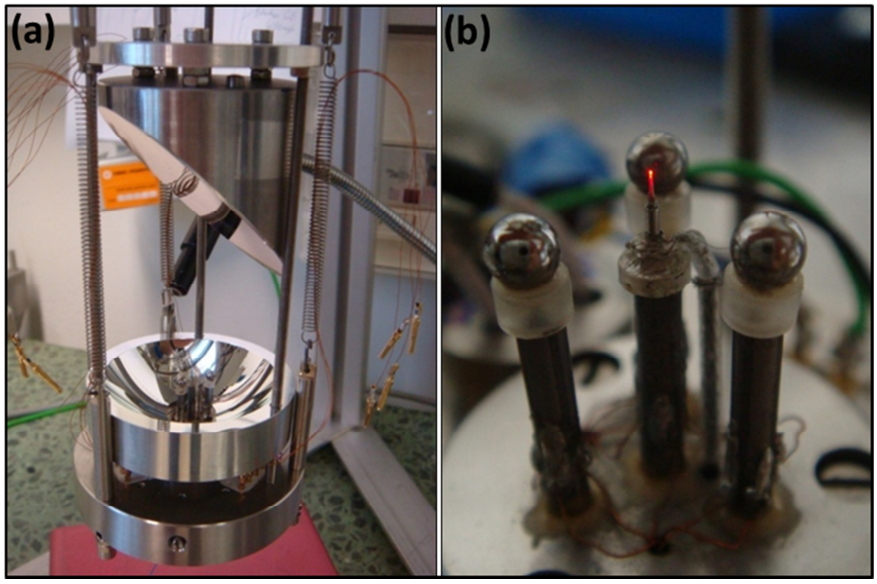

Figure 3.6. (a) Microscope head with damping system and (b) optical fiber tip with light at its apex

A commercial grating pattern was gold sputtered to achieve electrical conductivity. This pattern was used for calibration purposes. The sample consisted of a 3D-square pattern, which was sized in the scale of a few micrometers. The periodicity of the square grating was with 1,5 µm already large with respect to the scan range of the microscope. Therefore, only main steps of the pattern were observed in Figure 3.7, which shows a STM image obtained with a gold tip. The inset of Figure 3.7b illustrates the calibration pattern and gives an idea of its dimensions.

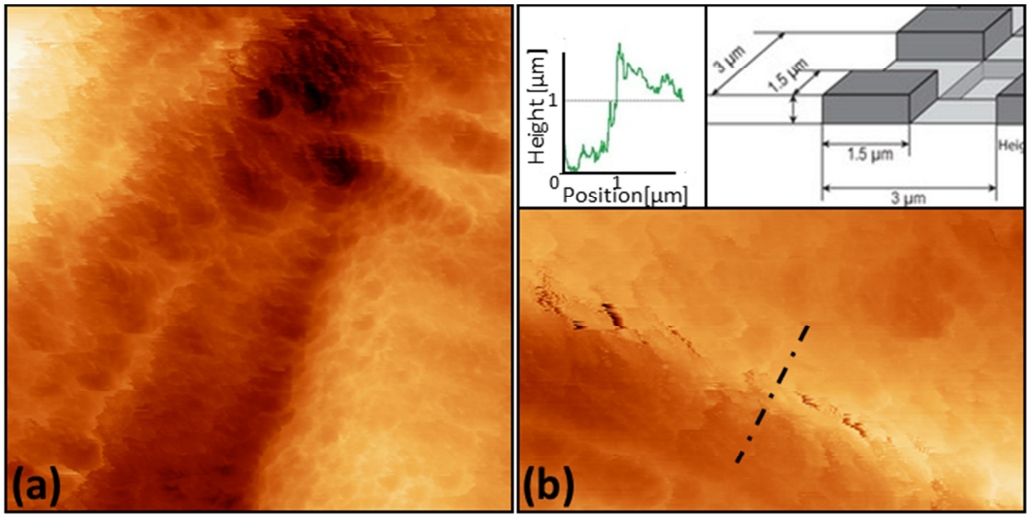

Figure 3.7. Topographic images of the square pattern obtained by a gold tip (5 nA, 5V, 1.5x1.5 μm^2). The dimensions of the calibration pattern can be seen in the inset of (b).

The system was able to provide the first measurements, showing simultaneously topographic as well as optical information of a surface. In this first approximation, it can be seen in Figure 3.8, how the light response corresponds the surface topography of a Au(111) crystal. Evidently, on the up-right corner the light is more intense than in other regions of the sample. The enhanced light may be coming from defect like steps or corners, which are likely to emit more light according to the literature [110]. Light was collected for 5 minutes in dark environment. As the measurements were performed in air conditions and the corrugation of the sputtered sample was rather high, it can be just considered as a proof of principle of the method. The approximate spatial resolution of the method amounts to 50 nm in this example. The measurement was performed using the feedback of the STM, light was coming from the tip and collected in the parabolic mirror from the far field, due to the big aperture on the fiber.

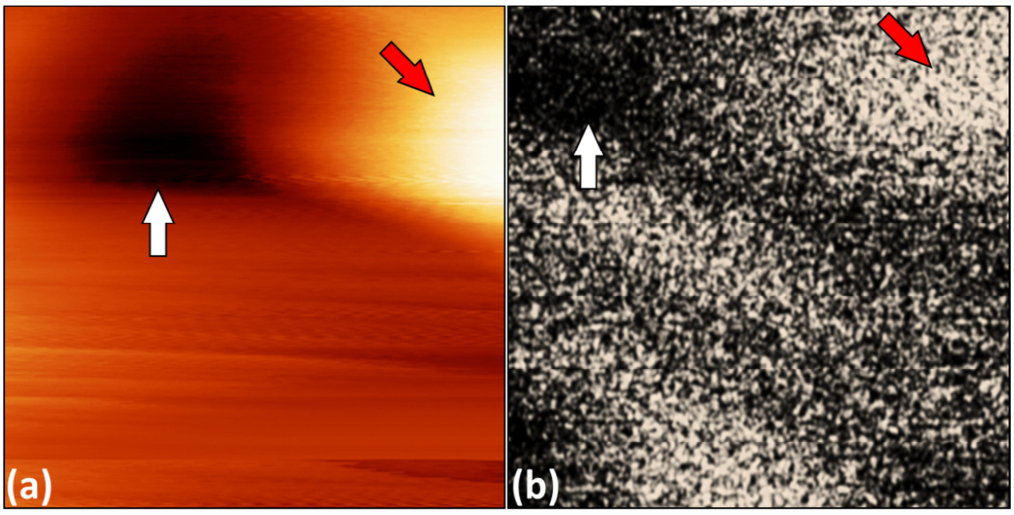

Figure 3.8. (a) Surface topography and (b) corresponding light emission map obtained at 5V and 10 nA (800x800 nm^2)

In addition, the photon intensity was recorded as a function of U_t between tip and sample. Two regimes could be distinguished. The first of them is the so called *proximity field emission*, which implies $|U_t| \leq 20\ V$. The second one is the *tunneling regime*, in which the wavelength of the visible light is much longer than the gap spacing. The set point was set to $|U_t| = 5\ V$ and $I_t = 15\ nA$. In addition, the light intensity was recorded during a stepwise approach and retract of the SNOM tip. The light trace is shown in Figure 3.9 and the effect is also found in the literature [61]. The photon intensity is observed to increase rapidly, exhibiting some small oscillations with the highest signal intensity in the tunneling regime. This tunneling regime is achieved for tip sample distances closed to zero. The red and green curves represent the approach and retract modes, respectively. Our interpretation consists in three regimes that are clearly distinguishable in Figure 3.9. In zone 1, tip is far away from the sample, so that there is no tip-sample coupling and therefore the intensity of the detected light is very low. In zone 2, however, the emerging tip-sample coupling enhances the light emission, increasing the detected intensity until it reaches the saturation area in zone 3. This saturation effect may come from either a shadowing effect or a change in the tip shape. The change of the tip can be seen in the different forward and backward traces, which is typical for experiments in air. To avoid tip changes, an ultra-high vacuum environment is needed. Figure 3.9a shows no tip change, as both approach and retract curves exhibit similar traces.

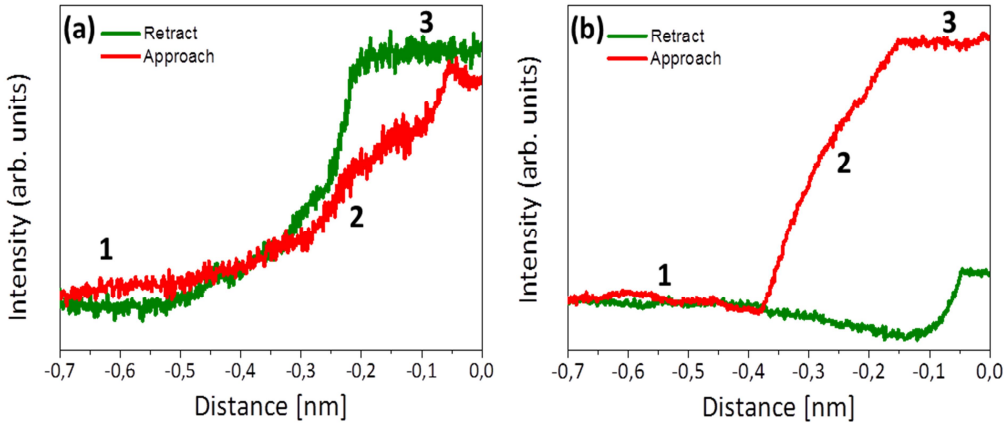

Figure 3.9. Photon intensity during approach and retract processes. Note the three zones: no coupling (1), coupling (2) and saturation (3).

Within this thesis, the primary steps in constructing an aperture SNOM with STM feedback-control were fulfilled. Regarding the technical problem of tip fabrication, there is also still plenty space for improvements, in particular in the fields of tip stability and damage threshold. Thermal assisted tip pulling might help to achieve less sharp tips with reproducible shape. A better coating of the tip is also desirable. The inset aperture should be obtained in a controlled and more reproducible way, as described in the literature [20]. The introduction of the system in an UHV environment might allow higher stability of the tips and stable conditions up to a bias of 10V. Operation at lower temperatures would also be desirable to improve stability. Regarding the improvement of samples, the knowledge from the Photon-STM can be transferred and applied for the investigation of optical effects on thin oxide films.

3.2 STM Experimental Setup

All experiments concerning the chapter 4 of this PhD work were carried out on a Beetle-design STM, which was operated at liquid-nitrogen (LN_2) temperature (100K) and Ultra-High Vacuum (UHV) conditions. A complete description of the microscope can be found in [16]. The system contains two chambers that are separated by a gate valve. One chamber is dedicated to the preparation of samples while the other one contains the microscope itself. The background pressure of $5x10^{-10}$ mbar is achieved with a turbo-molecular pump (pumping speed 150 l/s) in the preparation chamber. On the second chamber, an ion-getter-pump operates at 155 l/s, supported by a Titan-sublimation pump (TSP). A sputter gun (argon ion sputtering), two electron beam evaporators and a leak valve are mounted in the preparation chamber as well. The preparation chamber can be filled with reactive gases (O_2, H_2O) through this valve. The quality of the surface is checked by a two grid low energy electron diffraction (LEED) system in this chamber, which acts as a primary tool to clarify the structure of the different oxide films.

To heat the sample, a home-made filament of W/Th is placed at the back side of the sample, being held at high bias (from 100V to 2000V). To stimulate thermal electron emission, a current of approximately 3A flows through the filament resulting in an emission current of $\sim$5 mA. A pyrometer measures the temperature. We achieve atomically clean surfaces by cycles of sputtering and annealing.

At normal conditions, the sample is prepared and immediately transferred to the second chamber, which hosts the PSTM. The sample is normally ready for exploration after waiting for one hour to cool down. This is because heat flows from the sample to the LN_2 cooled plate only through small metallic spheres. The whole microscope is surrounded by a liquid-nitrogen flow-cryostat, which allows the STM head to be cooled down to temperatures of around 100K. A Pt100 sensor is charge of measuring the temperature. The working pressure of the Photon-STM chamber is of the order of $2x10^{-10}$ mbar. The STM head is suspended by four springs and also coupled to an eddy current damping system in order to isolate the structure to vibrational noise, giving rise to stable tunneling conditions.

The Beetle head consists of three outer piezos responsible for carrying the sample plate and therefore for *x*-*y* movement. Three ramps at the edges of the plate convert a tangential movement of the outer piezos into a movement in *z*-direction, see Figure 3.10 (upper inset). With this construction, approach and withdrawal are easily done without any tip movement and the outer piezos are furthermore capable of moving the sample on a micrometer range, which gives access to different areas. The metallic tip is carried by the central z-piezo, which approachs the sample surface through a hole in the central plate. The electric contact to the sample is made by stainless steel balls (radius=1mm) located on top of each piezo. To avoid electric contact between ball and piezos, a circular sapphire disk is situated between them. Only one metallic ball delivers the bias voltage to the sample.

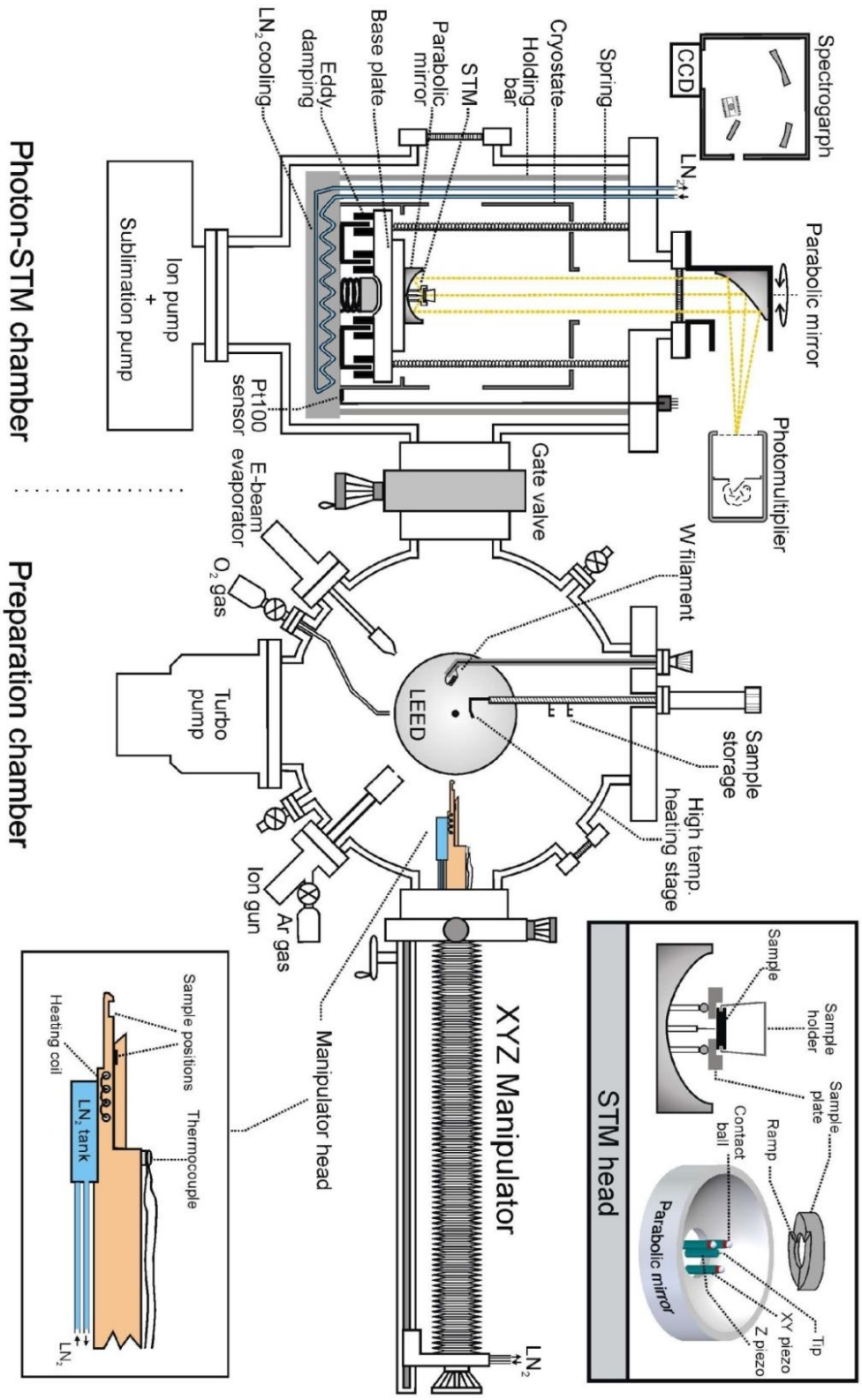

Figure 3.10. Schematic scheme of the Photon-STM and the preparation chamber used for the experiments in this thesis [51]

3.2.1 The Optical System

To measure light emission from the STM junction, the microscope head is surrounded by a parabolic mirror, whose focal point is located at the tip apex. This mirror is made of $AlMg_3$ compound and coated with a thin aluminum film, delivering a very low thermal expansion coefficient. With this configuration, most of the light emitted by the tip-sample junction is collected by the mirror and translated into parallel optical paths. Shadows of the outer piezos and the volume of the microscope itself reduce the collection angle; however, with no significant losses. A second parabolic mirror situated outside the UHV chamber collects the parallel beam delivered by the first one and directs it to a liquid-nitrogen-cooled PI/Acton SP-2156 spectrograph with a 1340x100 pixel CCD camera attached. In order to get enough intensity over a large spectral range, ~200nm (6.2eV) to 1000nm (1.2eV), the spectrograph is equipped with two gratings (150 grooves/mm) with different blazes at λ_{blaze}= 300 and 500nm. With this method, the emitted photons from the sample in a solid angle of ~3sr are concentrated on a point directly at the camera. Using acquisition times of 1 to 10 minutes, sensitivity curves for the whole optical path and the detector functions are obtained and shown in Figure 3.11a.

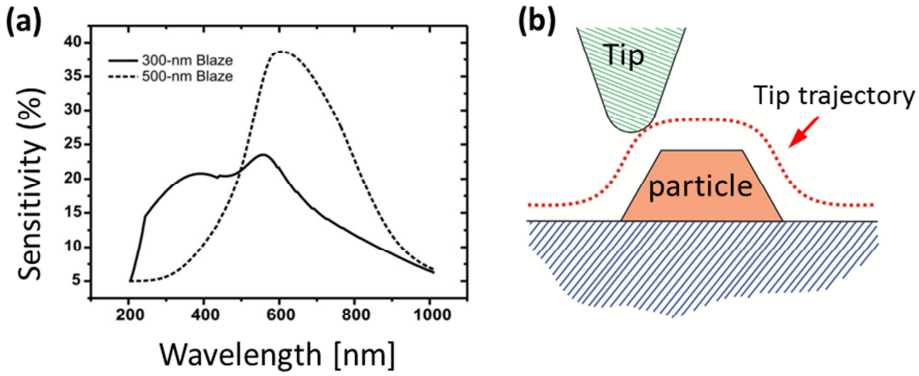

Figure 3.11. (a) Sensitivity curve of the CCD camera for the two blazes available. Adapted from [51]. (b) Representation of the tip convolution effect

Two modes for light excitation on the sample are supported by the system. The *tunneling mode*, which corresponds to voltages and currents in the range of tunneling conditions (voltages up to 10V and currents below 5nA). This mode allows for photon emission induced in local areas (1x1 nm^2). On the other hand, the *field-emission mode* implies bias ranging from 25 to 300V and a tunneling current from 1 to 10nA, resulting in a larger tip-sample distance. The excitation area is therefore bigger and photons are collected from surface areas in the order of 1x1 μm^2. With this last method, the sample is excited by high energy-electrons that induce not only radiative excitation but also finite damage at the sample surface.

The measurements of lateral dimensions of particles in STM are in general associated with a significant error, which results from the convolution of the tip geometry and the respective surface corrugation, as shown in Figure 3.11b. To take this effect into account, a factor of 1.5 in the lateral dimensions is used to transform the measured values into the real ones.

3.2.2 Low Energy Electron Diffraction (LEED)

LEED is employed as a simple and straight-forward diffraction technique in our studies of single crystal surfaces. It probes the long-range order of periodic surface structures and yields valuable information also on partially disordered systems, even if a complete structural analysis cannot be performed in this case.

The basis is the interference of electrons at surfaces, as related to the de Broglie equation $\lambda = h/mv$. In the case of wave scattering at a periodic array in two dimensions, constructive interference takes place if the scattered waves from successive lattice planes have path differences of multiples of the wavelength λ. This interpretation is widely known as the "Bragg equation":

$$n\lambda = 2d \sin \Theta \ . \tag{3.1}$$

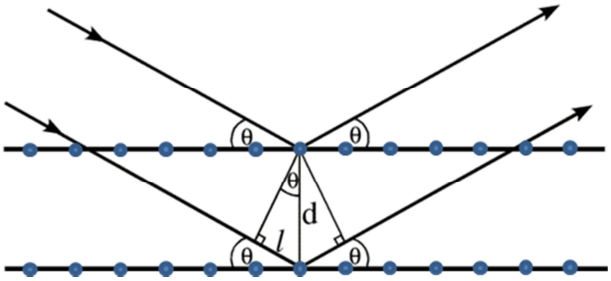

Figure 3.12. Representation of scattered waves and their path difference. Adapted from [111]

In this equation, d means the distance between two adjacent lattice planes, Θ is the angle between incident beam and surface plane and n an integer. This technique delivers information of the interatomic distance in the reciprocal space. Because of the surface sensitivity of the method, it is necessary to perform LEED experiments in ultra-high vacuum ($p<10^{-8}$ mbar) and on atomically "clean" surfaces [112].

Chapter 4

The Zinc Oxide Au(111) System

This chapter aims to find a correlation between the morphological properties and the optical activity in the presented system. First, we provide a general introduction to zinc oxide, followed by the growth behaviour and the optical properties [113-115]. In the last sections, we intend to modifiy this optical properties via deposition of metal particles on the ZnO surface [116] and we describe a three dimensional nanostructured growth mode adopted by the material [117].

4.1 Introduction to ZnO

Zinc Oxide is a fascinating semiconducting material with a direct band gap of 3.37 eV and a large exciton binding energy of 60 meV at room temperature [28, 118]. Due to these highlighting properties, ZnO has broad applications in electronic, optoelectronic, electrochemical, and electromechanical devices, for instance as ultraviolet lasers, light emitting diodes, field emission devices, high performance nanosensors, solar cells, piezoelectric nanogenerators, and nano-piezotronics, among others. In particular, one-dimensional (1D) ZnO nanostructures are of special interest due to their large surface-to-volume ratio. They have been produced by a wide range of techniques, such as wet chemical methods, physical vapour deposition, metal-organic chemical vapour deposition (MOCVD), molecular beam epitaxy (MBE), pulsed laser deposition, radio frecuency (RF) magnetron sputtering, electrospinning, and even top-down approaches, including etching. While sometimes high temperatures are required in those techniques in order to produce the desired structures, others are proceeding without heating by the use of catalysts. Compared to the bulk or thin film materials, ZnO nanostructures sometimes achieve higher efficiency in catalytic or optical processes due to their high surface-to-volume ratio, as those may facilitate light absorption or charge transfer processes [119], among many other effects.

The following list aims to describe some of the properties that distinguish ZnO from other semiconductors or oxides, making it useful for a broad spectrum of applications [120]:

- A direct and wide band gap of 3.44 eV and 3.37 eV at low and room temperatures, respectively [121]. As mentioned above, this makes ZnO suitable for applications in optoelectronics in the blue/UV region, in the fabrication of light-emitting diodes, laser diodes or photodetectors [28, 118]. Also optically pumped lasing has been found in ZnO platelets [122], thin films [123], clusters [124] and nanowires [125].
- A large exciton binding energy of 60 meV. This indicates that efficient excitonic emission in ZnO can survive at room temperature and higher [122, 123, 126].

- A large piezoelectric constant. An applied voltage causes a deformation in the crystal due to the low symmetry of the wurtzite lattice structure combined with a large electromechanical coupling inside it.
- Strong luminescence. Apart from the band gap recombination, defects and vacancies inside the lattice are the main sources of light emission from ZnO [113, 114]. This topic is discussed in section 4.3.
- A strong sensitivity of surface conductivity to the presence of adsorbed species. This advantage is used for the production of chemical sensors [127]. The effect is based on electron accumulation in the surface layer of annealed single crystals in vacuum. It disappears after exposure to ambient conditions or gases due to reverse band bending [128, 129].
- A strong non-linear resistance of polycrystalline ZnO. This non-linear resistance is normally caused by grain boundaries [130].
- Large non-linear optical coefficients. Non-linear optical devices may benefit from the use of the second- and third-order harmonics of ZnO, depending on the crystallinity of the samples [131].
- High thermal conductivity. This feature makes ZnO useful as an additive that promotes heat removal during device operation [132].
- Availability of large single crystals. Bulk crystals can be grown, offering a variety of terminations [28].
- Amenability to wet chemical etching. This property makes ZnO accessible to semiconductor device fabrication.
- Radiation hardness. This makes ZnO suitable for applications at high altitude or in space [133, 134].

In addition, zinc oxide plays nowadays an important role in reaction mechanisms for methanol synthesis. Most of the commercial available catalysts for methanol synthesis and for the water-gas shift reaction on the low temperature regime contain zinc, apart from the main active component: copper metal. The presence of ZnO in these catalysts enhances catalyst life, selectivity and activity [135].

In this thesis, we focus on two fundamentally different behaviours of ZnO growth. In a first approach, we grow crystalline ZnO films that maintain high surface quality even at large thicknesses. On the other hand, the formation of three dimensional nanostructures is studied, which correspond to ZnO nanorods. We discuss the parameters that are decisive for this type of growth. In both cases, the systems are studied using surface-science tools that imply working with high purity samples and deposition techniques in Ultra-High-Vacuum (UHV), as described in section 3.2. Even though the growth of 3D ZnO nanostructures has been already studied in the past, we were able to obtain new information on the mechanism, exploiting state of the art surface science techniques at ultra clean conditions. The aim of this chapter is, however, to present the results of the closed ZnO films, which includes a discussion of their growth as well as their optical features. A more detailed investigation of the optical properties of ZnO is presented later in section 4.3.

In the following sections, some general properties of ZnO will be introduced, such as its crystal structure, polarity, and electronic band structure, which are particular for bulk ZnO but can be extended to the case of thin films studied in this thesis.

4.1.1 Crystal Structure

Most of the group II-VI binary compound semiconductors crystallize either in two ways: *(i)* cubic zinc-blende, or *(ii)* hexagonal wurtzite lattices. In the last configuration, each anion is surrounded by four cations at the corners of a tetrahedron, and vice versa. This tetrahedral coordination is typical of *sp3* covalent bonding; however, the materials in this configuration also have a substantial ionic contribution. ZnO is a II-VI compound semiconductor whose iconicity resides at the borderline between covalent and ionic materials. The crystal structures adopted by ZnO are wurtzite, zinc blende, and rocksalt. However, at ambient conditions, the thermodynamically most stable phase is wurtzite. The zinc-blende structure can be stabilized only by growing it on cubic substrates. On the other hand, the rocksalt configuration (NaCl) may be obtained at relatively high pressures [28].

The wurtzite structure has a hexagonal unit cell with two lattice parameters, a ≈ 3.249 Å and c ≈ 5.206 Å, with ideal ratio of $c/a = \sqrt{8/3} = 1.633$. Figure 4.1 depicts a schematic representation of the wurtzitic ZnO structure.

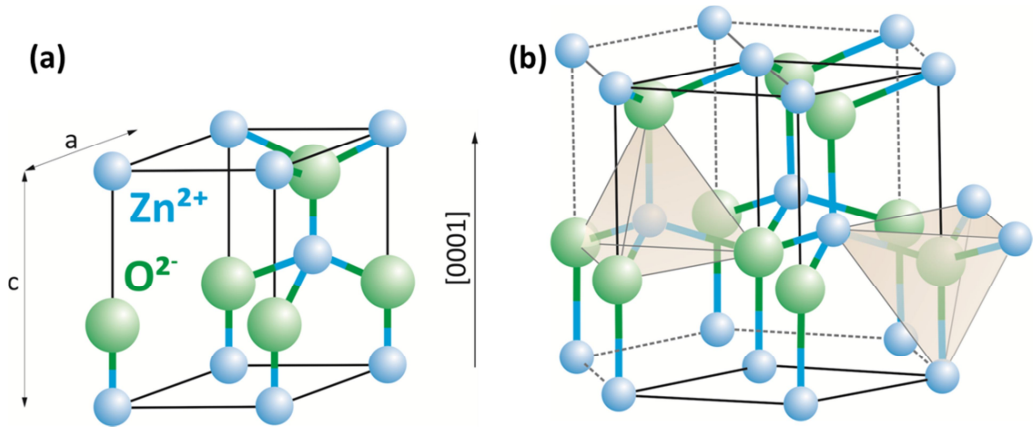

Figure 4.1. Crystallographic structure of ZnO at room temperature: wurtzite, with main parameters *a* and *c*. (a) unit cell, and (b) wurtzite structure. Adapted from [136]

ZnO has already a substantial fraction of ionic binding. Based on the concept of ionic binding, the bottom of the conduction band is formed essentially by the 4s levels of the Zn^{2+} ions and the top of the valence band by the 2p levels of the O^{2-} ions. The gap between conduction band and the highest edge of the valence band is around 3.437 eV at low temperatures. The situation for elements containing *d* electrons exhibits mixing effects coming from the overlap of atomic potentials [137]. In this case, Zn 3d levels mix with 4s levels. Both experimental and theoretical results conclude that Zn 3d states are found 10.5 eV below the Fermi Energy, after being considered as part of the valence band [138, 139].

4.1.2 Band Structure

The band structure of a given semiconductor is essential for determining its potential utility. As a consequence, good knowledge of the band structure is critical if the

material is considered for device applications. Besides, the band structure gives the electronic one-particle (electron or hole) states. ZnO is a direct semiconductor, which means that the top of the valence and the bottom of the conduction bands (VB and CB, respectively) are at the same point in the Brillouin zone. In other words, the zone at $k = 0$ at the Γ-point is of main interest. As mentioned in the last paragraph, the lowest CB is formed from the empy 4s states of Zn^{2+} or the antibinding *sp3* hybrid states. The effective electron mass m_e is almost isotropic with a value of around $m_e = (0.28 \pm 0.02)m_0$.

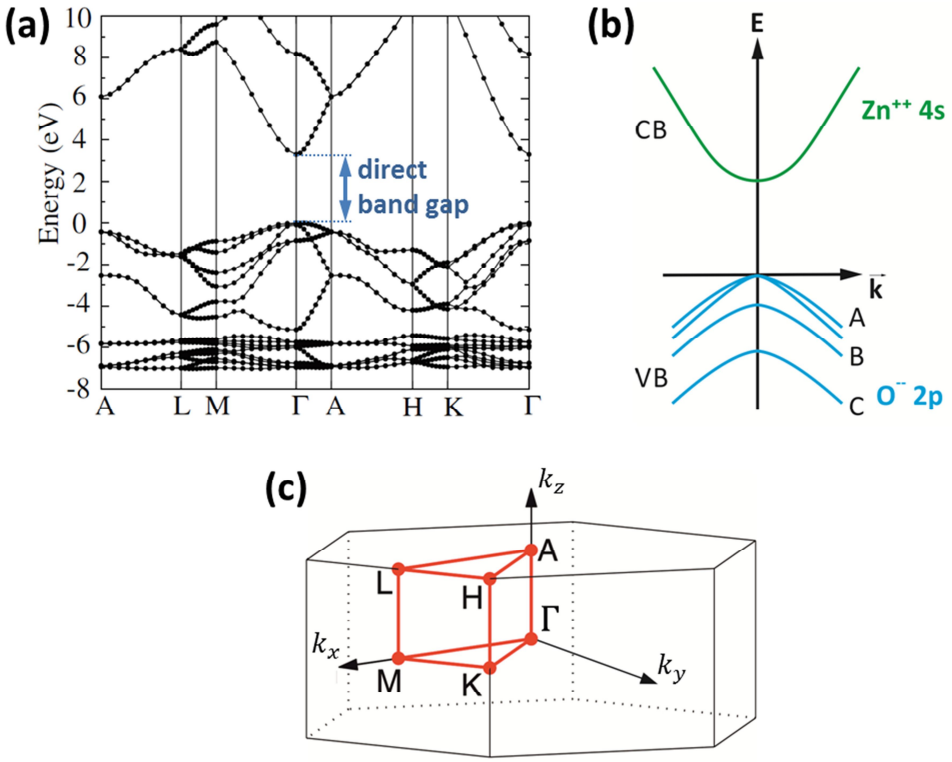

Figure 4.2. (a) Calculated band structure of ZnO, where the energy of the valence-band maximum was set to zero [120]. (b) Energy schema of ZnO in the Γ-point. Note the splitting in the VB due to the spin-orbit coupling. Adapted from [27]. (c) First Brillouin zone in the reciprocal space of the wurtzite lattice and the points of interest. Adapted from [140]

The valence band (VB), which originates from occupied 2p orbitals of O^{2-}, or the binding *sp3* orbitals, is split due to the influence of the hexagonal crystal field into two states. The inclusion of the spin gives a further splitting due to spin-orbit coupling into three two-fold-degenerate sub-VB's (see Figure 4.2b). These VB's are labelled in all wurtzite-type semiconductors, like ZnS, CdS, CdSe, or GaN from higher to lower energies as A, B, and C bands.

The splitting of the A and B valence bands is only of the order of 5 meV and the selection rules for allowed transitions are essentially the same. The effective hole masses in ZnO are rather isotropic and similar for the A, B, and C VBs with typical values of:

$$m_{h\perp,\parallel A,B} = 0.59\, m_0 \ , \ m_{h\parallel C} = 0.31\, m_0 \ , \ m_{h\perp C} = 0.55\, m_0 \ .$$

The concept of effective mass depends directly on the direction, as is can be seen in the last three expressions.

4.1.3 Polarity

The ZnO crystal exhibits crystallographic polarity, as some of the possible terminations possess no inversion symmetry. The polarity indicates the direction of the bonds. In the zinc-blende and rocksalt structures, these directions are in the closed-packed (111) planes, whereas the corresponding (0001) basal planes in the wurtzite lattice differ from $(\bar{1}\bar{1}\bar{1})$ and $(000\bar{1})$ planes, respectively. The adopted convention says that the $[0001]$ axis points from the face of the O plane to the Zn plane and is the positive *z* direction. In other terms, when the bonds along the *c* direction are from cation (Zn) to anion (O), the polarity is referred to as Zn polarity. In the same way, when the bonds along the *c* direction are from anion (O) to cation (Zn), the polarity is referred to as O polarity. Many properties of the material depend on its polarity, such as the growth, etching, defect generation and plasticity, spontaneous polarization, and piezoelectricity. In ZnO with wurtzite structure, in addition to the primary polar plane (0001) and associated direction $\langle 0001 \rangle$, many other secondary planes and directions exist in the crystal configuration. However, the (0001)-type of surfaces and directions are most commonly found to govern the growth of the material.

The control of the film polarity plays an important role in epitaxial growth of ZnO. When the film is grown in the $[0001]$ direction, Zn polarity (+c) is obtained and the top surface is Zn terminated. On the other hand, when the growth is in the $[000\bar{1}]$ direction, O polarity (-c) is observed and the top surface is O terminated. Much effort has been invested to determine the effects of the polarity and to find a way to control it during growth. Depending on the substrate and the used technique, different terminations (Zn or O) are obtained. However, the energetically preferred growth direction of ZnO is normally the (0001) axis, along which Zn and O planes alternate in a regular way. In order to avoid divergence of the electrostatic energy, the associated surface dipole needs to be quenched at a critical film thickness by one of the following ways that include surface hydroxylation [141], metallization [142, 143], or nonstoichiometric surface compositions [144, 145]. All of these processes are able to compensate the concomitant dipole along the surface normal.

4.1.4 Intrinsic Defects

The simplest imperfection is a *lattice vacancy*, which is nothing more than a missing atom or ion. It is also called *Schottky defect*. A *Schottky defect* is created in a perfect crystal when transferring an atom from a lattice site in the interior to a lattice site on the surface of the crystal. Lattice vacancies are always present in thermal equilibrium in an otherwise perfect crystal, due to the increase of entropy by a disorder in the structure [146].

The probability for a lattice site to be vacant is proportional to the Boltzmann factor for thermal equilibrium: $P = e^{-E_V/k_B T}$, where E_V is the energy required to take an

atom from a lattice site inside the crystal to a lattice site on the surface, or, in other words, the *formation energy*. In the presence of N atoms, the equilibrium number n of vacancies is described by

$$\frac{n}{N-n} = e^{\frac{-E_V}{k_B T}} . \tag{4.1}$$

For the case that $n \ll N$, then

$$\frac{n}{N} \cong e^{\frac{-E_V}{k_B T}} . \tag{4.2}$$

This last equation shows that the equilibrium concentration of vacancies decreases as the temperature decreases. Thus, the concentration of vacancies will be bigger than the equilibrium value if the crystal is grown at an elevated temperature and then cooled suddenly. Hence, vacancies are frozen and are not able to diffuse inside the lattice. This effect is particularly important in our case, as it is considered as the fundamental basis for the creation of intrinsic defects in the oxide lattice. Figure 4.3 shows the common defects in the ZnO structure that are going to be analyzed along this chapter.

In ionic crystals, however, it is usually energetically convenient to form roughly equal numbers of positive and negative ion vacancies. The crystal is, hence, kept electrostatically neutral due to the formation of pairs of vacancies on a local scale. From statistical methods it is derived that

$$n \cong N\, e^{\frac{-E_p}{2k_B T}} \tag{4.3}$$

for the numbers of pairs, in which E_p represents the energy formation of a pair.

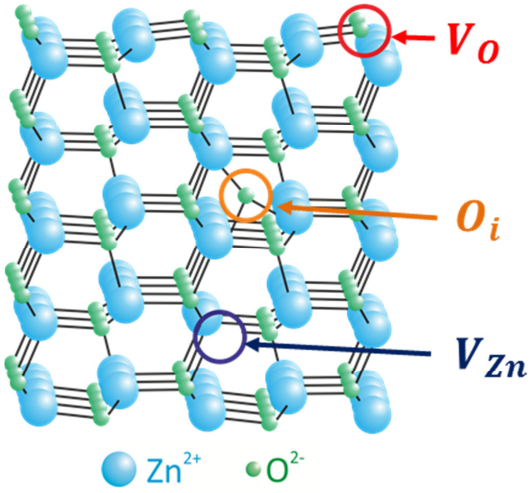

Figure 4.3. The crystalline ZnO $(10\bar{1}0)$ structure with Schottky and Frenkel defects. Oxygen vacancy is indicated with red circle, while Zn vacancy is marked in blue, also Schottky defect. Frenkel defect is marked in orange: oxygen interstitial. All these defects are involved in the light emission, as described in this chapter.

Another type of lattice defect is the *Frenkel defect*, as depicted in Figure 4.3. In this case, an atom is transferred from a lattice site to an *interstitial position*, a position not normally occupied by an atom. The following equation is valid, providing that the number n of Frenkel defects is much smaller than the number of lattice sites N and the number of interstitial sites N':

$$n \cong \sqrt{N\,N'}\; e^{\frac{-E_I}{k_B T}} \quad , \tag{4.4}$$

in which E_I stands for the energy necessary to remove an atom from a lattice site to an interstitial position.

The formation energy of a point defect in the ZnO lattice is strongly dependent on the growth or annealing conditions, as it is shown in Figure 4.4 [120, 147]. Particularly, the relative abundance of Zn and O atoms in the environment determines the formation energy of point defects in the ZnO lattice. The formation energy of an oxygen vacancy is expressed via the chemical potentials μ_{Zn} and μ_O, respectively. In the case that the vacancy is charged, the formation energy also depends on the Fermi level E_F, as it is also seen in Figure 4.4 (positive and negative slopes) This level represents the energy of the electron reservoir and can be thought to be an "electron chemical potential". The formation energy of an oxygen vacancy in ZnO is described by the following expression:

$$E^f\left(V_O^q\right) = E_{tot}\left(V_O^q\right) - E_{tot}\,(ZnO) + \mu_O + q(E_F + E_{VBM}), \tag{4.5}$$

where $E_{tot}\left(V_O^q\right)$ is the total energy of a supercell containing the oxygen vacancy in the charge state q, $E_{tot}(ZnO)$ represents the total energy of a perfect ZnO crystal in the same supercell and μ_O stands for the oxygen chemical potential. In general, all native point defects are described by equations similar to (4.5). A further description of the chemical potential and its properties is found in section 4.5.2, as it plays a key role for the growth behaviour of ZnO.

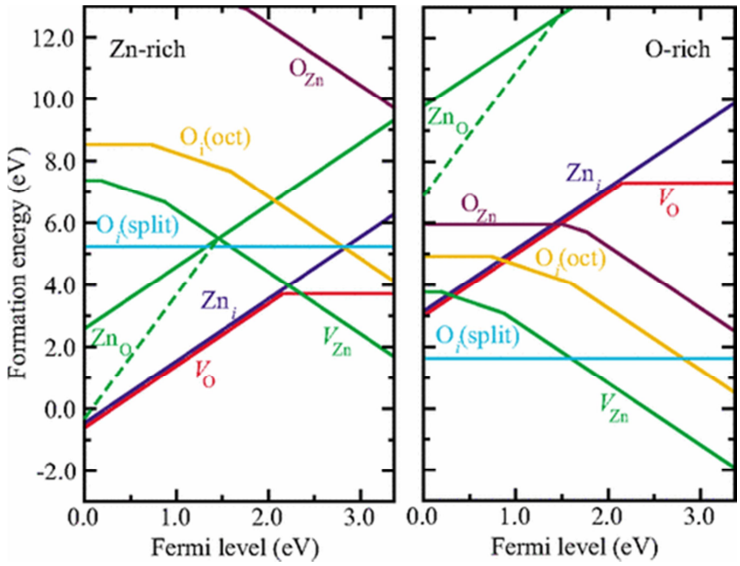

Figure 4.4. Formation energies as a function of Fermi-level position for native point defects in ZnO for Zn-rich (left) and O-rich conditions (right). The zero of Fermi level corresponds to the valence-band maximum. The slope of the segments indicates the charge state. Kinks in the curves indicate transitions between different charge states (from [26]). The defects are described by the Kröger-Vink notation. The oxygen atoms can occupy the octahedral interstitial sites or form split interstitials, in which it shares a lattice site with one of the nearest-neighbour substitutional oxygen atoms.

4.1.5 Impurities

Certain types of impurities and imperfections in the lattice can drastically affect the properties of a semiconductor, such as the conductivity or the optical properties. As an example, the addition of boron to silicon just in the proportion of 1 boron atom to 10^5 silicon atoms increases the conductivity of pure silicon by a factor of 10^3 at room temperature. In a compound semiconductor, the deficiency of one constituent in the stoichiometry will act as an impurity. Such semiconductors are called *deficit semiconductors*. The effect of adding impurities to a semiconductor is called *doping* and leads to an *extrinsic* semiconductor. On the other hand, an *intrinsic* semiconductor is a pure semiconductor without any significant dopant species present.

This section aims to give a general description of impurities effects [146]. For simplicity reasons, these effects are presented for the silicon structure, which crystallizes in the diamond configuration. In this case, each atom forms four covalent bounds, one with each of its nearest neighbors, corresponding to the chemical valence of four. If an impurity atom of valence five, such as phosphorus, arsenic, or antimony, is substituted in the lattice at the position of a normal atom, there will be one valence electron from the impurity atom left over. This situation takes places after the four covalent bonds are established with the nearest neighbors. In other words, the impurity atom has been accommodated in the structure with as little disturbance as possible. However, one electron is donated to the CB of the semiconductor.

Donor and Acceptor States

The schematic picture of Figure 4.5a shows a positive charge on the impurity atom, which has lost one electron. Crystallographic studies have demonstrated that the pentavalent impurities get inside the lattice by substitution of a normal atom, without creating interstitial positions. These impurity atoms that can give up an electron are called *donors*. As the electron remains in the crystal, the crystal as a whole remains neutral. The binding energy of the donor impurity can be estimated by an extension of the Bohr's theory for a hydrogen atom.

The binding energy of an atomic hydrogen is $E_0 = -\frac{e^4 m_0}{2\,(4\pi\varepsilon_0\hbar)^2} = -13.6\ eV$, and the Bohr radius of the ground state of hydrogen is $a_0 = \frac{4\pi\varepsilon_0\hbar^2}{m_0 e^2} = 0.529\ \text{Å}$. Taking into account both the dielectric constant of the medium and the effective mass of an electron in the periodic potential of the crystal, one obtains:

$$E_d = \frac{e^4 m_e}{2(4\pi\varepsilon\varepsilon_0\hbar)^2} \tag{4.6}$$

for the donor ionization energy in the semiconductor. The modified Bohr radius results:

$$a_d = \frac{4\pi\varepsilon\varepsilon_0\hbar^2}{m_e e^2} \quad . \tag{4.7}$$

As the squared dielectric constant enters the equation, it has an important effect on the donor energy. The effective mass enters only as the first power, making it less relevant.

In order to get a general idea of the impurity levels, we can use the standard values for silicon, $m_e = 0.2\, m_0$ and the static dielectric constant $\varepsilon = 11.7$. The ionization energy E_d in this model is 20 meV, being lower by a factor of $m_e/m_0\varepsilon^2 = 1.46\, x\, 10^{-3}$ as compared to the binding energy of the atomic hydrogen. Thus, the radius of the first Bohr orbit is 30 Å in silicon. This value is increased by $\varepsilon m_0/m_e$ as compared to the value of 0.53 Å that corresponds to the free hydrogen atom. The value in silicon is so large, that the impurity orbits overlap at relatively low impurity concentrations, changing substantially the electronic properties of the material. As a comparison, for the case of ZnO, taking into account $\varepsilon = 3.7$ [148] and $m_e = 0.28\, m_0$, as seen in section 4.1.2, it results in an ionization energy of $E_d = 0.27\, eV$ and a modified Bohr radius of $a_d = 7$ Å .

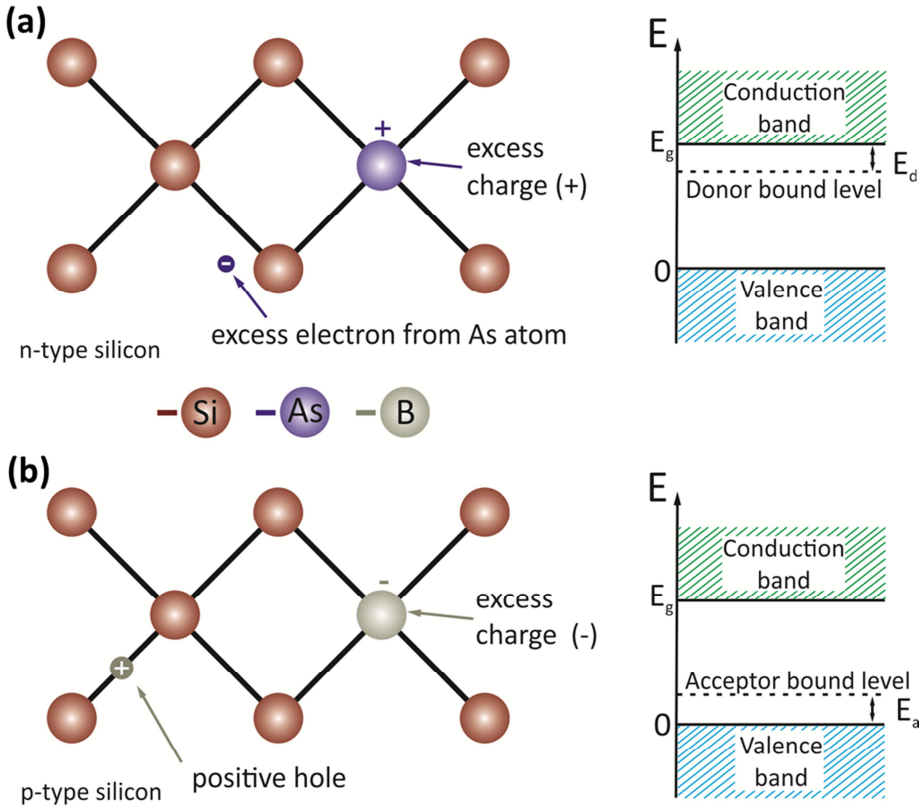

Figure 4.5. Silicon crystal structure doped with (a) donor impurities and (b) acceptor impurities. The binding energy for each case is shown on the right schema. The figure aims to show the possible positions of electrons and holes added due to the impurities.

On the other hand, just like an electron bounds to a pentavalent impurity, a hole may be bound to a trivalent impurity in germanium or silicon, as depicted in Figure 4.5b. Trivalent impurities can accept electrons from the valence band, leaving holes in the band. Hence, these impurities are called *acceptors*. For the case of silicon in particular, elements like boron, aluminum, gallium and indium are good acceptors. When an acceptor is ionized, there is a free hole, which requires an input of energy. In a conventional energy band diagram, an electron rises when it gains energy, whereas a hole sinks by gaining energy. The same Bohr model developed before applies

qualitatively for holes as well as for electrons. However, the degeneracy at the top of the valence band makes the effective mass problem more complex, but a deep analysis of this situation goes beyond the aim of this section.

If donor atoms are present in larger numbers than acceptors, the thermal ionization of donors will release electrons into the conduction band. Thus, electrons will control the conductivity of the specimen and the material is called *n-type*. On the contrary, if acceptors are dominant, holes will be released into the valence band and the conductivity will be controlled by holes, rendering the material *p-type*. The same concept can be forwarded to ZnO, which is always n-type due to the presence of hydrogen in the lattice. In most of the growth methods, hydrogen ionizes at low temperatures, producing an electron-hole pair [120].

N-type Doping

The substitution of Zn or O atoms in the lattice is one possibility to achieve n-type doping in ZnO. These substitute atoms should be replaced by atoms that have one electron more in the outer shell than the original ones. As a consequence, the group III elements, like Al, Ga, and In are potential donors for the Zn cations, according to the following expression:

$$D^0 \Leftrightarrow D^+ + e^- \quad , \tag{4.8}$$

where D^0 and D^+ represent the neutral and the ionized donor, respectively. The right term in equation (4.8) describes the equilibrium condition at low temperature.

Another possibility for n-doping would be group VII elements on the anion site. Even though this combination is known to be very efficient, it has been less investigated for ZnO. However, the role of hydrogen in the electronic properties of ZnO has drawn the attention in the last time. First-principles calculations have shown that interstitial hydrogen behaves as a shallow donor, as only the positive charge state H_i^+ is thermodynamically stable. The behaviour of hydrogen in ZnO is extremely unusual. In most of the semiconductors studied to date, interstitial hydrogen has been found, theoretically as well as experimentally, to act as an *amphoteric* impurity [149, 150]. In p-type material, hydrogen incorporates as H_i^+, and in n-type material as H_i^-, always compensating the prevailing conductivity of the material. The amphoteric behaviour excludes hydrogen from acting as a dopant, i.e. from being a source of conductivity. Surprisingly, interstitial hydrogen in ZnO occurs exclusively in the positive charge state, acting always as a donor [120].

Apart from interstitial positions, hydrogen can also replace oxygen in the ZnO lattice (H_O). Substitutional hydrogen H_O is also a shallow donor in ZnO, entering exclusively in the positive charge state H_O^+ [151]. Both substitutional and interstitial forms of hydrogen have low formation energies, which means that they can occur in significant concentrations [151]. Therefore, hydrogen is a very attractive candidate for an impurity that can be unintentionally present, giving rise to a background n-type conductivity. However, a deeper analysis of this background conductivity in ZnO exceeds the aim of this thesis and will not be further discussed.

P-type Doping

According to the interpretation described above, it would be expected that the elements Li, Na, or K of the group I may be good acceptors on the Zn site. Indeed, the elements Li, Na, K and also the Ib elements Cu and Ag can be introduced as acceptors in the wurtzite lattice. However, they normally form deep acceptors with ionization energies around a few hundred meV. These energies are much larger than k_BT at room temperature, so that the following equation mainly occurs from the right to the left at room temperature:

$$A^0 \Leftrightarrow A^- + h^+ \ . \tag{4.9}$$

From the practical point of view, the fabrication of p-type ZnO for technological applications still possess a large problem. Many doping strategies were tested without success to fabricate a p-conductive ZnO material. The problems may exist due to various physical limitations, such as *(i)* the intrinsic presence of excess electrons in the as grown material, *(ii)* the low formation energies of native ZnO defects that cancel the p-type character, and *(iii)* the inadecuate position of acceptor levels that are often too deep in the band gap to enable thermal activation at room temperature [118, 152].

In order to achieve p-type conductivity of ZnO, nitrogen doping was considered to be a promising approach. Even though good advances have been made in the last years, the fabrication of a genuine p-doped material is still not possible. In principle, nitrogen should be easily introduced in the wurtzite lattice without a lot of strain, due to the similarity between oxygen and nitrogen in terms of atom radii and electronic structure. The nitrogen ions are expected to enter the lattice in two distinct configurations: *(i)* as a substituent on the oxygen sites N_O, or *(ii)* as defect complexes in combination with Zn (N_O-V_{Zn}) or oxygen vacancies (N_{Zn}-V_O) [153, 154]. In agreement with theoretical calculations, the impurity ions have the tendency to induce a deep acceptor level in the ZnO band gap. This effect gives rise to a broad luminescence peak situated at ~730 nm [155, 156]. Indeed, this peak has been already observed in ZnO single crystals that were modified by traces of nitrogen [157]. Unfortunately, the nitrogen-doped sample showed low carrier mobility and could therefore not be considered as a p-type semiconducting oxide.

Section 4.3.2 of this thesis deals with investigations of optical and electronic properties of nitrogen-doped ZnO thin films [115]. We make use of luminescence spectroscopy with the STM to unravel the electronic characteristics of the N-dopants. We reproducibly found a 730 nm peak in the experiments. In conflict to earlier interpretations that attributed this emission to N-dopants, it was assigned to oxygen vacancies that were found to develop easily in n-doped ZnO, as discussed in section 4.3.1.

4.1.6 Moiré Pattern

The nonlinear interaction of optical patterns of lines creates a real and visible pattern of roughly parallel dark and light bands, which is called the *Moiré pattern* and is superimposed on the original lines [158]. The Moiré pattern is a secondary and visually evident superimposed pattern created, for example, when two identical patterns on a

flat surface are overlaid while displaced or rotated a small amount from one another, as it can be seen in Figure 4.6. This optical effect can be found in many fields, such as the aggrupation of molecules on a metal surface [15] or the formation of the very first layers of a thin film, as it will be described in section 4.2.2.

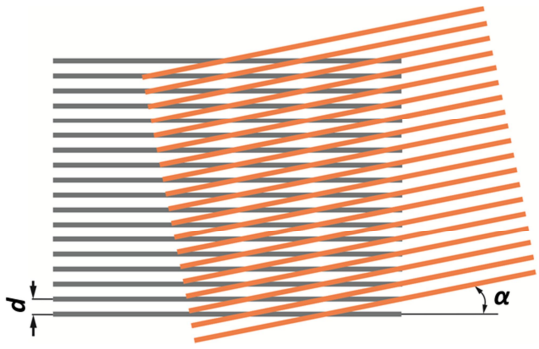

Figure 4.6. Moiré pattern obtained from the superposition of two patterns with rotation angle α

4.2 Growth of ZnO Thin Films on Au(111)

In this part of the thesis, a new approach to grow crystalline ZnO films is presented. This approach maintains a high surface quality even at large thicknesses of the films. As starting point, we have chosen the Au(111) surface that shares the hexagonal symmetry with ZnO(0001) and can be treated at sufficiently high temperature to reach thermodynamic equilibrium. The ZnO films are typically 1 to 30 ML thick. This thickness is large enough to develop the band gap of bulk ZnO.

4.2.1 ZnO Thin Film Preparation

The Au(111) single crystal used as support for the ZnO was cleaned by repeated cycles of Ar^+ sputtering and annealing to 1100 K. Normally, three cycles of 1 hour sputtering and half an hour annealing were enough to obtain a clean gold surface. This produces a sharp p(1x1) LEED pattern of the *hcp* Au(111), which is shown in the inset of Figure 4.7c. A typical atomically flat gold surface is seen in the STM images of Figure 4.7, where the monoatomic steps are depicted. In a more detailed view, the Herringbone reconstruction that is characteristic for the (111) surface is also seen (Figure 4.7b). The white spots sitting on some elbows of the reconstruction are interpreted as adsorbates. At this point, also the calibration of the *xyz* parameters is done.

Light emission from a bare Au (111) sample was also checked in order to calibrate the optical system. A typical spectrum obtained at low bias (3.3V and 5nA) is shown in Figure 4.7c. The tip induced plasmon resonance is clearly seen at ~730 nm, which is considered to be a third tool to evaluate the cleanliness of the substrate. The wavelength of the tip-induced plasmon depends strongly on the tip shape and the bias conditions, as described in section 2.1.3.

After sample cleaning, ZnO pellets were evaporated from a Mo crucible in 5×10^{-5} mbar O_2 and deposited onto the clean gold surface at room temperature. The preparation was finished by annealing the films to temperatures between 600 and 800 K in an O_2 ambient of 5×10^{-5} mbar.

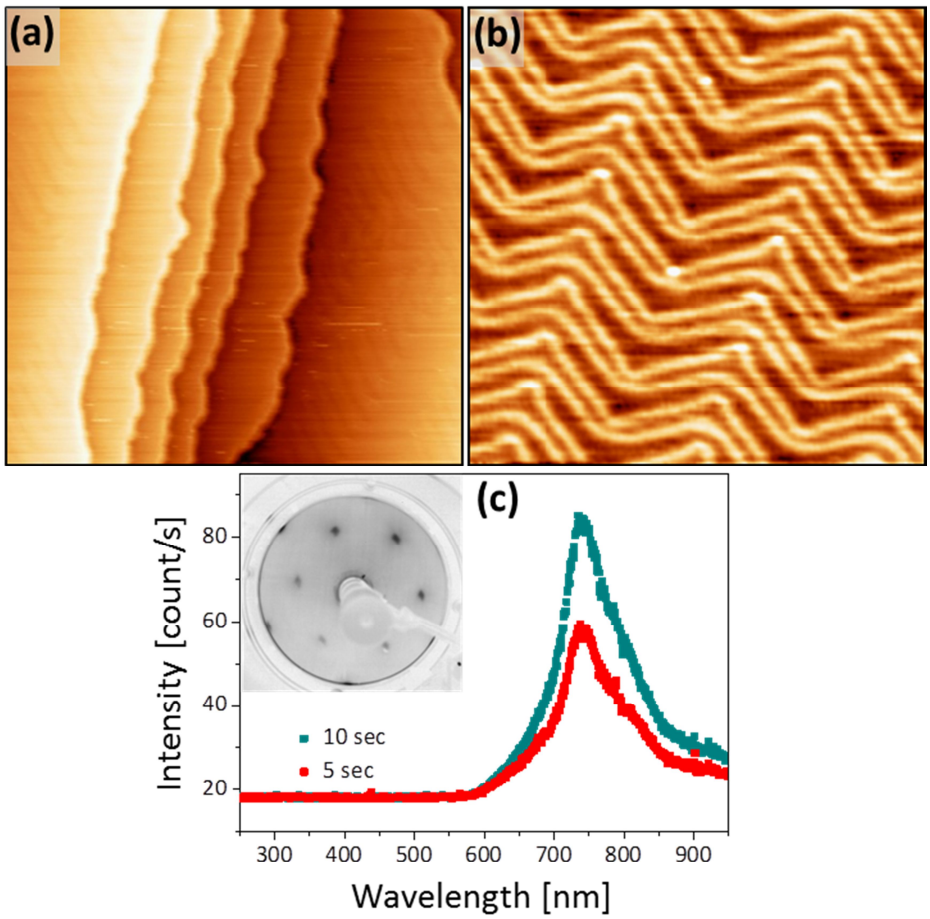

Figure 4.7. (a) STM topographic image of an atomically clean Au(111) surface (120x120 nm^2, 0.7V, 1nA). (b) Herringbone reconstruction of the surface (50x50 nm^2, 2.6V, 1nA). (c) Tip induced Au plasmon taken at 3.3V and 5nA. The maximum in the spectrum reflects the dielectric properties of the gold. Note that Herringbone reconstruction can be observed in both (a) and (b). LEED pattern taken at 100 eV can be seen in the inset of (c).

4.2.2 Structure and Morphology of ZnO Thin Films

In the case of small exposure and high annealing temperature (T>750 K), isolated ZnO nanocrystallites developed on the Au(111) surface as it is depicted in Figure 4.8a. The typical deposits are up to 6 nm in height and 20 nm in diameter and feature distinct triangular or hexagonal shapes. Their height-to-diameter ratio is around 0.3, indicating that the oxide film already dewets from the metal support in this temperature range. The aim of our studies was to concentrate on the properties of compact films, so that we did not explore the ZnO crystallites any further. Films that cover the entire Au(111) surface have been obtained at higher ZnO load and lower annealing temperatures. An

example for a film of 1-2 ML nominal thickness is shown in Figure 4.8b. Its surface is covered with a hexagonal dot-pattern of 2.2 nm periodicity, being assigned to a Moiré superstructure, as explained in section 4.1.6.

Based on the experimental cell size and the ZnO bulk lattice constant, the Moiré superstructure mentioned above is traced back to (7×7) ZnO(0001) unit cells overgrowing (8×8) cells of the non-reconstructed Au(111) support. This effect yields a hexagonal superstructure with 2.3 nm periodicity (Figure 4.10a). This agreement with the experiment data is even better if a small lattice expansion (+3 %) is assumed for the interfacial ZnO planes. The wurzite lattice in the limit of thin films tends to undergo a tetragonal distortion in which the vertical lattice parameter is reduced with respect to the in-plane one in order to lower the effect of polarity [159]. As a result, the moderate increase of +3% in the lattice expansion seems to be reasonable. The signs of the tetragonal dislocation of ZnO/Au(111) are clearly seen in the inset of Figure 4.8b. Here, a clear increase of the step height with film thickness is observed.

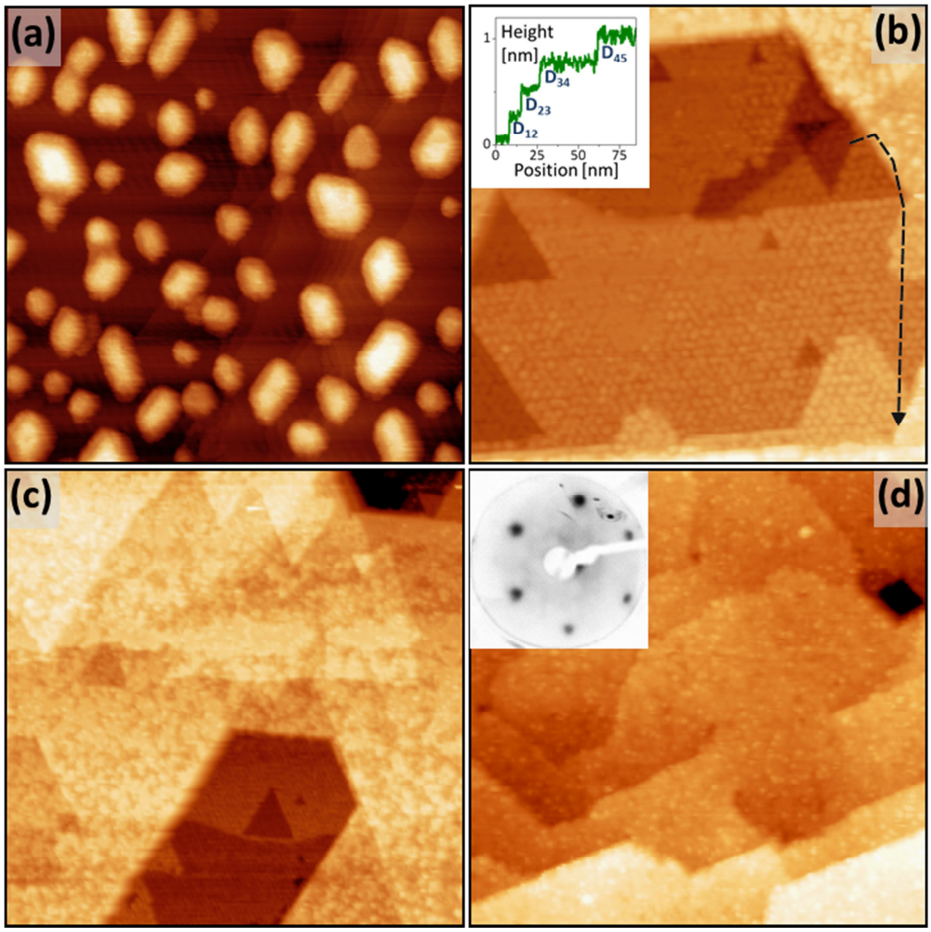

Figure 4.8. Overview STM images of (a) ZnO nano-islands (1.6 V, 160 × 160 nm^2) and compact films of (b) 3 ML (80 × 80 nm^2), (c) 8 ML (160 × 160 nm^2) and (d) 15 ML (160 × 160 nm^2) nominal thickness grown on Au(111). The inset in (b) displays a height profile across the first four ZnO layers. Measured step heights are D_{12} = 2.2 Å, D_{23} = 2.4 Å, D_{34} = 2.6 Å, and D_{45} = 2.6 Å. The inset in (d) shows the LEED pattern of the 15 ML film taken at 80 eV [113].

It is important to highlight that STM images that show the Moiré superstructure give no hint for a preservation of the Au(111) herringbone reconstruction beneath the ZnO. Hence, we propose that the gold reconstruction is lifted during oxide growth, a behavior that has been found for many other dielectric and molecular overlayers on the Au(111) surface before [160]. Our tentative model, growth of a strained ZnO(0001) layer on the unreconstructed Au(111) surface, gets corroborated by LEED measurements that show only the plain hexagonal spot pattern of ZnO(0001) (Figure 4.8d, inset). The Moiré structure is not resolved in the diffraction pattern due to the small coherence length of our LEED system and the finite size of adjacent superstructure domains.

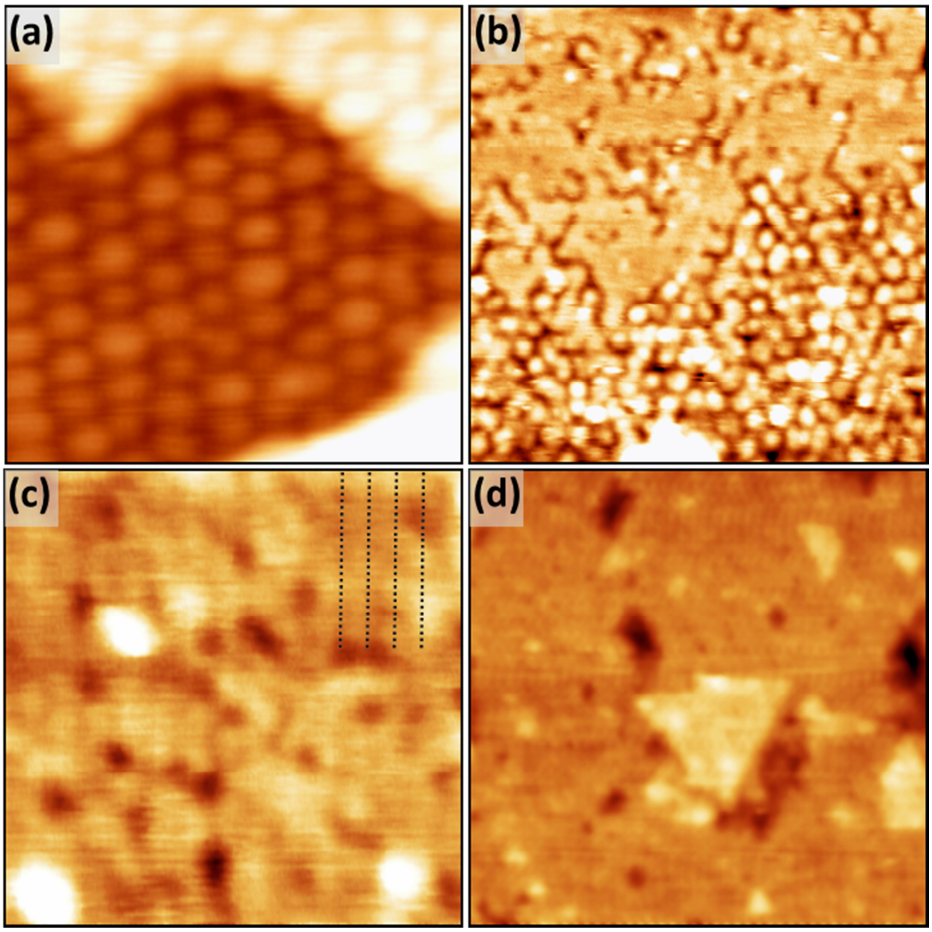

Figure 4.9. Close-up images of (a) the ZnO/Au(111) Moiré pattern (1st ML, 20×20 nm^2), (b) the transition range between Moiré pattern and flat surface (4th ML, 60×60 nm^2), (c) the (2×1) stripe pattern indicative for a hydrogen super-structure (7th ML, 10×10 nm^2) and (d) the featureless surface of a 15 ML thick film (100×100 nm^2).

For the first four oxide layers, the Moiré pattern remains visible in the STM with constant in-plane periodicity and constant corrugation (Figure 4.8c). The measured corrugation of ~1Å is independent of the bias voltage, suggesting that the contrast is mainly of geometric origin and not induced by a modulated ZnO state-density. A more careful analysis reveals that not all Moiré units appear with the same height and the actual corrugation varies between 0.8 and 1.2 Å (Figure 4.9a). Occasionally, complete

cells are missing or groups of neighboring maxima merge into one continuous bright region. In the fourth layer it is surprising that the Moiré superstructure suddenly crosses over into a homogenous surface without apparent periodicity (Figure 4.9b). This contrast change often occurs in the middle of wide terraces, and is not correlated to surface step edges. Our finding suggests that the Moiré contrast does not exclusively arise from changes in the Zn/O binding positions on the Au(111), but gets enhanced by ad-species on the oxide surface. In the thin-film limit, these adsorbates occupy only distinct regions of the Moiré cell, amplifying the superstructure contrast. Only beyond the fourth layer, the adsorbates spread onto the surface and the superstructure pattern disappears. Remind that a Moiré contrast declining with film thickness would be expected if only the modulated Zn/O binding sites at the interface would govern the STM corrugation, in conflict with the experiment. These adsorbates on the ZnO(0001) surface play a role in the polarity cancelation, as it will showed later.

With increasing film thickness, the Moiré pattern disappears from the topographic images, although the surface retains a mean roughness of ~1 Å, as shown in Figure 4.8d and 4.9d. Our interpretation is that the very same ad-species that amplify the Moiré contrast on thin films give rise to the finite corrugation on thicker ones, only that they abandoned their long range order. The ZnO films, on the other hand, remain perfectly crystalline, as proven by the wide, triangular and hexagonal terraces seen in STM. The latter are delimited by straight step edges that follow the three equivalent $[110]$ orientations of the Au support. The predominant angle between adjacent steps amounts to 60°, while 120° angles only occur in the case of multiple steps.

Interpretation

We propose the following structure model for the ZnO/Au(111) system, which is based on our experimental results and the wealth of literature data on bulk ZnO. Two factors govern the oxide growth: *(i)* the polarity of the (0001) wurzite termination, and *(ii)* the lattice mismatch with the Au(111). The oxide adopts its own lattice parameter right from the beginning, so that interfacial lattice strain seems to be avoided. The stacking of two differently-sized hexagonal lattices gives rise to the observed Moiré pattern. Its dimension is best accounted for with an ZnO lattice expanded by +3% grown on top of non-reconstructed Au(111) [159, 161]. It is interesting to remark that systems with a stronger interface coupling, i.e. MgO/Mo(001) [162], often develop misfit-driven dislocation networks in order to compensate for the lattice strain. This is not observed for ZnO/Au(111), where relatively wide terraces are seen.

For the issue of polarity compensation, two balancing effects have to be considered [163, 164]. First, the oppositely charged ion planes (Zn^{2+} versus O^{2-}) tend to reduce their mutual distance in order to minimize the associated dipole moment [165]. This may converge to graphitic structures, as found for ZnO on Ag(111) [159], where the Zn and O ions reside in the same plane. Secondly, electron transfer between the oxide overlayer and the metal beneath generates an interface dipole that aligns opposite to the structural ZnO dipole and causes the Zn-O layer distance to increase again [162]. At the ZnO/Au interface, charges preferentially flow from the oxide into the electro-negative gold. This results in a stabilization of positively charged Zn^{2+} ions at the interface, while the O^{2-} ions are pushed outward [166]. The sum of both effects leads to a situation in

which the Zn^{2+}-O^{2-} layer distance is reduced, but not zero as on Ag(111), and the terminating plane is made of oxygen. The reduced step heights measured for the first ZnO layers (2.2 Å) with respect to thicker films (2.6 Å, Figure 4.8b) serves as indirect evidence for this scenario. In addition, the Zn^{2+}-O^{2-} layer distance is modulated by changes in the metal-oxide stacking across the Moiré cell (Figure 4.10a). At the places where both, Zn and O ions, occupy Au(111) hollow sites, the largest Zn-O interlayer distance is expected to take place. The reason is that the interface distance is small and the charge transfer into the gold is correspondingly big. Conversely, a nearly coplanar and dipole free situation may be adopted by ZnO units in the top domains of the Moiré cell, mimicking the situation of Ag(111) supports where charge-transfer effects are negligible (Figure 4.10a) [159].

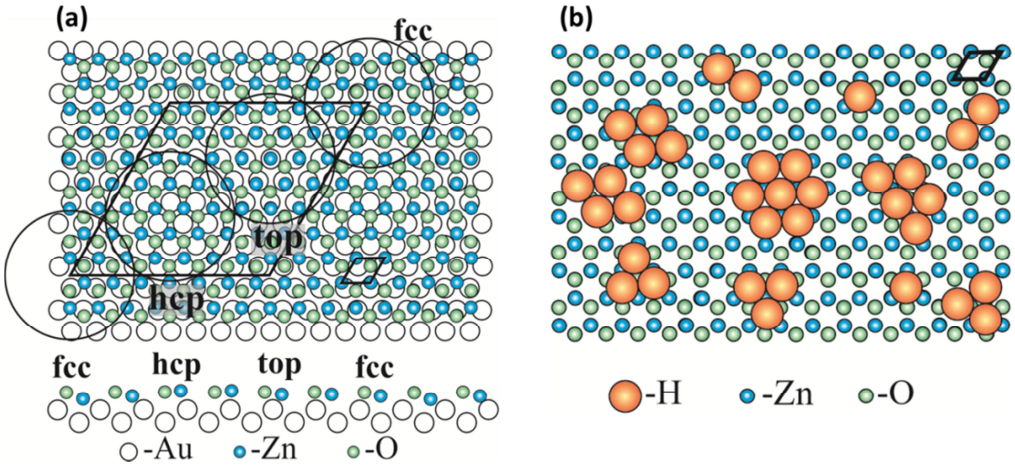

Figure 4.10. (a) Structure model of the ZnO / Au(111) Moiré cell, coming from the (7x7) super-cell sitting on top of the (8x8) Au surface. The three main binding configurations for Zn are also shown. Note the modulated Zn-O layer distance in the side-view, as discussed in the text. (b) Structure model of a thick film with the H adsorbates that compensate the polarity.

With increasing film thickness, the ZnO gradually develops a wurzite structure and a surface dipole builds up. For O-terminated films, being the expected stacking on electronegative gold, this dipole may be cancelled with positive excess charges, e.g. $Zn^{\delta+}$ or $H^{\delta+}$ ions, the density of which is given by the general compensation rule for polar materials: $\sigma_{surf} = \sigma_{bulk} \frac{d}{D}$ [167]. With d the bulk Zn-O layer distance (0.63 Å) and D the height of the unit cell (2.6 Å), a surface charge density of $\sigma_{surf} = +0.5|e|$ is required per unit cell to compensate for the polarity in the bulk. Due to the Moiré pattern, the polarity does not develop homogeneously with film thickness. The thickness-dependent dipole becomes critical first in the hollow domains of the Moiré cell, where a finite Zn-O layer distance is present already at the interface and the electrostatic dipole builds up most quickly. In those regions, compensating adsorbates are first attached to the surface and produce the decoration effect seen in the STM (Figure 4.9a). Above 4 ML thickness, dipole compensation is required throughout the surface and the decoration-effect, hence the Moiré pattern, vanishes from the measurements (Figure 4.9b). On thick O-terminated ZnO films, dipole compensation may be achieved either by ¼ ML of Zn^{2+} or ½ ML of H^{+} ions, as depicted in Figure 4.11. We expect our

films to be hydrogenated with the simple argument that any excess Zn would immediately oxidize at the O-rich conditions used for preparation. In addition, sufficient amounts of hydrogen are present in the rest gas of our chamber, facilitating surface hydrogenation. Hydrogen is known to form a (2×1) superstructure on ZnO(0001) [168]. Indeed, we are able to identify a faint row pattern on thick ZnO films, which is however not perfect but contains numerous defects, e.g. H-vacancies or H_2O molecules (Figure 4.9c).

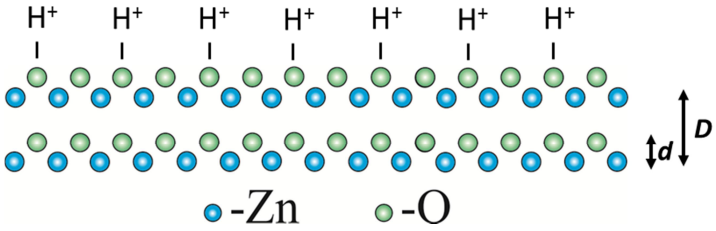

Figure 4.11. Charge density at the surface $\boldsymbol{\sigma_{surf} = +0.5\,|e|}$, which means one H^+ positive ion every two unit cells.

Additional scenarios for the dipole compensation on ZnO(0001) are proposed in the literature. For Zn-terminated ZnO, formation of a non-stoichiometric and oxygen-rich surface oxide was observed to contain a high density of nanometer-sized ad-islands and pits bordered by O-terminated step edges [169]. No equivalent surface reconstruction is revealed in our experiment and the ZnO terraces are flat down to the atomic scale. In contrast, the large propensity of O-terminated ZnO to develop a compensating hydrogen layer is well documented in the literature [170-172]. As dipole-compensation depends on the ZnO termination, which, in the case of thin films is governed by the nature of the metal support, different routes are expected to be active for ZnO on weakly and strongly electronegative substrates, e.g. on Ag(111) and Au(111).

4.3 Optical Properties of ZnO

The electronic structure of the oxide film and in particular the position of the band edges with respect to the Au Fermi level has been probed with STM conductance spectroscopy performed with lock-in technique and disabled feedback loop. The associated spectrum for a 15 ML thick ZnO film is depicted in Figure 4.12a. The band onsets show up as steep rises in the dI/dV signal, at -2.0 and +0.8 V for valence and conduction band, respectively. We measured a band gap value of 2.8 eV, which turns to be smaller than the bulk value of 3.4 eV. ZnO on Au(111) exhibits a strong n-type conductance behaviour. In other words, the Fermi level is much closer to the conduction than to the valence band of the oxide. This fact follows the behavior of bulk ZnO, which is known to be a strong n-type conductor. The origin of the high ZnO Fermi level is still under discussion. However, recent DFT calculations [173] and EELS measurements [174] indicated that H-ions in the ZnO lattice are responsible for the partial filling of the conduction band. Thi H-atoms dissolve in high quantities in the ZnO lattice, where they ionize and donate electrons into the ZnO conduction band, spontaneously.

In our case, the ZnO/Au(111) interface interaction contributes to the n-type conductance behaviour. As discussed before, ZnO looses electrons to the electronegative gold, generating a positive interface dipole that causes the vacuum energy and hence the oxide bands to shift down in energy. The role of interfacial charge-transfer on the band positions of thin oxide films has been discussed in detail in the literature, e.g. for CaO/Mo(001) films [175]. We have not detected gap states in the conductance curves, indicating that our ZnO films are reasonably stoichiometric and contain only small amounts of O and Zn defects.

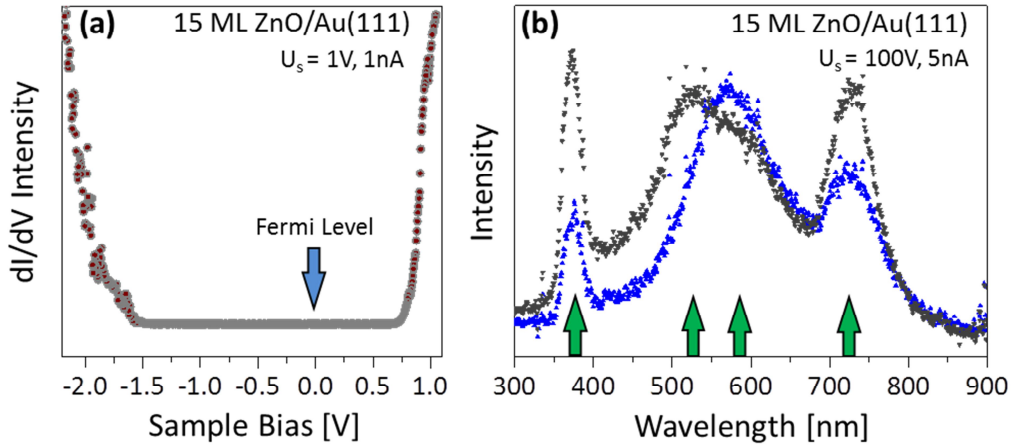

Figure 4.12. (a) STM conductance spectrum taken on a 15 ML thick ZnO film with 1.5 V setpoint bias. (b) STM luminescence measured on two similarly prepared ZnO films of 15 ML thickness. Arrows indicate the four main peaks. The first peak is due to the electron-hole recombination across the band gap. The other ones come from defects in the wurzite lattice, as discussed in the text.

Luminescence spectra of 15 ML thick ZnO/Au (111) films have been measured with the technique introduced in chapter 3 and are depicted in Figure 4.12b. The spectra were obtained via injection of 100 eV electrons (5 nA current) from the STM tip into a predefined sample region of approximately 100 nm diameter. The acquisition time has been restricted to 120 seconds in order to minimize electron-damage. Furthermore, the exposed surface region was changed after each spectral run. More moderate excitation conditions did not yield measurable photon fluxes from ZnO, although already 3.3 eV electrons were sufficient to generate intense plasmon-mediated light from bare Au(111), as shown in Figure 4.7 [176]. This difference shows that not an inadequate optical read-out but an intrinsically low emission yield renders the high-bias excitation of ZnO/Au films necessary. A typical ZnO emission spectrum is characterized by four emission lines, centered at 373 nm (3.3 eV), 535 nm (2.3 eV), 595 nm (2.1 eV) and 730 nm (1.7 eV), as it can be seen in Figure 4.12b. Whereas the high- and low-wavelength lines are sharp and distinct (FWHM: 90 / 180 meV, respectively), the two central lines are relatively broad (FWHM: 250 meV). The peak at 373 nm is readily assigned to the band-gap recombination of ZnO. Upon high-energy electron impact, hot electrons are excited into the conduction band, from where they relax to the band minimum situated at the Γ point. After that, they recombine radiatively with holes in the valence band, giving rise to the associated light emission [177]. It was not possible for us to resolve

the excitonic fine-structure of the band recombination. One reason for this was the low spectral resolution of our optical setup (150 lines/mm), whereas the other one was the experimental temperature that still enables exciton-phonon coupling. The excitonic fine-structure is therefore subjected to pronounced thermal broadening.

The remaining three emission peaks are only mentioned here, as their true origin is explained in the next section. They are intrinsic to ZnO without dopants and indicate the presence of defects in the oxide lattice. Whereas donor-type impurities, such as neutral O vacancies and Zn interstitials, induce filled gap states and allow for radiative recombination processes with holes in the valence band, acceptor-type defects, e.g. positively charged O defects, give rise to empty gap states and open up new recombination channels for hot electrons in the conduction band [26]. Comparing the results with literature data, we see that the intermediate peaks at 535 and 595 nm were already observed in ZnO crystals and nano-materials [178-181]. While the peak at 535 nm is likely assigned to Zn vacancies [31, 182, 183], the peak at 595 nm is of unknown origin. On the other hand, the 730 nm-emission band was found to emerge only after reducing the ZnO by vacuum annealing or electron bombardment. This indicates an emission channel mediated by O-vacancies [177, 184]. All peaks appear only in thick films and we consequently discarded a possible involvement of the ZnO/Au interface in the emission process. The nature of the different emission bands and their dependence on the ZnO preparation conditions with intrinsic and extrinsic defects is presented in detail in the following section.

4.3.1 Intrinsic Point Defects in ZnO and Their Influence on the Optical Activity

Intrinsic defects play an important role in the emission of light, introducing different peaks in the luminescence response of the material. The ambiguous role of lattice defects becomes particularly evident in the optical behavior of ZnO. Several strong transitions take place in the oxide due to the direct band gap. The most prominent one is the band-recombination peak at 3.3 eV. Additional peaks with sub-band-gap energy indicate the presence of defect-mediated emission channels but the origin of them is strongly discussed. In fact, many native ZnO defects with finite thermodynamic stability, such as Zn and O vacancies (V_{Zn}, V_O), interstitials (Zn_i, O_i) and anti-site defects, have been proposed as potential emission center. Furthermore, various impurity ions, in particular nitrogen, were linked to common ZnO emission bands. The difficulty to connect luminescence data to lattice defects arises from the strong dependence of defect concentrations on the different ZnO preparation conditions, in particular the Zn/O chemical potential. Moreover, the oxide defects have a large tendency to interact and to compensate each other. Given the variety of fabrication methods, it is therefore little surprising that different ZnO samples feature different defect landscapes and, as a consequence, different optical properties.

Typically, theoretical studies deliver the first information on the nature of ZnO defects. They can accurately predict ground-state properties (e.g. defect formation energies), but are less reliable when the situation involves excited states and their optical response [26, 185]. Hence, luminescence experiments on well-characterized ZnO samples are desirable to confirm the theoretical predictions.

In this chapter, we discuss such experiments, performed by growing crystalline ZnO films on Au(111) supports and by measuring local luminescence data with the STM. In order to elucidate the nature of defects, nearly stoichiometric films have been prepared as well as films with varying concentrations of ZnO point defects, as depicted in Figure 4.3 [186]. From differences in the optical response, conclusions are made on the interrelation of native ZnO defects and characteristic maxima in the photon-emission spectra.

The samples were prepared with the same procedure as descripted in section 4.2.1. In order to improve signal to noise ratio of the optical signal, we focused on rather thick films. After a cleaning step of the support, we started growing ZnO layers of 25 ML thickness by evaporating ZnO in O_2 atmosphere. Then, we performed an annealing step in $5x10^{-6}$ mbar O_2 pressure. Figure 4.13 shows a topographic image as well as STS- and cathodo-luminescence spectra corresponding to one of the first sets of samples used for the following experiments.

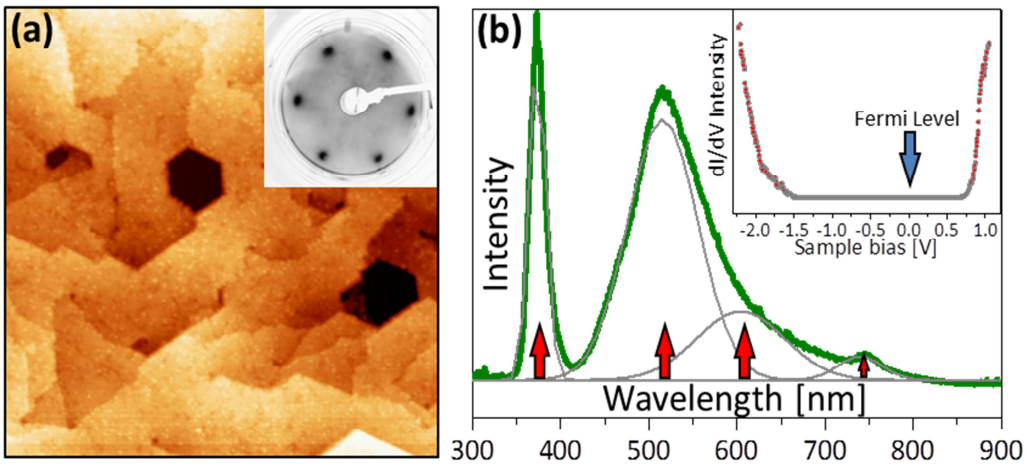

Figure 4.13. (a) Representative STM topographic image of a typical ZnO film of 25 ML thickness (1nA, 3.4 V, 220x220 nm^2) and its associated hexagonal LEED patter (inset). (b) Cathodoluminescence spectrum shows all the typical ZnO peaks. Emission maxima were determined via Gaussian deconvolution. (inset) STS spectra shows band gap similar to the bulk.

We aim to find a correlation between lattice defects and luminescence peaks. For this reason, we intend to create lattice defects in defined quantities, as long as our experimental set up allows it. According to the formation energy of defects in O-rich conditions shown in Figure 4.4, we want to address three types of vacancies: oxygen vacancies, oxygen interstitials and zinc vacancies. For the creation of oxygen vacancies, we propose thermal, optical and chemical methods. The removal of oxygen atoms by means of a thermal treatment from a glowing tungsten filament, i.e. with electron bombardment, has the disadvantage of promoting the formation of zinc vacancies as well without being controlled [187]. On the other hand, the thermal desorption of oxygen atoms by optical means has already been studied in oxide materials [188, 189]. As a result of a first photonic irradiation, a surface corner in the lattice is excited and

then undergoes non-radiative relaxation into the lowest triplet state. The corner O-atom can be exited again into a higher exited state by a second photon of the same energy, leading to the desorption of the O-atom. In the chemical case, hydrogen interacts with lattice oxygen, leading to the formation of water. Later, this water leaves the surface at elevated temperature, leaving an oxygen vacancy [190, 191].

Luminescence from Reduced ZnO Thin Films

In order to insert O-vacancies into the lattice, we have prepared ZnO films at reducing conditions by the methods explained before. The ZnO cathodoluminescence corresponding to different annealing temperatures is shown in Figure 4.14a [114]. The intensity of the 730 nm peak becomes bigger by a factor of five, corresponding to the main change in the light emission spectrum, while the other peaks do not suffer any significant change. As explained in the last section, annealing in vacuum also influences the amount of Zn defects. Thus, the optical approach has been chosen as the next step to reduce the oxide. Using the third harmonics of a Nd:Yag laser, we exposed the sample in situ to UV photons of 3.5 eV energy. The fluence of the laser was varied between 0.5-1.5 mJ/cm^2. These values are considered sufficient small to suppress thermal effects. It is important to note that also the 730 nm peak gained intensity during the experiment.

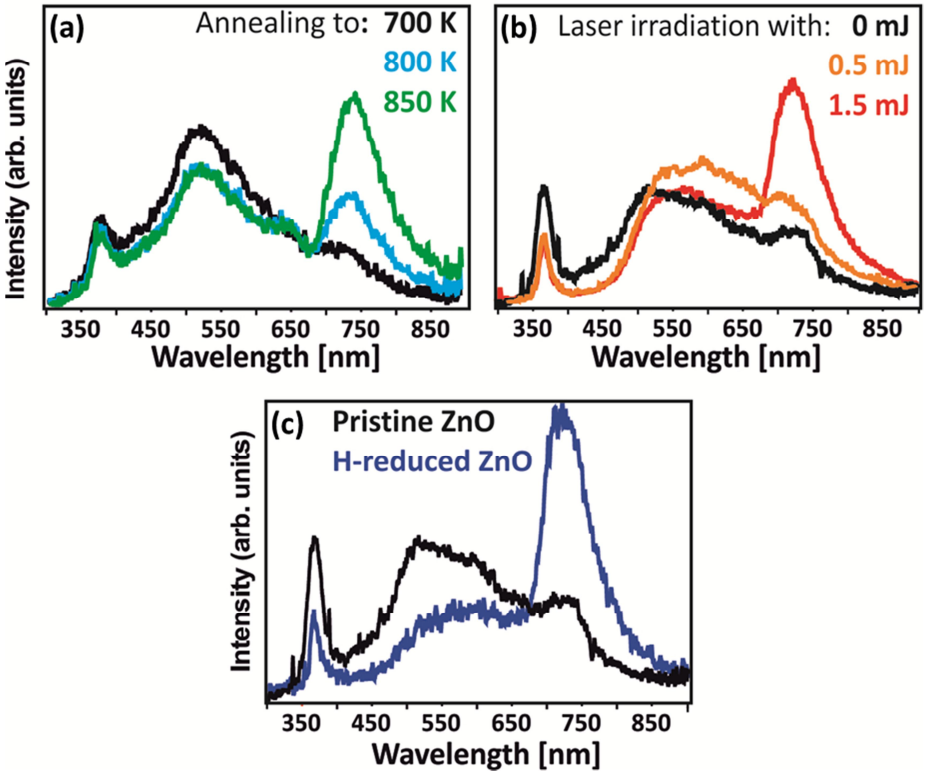

Figure 4.14. Evolution of ZnO cathodoluminescence spectra of pristine and reduced films. (a) Thermal treatment in 2×10^{-5} mbar O_2 at 700 K (black) and in vacuum at 800 K (light blue) and 850 K (green). (b) Reduction with 3.5 eV photons through laser irradiation: pristine film (black), after exposure to 0.5 (orange) and 1.5 mJ laser flux (red). (c) Chemical reduction: pristine film (black) and film grown in atomic hydrogen (blue).

On the other hand, other lines remained constant, as seen in Figure 4.14b. As a final step, chemical reduction was achieved by exposing the films to atomic hydrogen during growth. After that, an annealing step at 600 K was performed. Principally, the 730 nm emission arises again. This effect shows that all reduction-methods affect the same optical transition that is likely associated to V_O defects in the lattice, as shown in Figure 4.14c [114].

The second part of these experiments involved producing oxygen interstitials, as they are considered as another type of defect. They were intentionally created via oxygen ion implantation into the as-grown film at room temperature. After this step, we tried to recover the lattice quality by annealing the sample at 600 K in $2x10^{-5}$ mbar of oxygen. Luminescence spectra of those samples did not show the 730 nm emission peak that was always observed in the reduced oxide. However, the 595 nm peak appeared with higher intensity, even though this intensity is still smaller as the 730 nm emission observed after reduction (Fig. 4.15).

The last experiment aimed to address the zinc defects. However, it is not an easy task to change their amount, as they play an important role in balancing the charge neutrality despite the excess electrons in n-type ZnO [26]. Theoretically, only if all preparation steps are performed at finite zinc chemical potential, the concentration of zinc vacancies could be reduced. This implies a non-zero Zn partial pressure in the chamber, which is a challenging task in an UHV experiment. In order to overcome this problem, Zn-rich films were prepared by exposing the Au(111) support simultaneously to ZnO vapor and metallic Zn from a second source. After deposition, an annealing step at 600 K in $5x10^{-8}$ mbar O_2 was done. In the resulting light emission spectrum, the 535 nm peak experienced a large reduction. In contrast, the other peaks were less altered due to the preparation in Zn excess, as shown in Figure 4.15b. This fact gives a hint that zinc related defects may affect the luminescence in the green spectral region. Hence, a correlation between ZnO emission spectra and native defects in the wurtzite lattice could be established. The following list aims to describe this correlation for each native defect in detail.

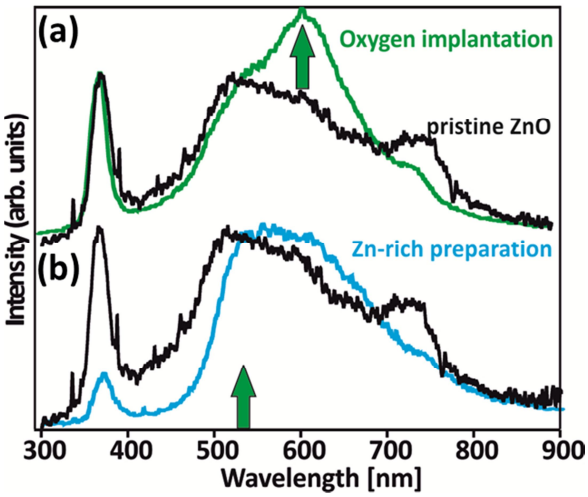

Figure 4.15. Luminescence spectra of ZnO films with different concentration of defects: pristine ZnO (black) and films grown in presence of atomic oxygen (green) and Zn-excess (blue).

Oxygen Vacancies

It is predicted by theory that V_O defects are thermodynamically less stable than Zn vacancies in n-type ZnO, as it can be seen in Figure 4.4 (right, O-rich conditions) [26]. As a consequence, all optical transitions that involve oxygen defects should be weak in well-prepared films. This requirement is only fulfilled by the 730 nm peak (Figure 4.14, black curves). Furthermore, the intensity of this peak turns bigger when reducing the oxide by thermal, optical or chemical methods. These last processes introduce V_O defects into the lattice (Figure 4.15), as already discussed in section 4.1.4.

Following DFT calculations, these defects produce gap states that will be doubly occupied in our films due to their high Fermi level and the presence of the Au(111) electron reservoir beneath [26]. Two scenarios may connect the peak in the electron-stimulated photon emission with O-vacancies:

(i) formation of a hole in the ZnO valence band followed by radiative decay of electrons from the V_O gap states, or

(ii) hole formation in the V_O gap states and recombination with conduction-band electrons.

In both cases, the V_O-defect level needs to be located in the middle of the band gap in order to produce an emission peak at 730 nm. However, only the first of the two mechanisms proposed above has been reproduced by DFT calculations [26, 185]. The concept, that a hole is captured by doubly charged V_O defects is also supported by luminescence data obtained on ZnO samples bombarded with MeV electrons [184, 192]. Here, a pronounced 730 nm peak was found to develop as the electrons removed oxygen from the lattice. According to this result, the peak corresponding to 730 nm is assigned to O vacancies.

Zinc Vacancies

Due to the difficulties in controlling the concentration of Zn vacancies from the experimental point of view, the role of Zn vacancies in luminescence spectra is rather hard to evaluate. However, there may be a correlation between Zn defects and the 535 nm emission peak for the following reasons.

First, the 535 nm peak has the highest intensity of all sub-gap maxima and cannot be completely eliminated using our preparation approach. This is in agreement with the low formation energy of V_{Zn} in theoretical approaches such as seen in Fig. 4.4, being rationalized by the necesity to insert this defect to reach charge balance with the excess electrons in the conduction band of n-type ZnO [26]. Only in the case that the Fermi level is close to the valence band, oxygen defects become energetically favorable. But this situation could not be reached in our experiments, as it is demonstrated in section 4.3.2 of this chapter.

Second, the 535 nm emission seems to decrease in samples having an excess of Zn, being produced by inserting metallic Zn to the preparation. This effect clearly indicates a partial annihilation of the V_{Zn} defects, as shown in Figure 4.15b. Nevertheless, we cannot reduce the number of Zn vacancies to zero because new defects develop spontaneously in the lattice during the annealing process of the film. In spite of the last

fact, our arguments still support a correlation between V_{Zn} defects and the 535 nm emission peak.

Considering an energy scheme, the Zn vacancies introduce acceptor-type gap states close to the valence band, as the zinc cations in the lattice have an initial charge of +2. These gap states are filled with electrons at the high Fermi level of the films (V_{Zn}^{-2} centers) [26]. Whenever holes are generated in the respective states, the defects turn optically active via two ways: *(i)* ionization by the incoming electrons (direct process), or *(ii)* capturing a hole from the valence band (indirect process). In both cases, the excited V_{Zn}^{-} center can recombine with a hot electron in the conduction band, and generates the 535 nm emission peak, as illustrated in Figure 4.16. The wavelength difference to the V_O emission at 730nm was also analyzed. The position of the V_{Zn} gap state was ~0.6 eV closer to the valence band than to the V_O state. DFT calculations found an energy difference of 0.9 eV between V_{Zn}^{2-}/V_{Zn}^{-} and the V_O^{0}/V_O^{+} transitions step, in agreement with our proposed mechanism. However, this last value ignores relaxation effects in the system during the optical transitions [183] that may contribute to the difference of the values. The 535 nm peak being assigned to the Zn vacancies is in agreement with earlier studies on ZnO single crystals and powders [29, 31], even though there has been no clear assignment so far.

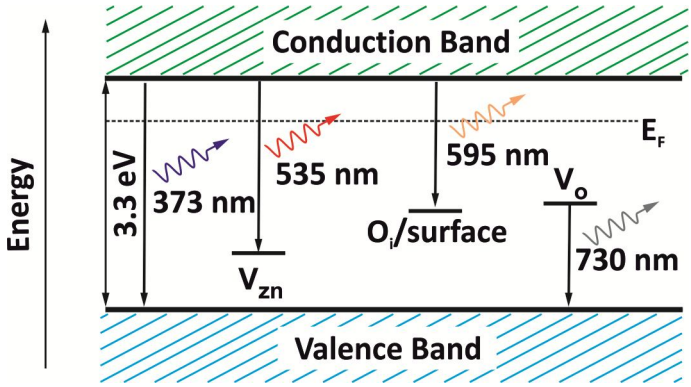

Figure 4.16. Energy scheme with the approximate positions of the defects inside the band gap

Frenkel Defects

The interpretation of the 595 nm peak in the ZnO luminescence is still open. This peak is already observable in as-grown films (Figure 4.13b). This suggests a low formation energy of the associated defect, as it spontaneously develops at our grown conditions. Taking into consideration the DFT stability diagrams for n-dopend ZnO (Figure 4.4) [26, 185], it is clearly seen that oxygen interstitials are the most stable defects, after the Zinc vacancies at the O-rich conditions used in our work. The defects appear in two configurations: *(i)* as an additional O^{2-} ion in an octahedral lattice site or *(ii)* as quasi molecular species occupying the original anion position. Whereas the latter possibility is optically inactive, the former induces an acceptor state in the lower part of the gap that gets filled up with electrons in our films. A radiative recombination channel opens up for conduction-band electrons, providing that ionization via electrons from the tip takes place. The underlying scenario is similar to the proposed one for Zinc vacancies.

Taking the emission peak at 595 nm as a fingerprint for this transition, the energy position of the ionized O_i state may be estimated to be at 1.2 eV above the valence-band edge, as depicted in Figure 4.16. This value is comparable to the calculated transition levels for single and double charged O_i defects at 0.7 eV and 1.5 eV, respectively [26]. Thus, the 595 nm peak is potentially related to O-interstitials in the lattice. Moreover, it turns to be most sensitive to the growth of ZnO in the presence of atomic oxygen. In conclusion, this type of oxygen interstitials is considered to play an important role for the 595 nm peak, as shown in Figure Figure 4.15a.

The 595 nm emission is often seen also in ZnO nanostructures, such as rods, tubes, and coils [180, 193]. This observation opens an alternative path for the interpretation of the peak, being related to the recombination of ZnO excitons at different surface sites. Two effects can reduce the oxide gap at the surface: (i) a reduced Madelung potential or (ii) specific surface states [194]. The effect of the reduced Madelung potential arises from the lower number of nearest neighbor ions at the surface [146]. Surface contributions are naturally strong in thin films and, as a result, the corresponding peak must be visible even though no comparable emission is found in bulk crystals.

To sum up, out of the common band recombination peak, also several defect-related emission lines are found in STM luminescence spectra of flat ZnO films prepared on Au(111) single crystals. In order to identify possible candidates for the lattice defects, the preparation conditions were altered in a systematic way. The experiments in this section made evident how thin-film techniques in combination with optical tools can be used for the understanding of the defect landscape in oxide materials. The intrinsic defects in this type of materials are of fundamental importance for their physical and chemical properties.

However, not only intrinsic defects are important for determining the optical properties of oxides. Extrinsic impurities drastically change the electrical as well as the optical features of oxides as well, as described in section 4.1.5. In the following section, the behaviour of ZnO in presence of impurities in the lattice will be presented.

4.3.2 Nitrogen-Doped ZnO Films

Our studies of ZnO thin films presented in this thesis revealed a n-type conductivity of the material. This was already seen in Figures 4.12 and 4.13. This type of conductivity is derived from the position of the Fermi level, which is situated closer to the positive than the negative onset of the ZnO bulk bands. A close position in the vicinity of the conduction band indicates a n-type character of ZnO. However, the presence of native point defects cannot explain the unintentional n-type conductivity of ZnO and possible impurities that act as shallow donors becomes relevant for the interpretation. In order to control the n-type conductivity in ZnO, we aim to investigate these impurities that are responsible for making n-type ZnO a stable configuration.

Similar to the preparation of ZnO samples in section 4.2.1, we used for our experiments films of 25 ML thickness. They were prepared by evaporating ZnO pellets in $2x10^{-5}$ mbar of oxygen onto an Au(111) single crystal at room temperature. The crystallinity of the film was achieved via an annealing step, also done in oxygen atmosphere. The sharp, hexagonal (1x1) LEED pattern indicated the crystallinity of the

ZnO and the $(000\bar{1})$ termination. STM images confirmed the crystalline nature of the sample, which exhibited wide terraces delimited by straight steps along the high symmetry directions of the wurtzite lattice, as depicted in Figure 4.17a. The surface was homogenously covered with protutions that had a size of a few Å. They were assigned to individual hydroxyl (-OH) groups. As described in section 4.2.2, the polarity of the oxygen-terminated ZnO needs to be removed, which is typically achieved by hydroxylation [113].

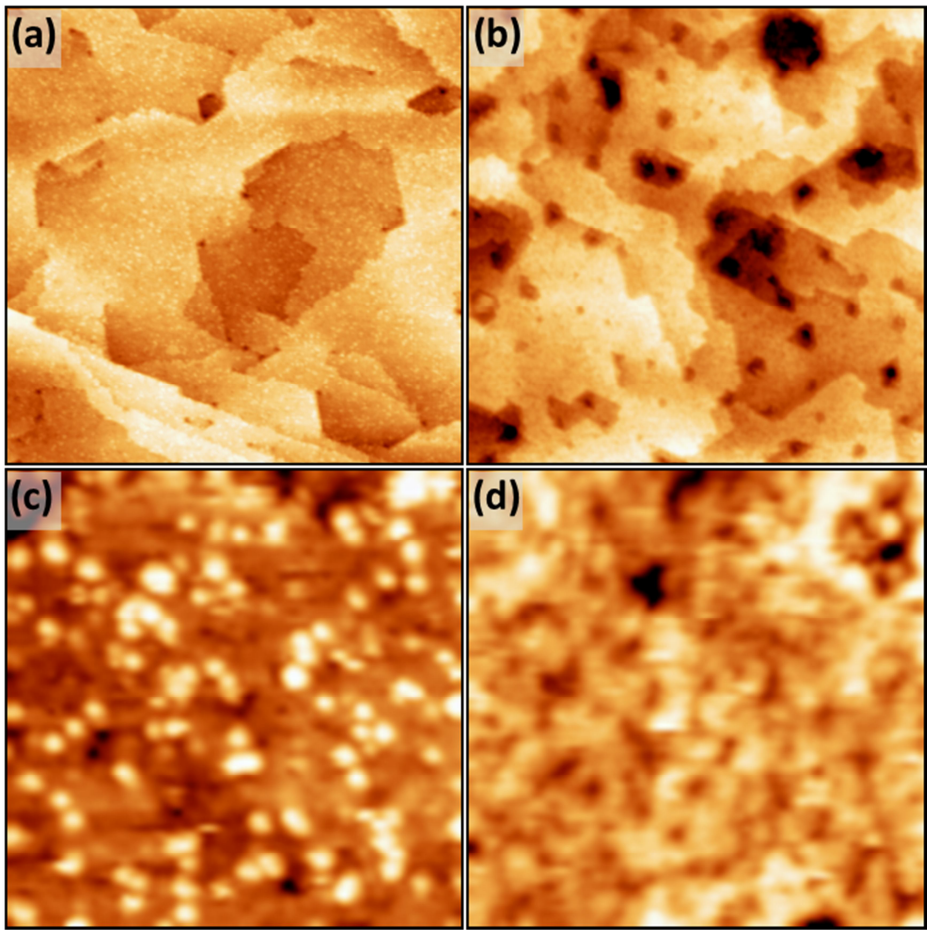

Figure 4.17. STM topographic images of (a) pristine and (b) nitrogen-doped ZnO films of 25 ML thickness grown on Au(111). (1 nA, 3.8 V, 200×200 nm^2). Nano-sized protutions that are related to hydroxyl groups in oxygen terminated ZnO are shown in (c) The surface irregularities in (d) result from a mixture of OH-groups and N-related surface defects (25×25 nm^2).

The process of doping was accomplished by adding atomic nitrogen, which was produced by an ion gun and mixed with the oxygen ambience used for film growth. In order to fabricate heavily and weakly doped films, the nitrogen flux has been varied between $5x10^{15}$ and $1x10^{14}$ ions/s, respectively. The films were crystallized again by gently annealing of the sample at 700 K in a gas mixture, containing $1x10^{-5}$ mbar N_2 and $1x10^{-5}$ mbar of O_2. We note that N_2 could not be incorporated directly into the film, as the molecular species tended to leave the sample in the subsequent annealing steps. Films produced by molecular nitrogen therefore reproduced the properties of non-doped samples.

Analysis of n-doped ZnO

The STM topographic images of two different 25-ML thick ZnO films are presented in Figure 4.17. The main difference lays on the preparation conditions. Whereas in Figure 4.17a, the sample corresponds to bare ZnO, in Figure 4.17b, the sample was prepared by adding atomic nitrogen to the growth atmosphere, aiming to achieve doping conditions. The overall film morphology was found to be similar in both cases, apart from the fact that large growth pits appeared in the doped films. These holes are caused by nitrogen-induced defects that develop during N exposure and coalesce into large pits in the subsequent annealing step. Nitrogen incorporation also leaves morphological fingerprints in the STM images at the near-atomic scale. In the case of pristine ZnO, the surface is homogeneously covered with Å-sized protutions typical for hydroxyl groups. In contrast, the doped oxide features faint depressions on the surface that grow in number at higher nitrogen exposure, as seen in Figure 4.17d [195, 196]. Due to the finite spatial resolution of our PSTM equipment, it was not possible to distinguish whether those minima represent the dopants or emerge as secondary defects during the nitrogen treatment. The electron diffraction patterns of both, pristine and doped films were analyzed and turned out to be indistinguishable from each other. Therefore, no evidence for the formation of nitride or oxonitride phases was revealed in our study.

In contrast to the morphology, the ZnO electronic structure, as probed with STM conductance spectroscopy, shows big differences between pristine and doped films. Normally, spectra of bare ZnO show a wide band gap, which reaches from the valence-band onset at around -2.0 to the conduction band situated at +0.75 V, as shown in Figure 4.18. Hence, the total gap size of 2.75 eV is slightly smaller than the one in the bulk material. The n-type character of the films is demonstrated again by the proximity of the conduction band to the Fermi level. When the samples were doped with nitrogen, the onset of the valence states undergoes a pronounced upshift towards the Fermi energy, causing the band gap to become smaller and also more symmetric. At high doping levels, the band gap collapses to a value of 1.0 eV, indicating a massive inducting of new electronic states in the band gap due to the nitrogen impurities.

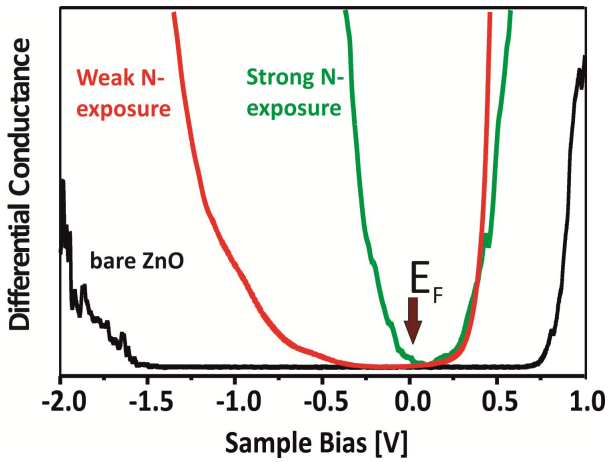

Figure 4.18. Differential conductance spectra taken on bare and nitrogen-doped ZnO films. The band gap gets strongly reduced upon increasing nitrogen exposure.

In order to obtain additional information on the behaviour of pristine and nitrogen-doped ZnO, the optical response was checked by employing STM-assisted luminescence spectroscopy. As discussed before at the beginning of section 4.3, the spectra of pristine films show four major emission bands that slightly vary in their relative intensity from sample to sample. The prominent peak at 373 nm (3.3 eV) was assigned to the recombination of excitonic ZnO modes, while intrinsic defects in the oxide lattice were found to be responsible for the high-wavelength bands.

Surprisingly, the same emission bands that occur for pristine ZnO are detected for the nitrogen-doped films at almost identical positions (Figure 4.19b). This fact indicates that nitrogen-doping does not create new recombination channels for hot electrons or holes generated by the STM tip. However, the spectral intensity of the existing peaks is modulated by the nitrogen-ions in the lattice. This effect becomes clear after analysing the intensities of the peaks in Figure 4.19b. The band recombination peak at 373 nm loses intensity, probably due to an increasing disorder in the doped samples [197]. On the other hand, the 730 nm-peak gets more intense when increasing the doping level. In the case of strongly doped films, the peak still reaches ten times the intensity of the band-recombination peak, in sharp contrast to pristine samples, as seen from Figure 4.19a. Moreover, the 730 nm-band could be further enhanced by vacuum annealing of the doped samples at 700-850 K. This behaviour is similar to the annealing of the non-doped films. The 535 nm-line assigned to Zn vacancies remains without changes upon doping. Apparently, the overall emission behaviour of doped ZnO matches the one of the non-doped but highly reduced oxide films. This fact suggests that nitrogen plays only an indirect role for the emission properties. As a first interpretation, nitrogen incorporation possibly promotes the formation of oxygen vacancies in the wurtzite lattice, which in turn produces the red luminescence at 730 nm. This idea will be supported in the following paragraph.

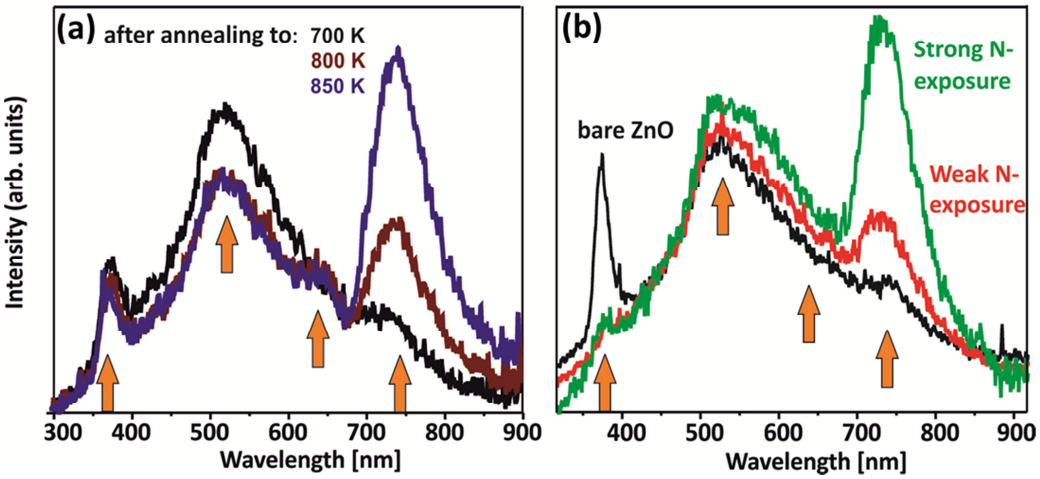

Figure 4.19. (a) STM luminescence spectra of bare ZnO prepared via a post growth annealing in oxygen at 700 K and vacuum annealing at substantially higher temperature to stimulate thermal reduction. (b) Similar spectra of doped ZnO films grown at different nitrogen exposure and post-annealed at 700 K. Excitation conditions are 5nA and 150 V for all spectra. The four main peaks are marked with arrows.

In previous works, nitrogen insertion into the ZnO lattice has always been connected with the appearance of a 730 nm luminescence peak [157]. According to recent DFT

calculations, the nitrogen-impurity ions produce a deep acceptor level in the ZnO band gap. This acceptor level enables radiative recombination of hot electrons from the conduction band. According to calculations that considered structural relaxations, the transition is associated to an energy of 1.7 eV, which is in good agreement with a 730 nm emission response. However, in this work we challenge this interpretation. As it can be seen in Figure 4.19a, the 730 nm-peak also occurs in photoluminescence spectra of ZnO films that were never brought into contact with atomic or molecular nitrogen. Considering the conditions of the experiments, this is a highly reliable statement, as the samples were prepared in an ultrahigh vacuum environment of $2x10^{-10}$ mbar, using an oxygen source of 99.999% purity. Also the ZnO pellets were free of nitrogen, as evaluated from the peak-14 intensity in mass spectrometry. Clearly, the 730 nm-emission peak could be reproduced even in those nitrogen-free films, for instance due to annealing in vacuum, exposure to ultraviolet photons or treatment with atomic hydrogen, as it was demonstrated in the other sections of this thesis [196]. Whereas these procedures are unable to change the nitrogen content in the samples, they all affect the abundance of O vacancies in the lattice. Hence, our experiments strongly indicate that the red luminescence is related to oxygen vacancies rather than to nitrogen-related defects.

Nevertheless, the 730 nm-emission also appears when atomic nitrogen is added to the ZnO growth atmosphere, as depicted in Figure 4.19b. A plausible explanation might be the facilitated formation of oxygen vacancies in presence of nitrogen impurities. This effect would be compatible with the valence difference between oxygen and nitrogen. N-atoms that are found on substitutional oxygen sites lack one valence electron to fill their 2p shell in the wurtzite lattice. Consequently, a localized hole-state develops in the band gap, transforming the N-ion into a deep acceptor. This energetically unfavourable situation can be removed if a compensating defect forms in the oxide lattice, providing that it supplies the missing electron. The ideal defect would be an anion vacancy (V_O), as described by the following expression in Kröger-Vink notation [198]:

$$2\ N_O^{\times} + O_{latt}^{\times} \rightarrow 2\ N_O^{-} + V_O^{2+} + \tfrac{1}{2}\ O_2\,(\text{desorb}). \tag{4.10}$$

In this case, the two extra electrons generated by the release of a neutral ½ O_2 molecule are used to satisfy the valence requirements of two nitrogen ions in the ZnO lattice. At this point, it is important to remark that the proposed ionic picture oversimplifies the situation, as bonds in the wurtzite lattice have a substantial covalent contribution.

In fact, the spontaneous development of compensating defects in the presence of charged impurities is a common phenomenon in oxide systems. For example, the substitution of bivalent Mg with monovalent Li ions in materials with rocksalt structure triggers the formation of oxygen vacancies as well, according to the following equation [199]:

$$2\ Li_{Mg}^{-} + 2\ O_{latt}^{+} \rightarrow 2\ Li_{Mg}^{-} + V_O^{2+} + O_{latt}^{\times} + \tfrac{1}{2}\ O_2\,(\text{desorb}). \tag{4.11}$$

The situation described in equation (4.10) connects the appearance of a 730 nm-emission peak with the formation of oxygen defects in nitrogen-doped ZnO. It also explains the puzzling result of a strong 730 nm-line in apparently nitrogen-free ZnO

films. In that case, the oxygen vacancies are caused by other processes, e.g. the thermal or photochemical removal of lattice oxygen.

Finally, potential strategies to produce either p-conductive ZnO or low band-gap materials for optoelectronic and photovoltaic applications are discussed. As it was appreciated in the conductance measurements, a gradual decrease of the band gap takes place upon nitrogen incorporation. This effect may be explained by the induction of new electronic states into the oxide gap, originating from both nitrogen substitutes and compensating oxygen defects. At high doping level, the reduced gap size allows for electron transport even at negative and low positive bias, an effect that is not observed for stoichiometric ZnO films. Hence, band-gap reduction via excessive nitrogen doping seems to be feasible. On the other hand, a switch between n- and p-type conductivity has never been observed in our experiments, as the Fermi level was found to remain constant with respect to the conduction band and only new states emerged in the lower part of the gap. A genuine p-type conductivity cannot be achieved by this trend. We therefore doubt that nitrogen doping represents a promising approach to achieve hole conductivity in ZnO [156, 200].

In this part of the thesis, optical transitions of ZnO thin films were studied with STM luminescence spectroscopy. Intrinsic as well as extrinsic defects were created. In all cases, the optical spectra showed a peak at 373 nm, which has been related to the band gap transition and demonstrated the crystalline character of the films, due to its similarity to bulk ZnO. Zinc vacancies were responsible for a pronounced 535 nm emission. The interpretation of the 595 nm emission peak was ambivalent, as two explanations may be possible for this effect: either oxygen interstitials or surface states. Last, the 730 nm peak was analysed in terms of a possible role of dopants in the ZnO lattice. However, the peak was better explained by optical transitions due to oxygen vacancies in the wurtzite lattice. Hole conduction has not been observed in our samples and we doubt that it can be achieved solely via nitrogen doping of ZnO.

4.4 Modification of Optical Properties of ZnO via Ag Deposition

4.4.1 Metal Particles on Oxides

The aim of this section is to describe the behaviour of different metal particles grown on top of ZnO thin films in order to modify the optical activity. First, we provide a brief introduction to metal particles on oxides, before describing their growth behaviour on ZnO.

During the past decades, the structure and properties of small metal particles have attracted a lot of attention in the field of fundamental research. Due to their exceptional physical and chemical properties, the intermediate state of matter between simple atoms in the gas phase and the solid state has been intensively investigated. In the case of free unsupported clusters, the properties are essentially determined by the aggregate size. In constrast, for deposited systems, the interaction with the substrate can play an important role as well, in this way, modifying, changing and strengthening certain features.

Heterogeneous catalysis is one of the areas in which deposited metal particles are employed to a large extent. In this field, a catalytically active component, such as a transition metal, is dispersed over a suitable support, usually an oxide like alumina, silica or zinc oxide. This is done in order to achieve the highest possible surface area of the active phase. In addition, due to the high degree of dispersion, particle-size effects can influence the catalytic behaviour in a dramatic way. These effects originate, for example, from specific structural or electronic features. The improvement of the catalytic activity and selectivity of a supported catalyst have always been the central question in catalytic research [201, 202].

This part of the thesis aims to study the structure and morphology of metal particles grown on thin oxides films by vapour deposition. First, we would like to address the processes taking place on the surface when a metal vapour is precipitated onto an oxide support [203, 204]. The adsorption of the incoming metal atoms on the surface is the first important step. In order to stick, the atoms have to get thermally accommodated to the surface. Otherwise, they would be elastically scattered. Although we have no direct experimental evidence, we assume in a first approximation that the probability of the incoming atoms to stick is close to one. On the other hand, this fact does not mean that every adatom will be trapped on the surface. Desorption effects, such as re-evaporation, may lead to a net sticking coefficient smaller than one. The effect is considered as incomplete condensation. Thus, if the substrate temperature is higher, this effect is more important. Nevertheless, the sticking probability is still near to one for many transition metals on oxides at room temperature, as it has been demonstrated in the literature [205, 206]. The following expression determines the diffusion coefficient of the atoms across the surface, once they have been adsorbed [202]:

$$D = \frac{1}{4}(v_0 a^2)\exp\left(-\frac{\varepsilon_{Diff}}{k_B T}\right), \tag{4.12}$$

where ε_{Diff} represents the activation energy for diffusion, usually scaling with the adsorption energy, v_0 is the prefactor, a is the distance between two adjacent adsorption sites, T is the temperature and k_B is the Boltzmann constant. The average travel time is related to the travel distance l and the diffusion coefficient, as follows:

$$\tau = l^2/4D \ . \tag{4.13}$$

A process called *heterogeneous nucleation* takes place in the case that defects are present on the surface, as the adatoms may be trapped at these sites forming nuclei for subsequent growth processes. The other borderline case is *homogeneous nucleation*, where a stable nucleus is generated by aggregation of several adatoms on regular sites. The *critical cluster size* is defined by the minimum number of atoms that a single diffusing atom must find for the homogeneous nucleation. In case of addition of further adatoms, these nuclei will then grow, while, on the contrary, islands up to that size can dissolve again.

In the case of homogeneous nucleation, the diffusion coeffiecient and the vapor flux F define the saturation density of nuclei N. Its expression is defined for a critical cluster size of one atom as follows:

$$N \sim (F/D)^{1/3} \ . \tag{4.14}$$

Growth processes take place once the saturation density of particles has been reached. In this case, no further nuclei form and all diffusing adatoms are captured by existing islands, providing that they have attained a certain size. The dimension of the growth mode (2D or 3D), which is expected for a given combination of a metal and an oxide, is defined by thermodynamics. The surface free energies of the metal, γ_{Metal}, and the oxide, γ_{Oxide}, and the free energy of the metal-oxide interface, $\gamma_{Interface}$, define the growth behaviour [204, 207]. If

$$\gamma_{Interface} + \gamma_{metal} \leq \gamma_{Oxide} \ , \tag{4.15}$$

which means that free energy is gained by formation of the oxide-metal and the metal-vacuum interface, the metal wets the oxide at equilibrium corresponding to a layer-by-layer growth mode, also called *Frank-van-der-Merwe* growth mode, as shown in Figure 4.20. On the other hand, when

$$\gamma_{Interface} + \gamma_{metal} > \gamma_{Oxide} \ , \tag{4.16}$$

wetting turns out to be thermodynamically forbidden and the metal is expected to form thick 3D aggregates, which is known as *Volmer-Weber* growth mode. As the surface free energies of metals (especially of transition metals) are normally large than those of oxides [208], equation (4.15) means that a layer-by-layer growth mode should be an exception and that the growth of 3D particles is very likely to happen. This has already been observed in many deposition studies of metals on oxides [208-210]. Also a third growth mode is possible, which is known as the *Stranski-Krastanov* mode, see Figure 4.20. In this case, three dimensional metal particles grow after formation of a closed atomic monolayer on the surface. However, the Volmer-Weber mode is most frequently observed due to the bigger surface energy of metals in comparison with those of oxides.

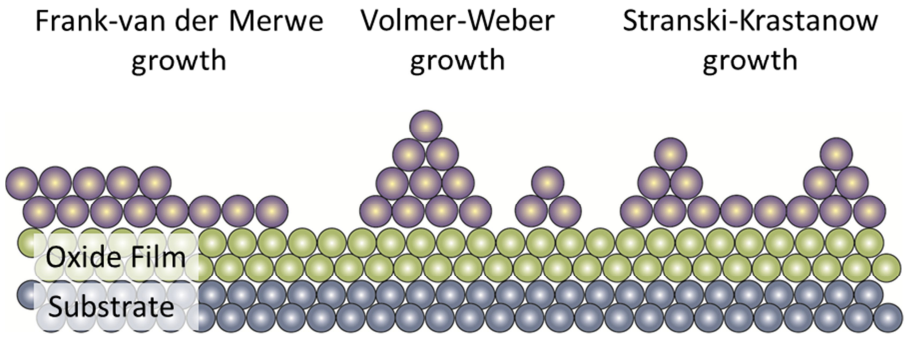

Figure 4.20. Schematics of the three growth models of metal particles on oxides films

In addition, the equilibrium shape of the aggregates can also be predicted. As shown in Figure 4.21 (left), the schematic corresponds to a *Wulff polyhedron* truncated at the interface in accordance with the following equation [211]:

$$\Delta h/h_i = E_{Adh}/\gamma_{Metal(i)}, \tag{4.17}$$

where $\gamma_{Mteal(i)}$ is the surface free energy of the corresponding crystal face i and E_{Adh} is the adhesion energy, given by [212]:

$$E_{Adh} = \gamma_{Metal(i)} + \gamma_{Oxide} - \gamma_{Interface} \ . \quad (4.18)$$

From equation (4.17), it becomes evident that the particles become flatter, when the adhesion energy increases. The adhesion energy is in turn dependent on the strength of the metal-oxide interaction, as it can be deduced from eq. (4.18). If this interaction increases, $\gamma_{Interface}$ will decrease, which results in larger values of E_{Adh}. This can happen, for example, due to partial oxidation. Therefore, it is not surprising that adhesion energies have been found to roughly correlate with the negative enthalpies of formation of the oxide of the metal (per mole of oxygen) [210, 213].

The model of the Wulff polyhedron is only valid in conditions of thermodynamic equilibrium. Furthermore, the facet with the lowest free energy often corresponds to the top of the cluster.

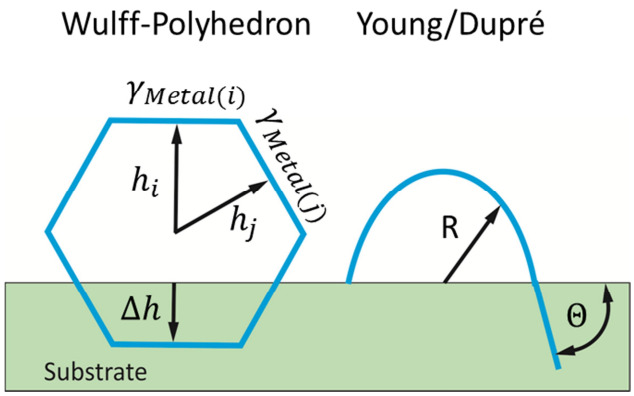

Figure 4.21. Geometric models for estimation of the shape of metal particles on oxide surfaces

On the other hand, the *Young-Dupré* model considers a contact angle Θ between a fluid metal particle and its supporting oxide substrate. The following formula describes the equilibrium shape for metals clusters (Figure 4.21, right) [214]:

$$\cos\Theta = (E_{Adh}/\sigma_M) - 1 \ . \quad (4.19)$$

The free energy of the surface $\gamma_{Metal(i)}$ of the different facets of a metal is replaced in this model by the surface energy of the fluid aggregate σ_M. In this context, high adhesion energies lead to small contact angles and therefore promote a two dimensional growth of the particles on the oxide. Upon increase of the contact angle between metal and substrate, the clusters grow with larger aspect ratio and develop three dimensional shapes.

The advantages of oxide substrates often develop only in combination with another phase, e.g. a metal extended to nanocomponents forming a hybrid or composite structures. Hybrid materials, such as thin film oxides plus metal particles, feature merits from two or more components and potentially synergistic properties caused by interactions among them. For instance, it is well known that nanoscale emitters benefit from metal nanoparticle or nanofilm surroundings [215, 216]. For wide gap semiconductor ZnO, reports have shown that by placing Au or Ag nanoparticles on ZnO nanorods or films, the ZnO's luminescence capability can be enhanced [217, 218]. Metal/ZnO hybrid nanostructures are therefore good candidates to yield high optical efficiencies in optoelectronic devices, for example in lasers and LEDs. The

nanostructure's key parameters need to be optimized carefully, for instance by changing the amount of Au and Ag or mixing several ad-metals on top of ZnO. In the following sections, the interaction of Au, Ag and Cr particles with ZnO will be studied.

Most metal-ZnO hybrid systems in the literature were prepared by wet-chemical methods, e.g. by metal-organic epitaxy [219], solvothermal [220], and electrochemical deposition, techniques that often suffer from a contamination of the samples with parasitic agents. Moreover, fabrication and characterization of the systems are typically performed ex-situ and involve sample transport through air. As it was presented in section 4.2, we have prepared and explored different ZnO hybrid systems in a single, ultrahigh vacuum (UHV) experiment, exploiting a variety of high-purity surface-science techniques. Atomically flat ZnO films grown on Au(111) single crystals are used as susbtrates. The morphology of the precipitated Ag, Au and Cr nanoparticles is studied here with scanning tunneling microscopy (STM), while the optical response is monitored with STM luminescence spectroscopy, already described in section 3.2.1. The optical spectra suggest a limited interaction between plasmonic excitations in the silver and excitons in the ZnO, the efficiency of which could be tuned by embedding the particles into the oxide matrix. Our experiments therefore provide insight into energy-transfer processes in well-defined metal-oxide hybrid systems.

Samples were prepared with the same procedure as descripted in section 4.2.1. Silver, gold and chromium have been evaporated from a Knudsen cell onto the freshly prepared oxide film held at 300 K in different samples. For the hybrid Ag-ZnO system, the Ag-ZnO coupling has been enhanced by covering the metal particles with additional ZnO layers of variable thickness. The Ag-ZnO morphology was further modified by annealing the hybrid system to different temperatures, as described in the following section.

4.4.2 Ag Particles on ZnO

Figure 4.22 displays the growth sequence of silver on a 25 ML thick ZnO film deposited at 300 K. At the lowest exposure, nearly hemispherical particles of approximately (1.5 ± 0.5) nm height and 3-5 nm diameter develop on the oxide surface. After correction for tip-convolution effects, this corresponds to a nominal Ag coverage of 1.5 ML. The oxide surface is homogeneously covered by Ag particles with a mean density of 5×10^{12} cm^{-2}. By doubling the nominal coverage to 3 ML, the mean particle size increases to (2.5 ± 1) nm height and 6-8 nm diameter, while the density decreases to 2.5×10^{12} cm^{-2} due to coalescence effects. At the same time, the particles develop characteristic hexagonal shapes, indicative for their perfect crystalline nature and the Ag(111) orientation of the top facet [221]. We assign the Ag deposits to *fcc* nanocrystals, as it has been already described in the literature [222]. The Wulff construction connects equilibrium geometry with surface-free energy of the dominant crystal facets of the nanoparticles, as it has already been shown in last section. The silver nanoparticles are characterized by large (111) top and side facets interrupted by smaller (100) planes, leading to the hexagonal shape seen in the STM, as seen in Figure 4.22. When the nominal coverage reaches 5 ML, large crystallites with (3.5 ± 1.0) nm height, 8-12 nm width and atomically-flat top facets develop on the oxide surface. In addition, the particle density still decreases to to 1×10^{12} cm^{-2}. This is an indication of

the high mobility of the incoming Ag atoms and the tendency of the metal to coalesce into large deposits on the surface [221]. We would like to highlight the difference in cluster size and density among the different metals studied in our experiments on ZnO thin films. Apparently, silver forms the largest and most compact particles, while the average density of Au and Cr clusters is higher by a factor of 1.4 and 2.2, respectively. This result is further discussed in section 4.4.3. Apparently, the mean particle size decreases when moving Ag to Au and Cr deposition. This trend reflects the chemical inertness and high mobility of silver that is unable to form strong chemical bonds with the hydroxylated ZnO(0001) surface.

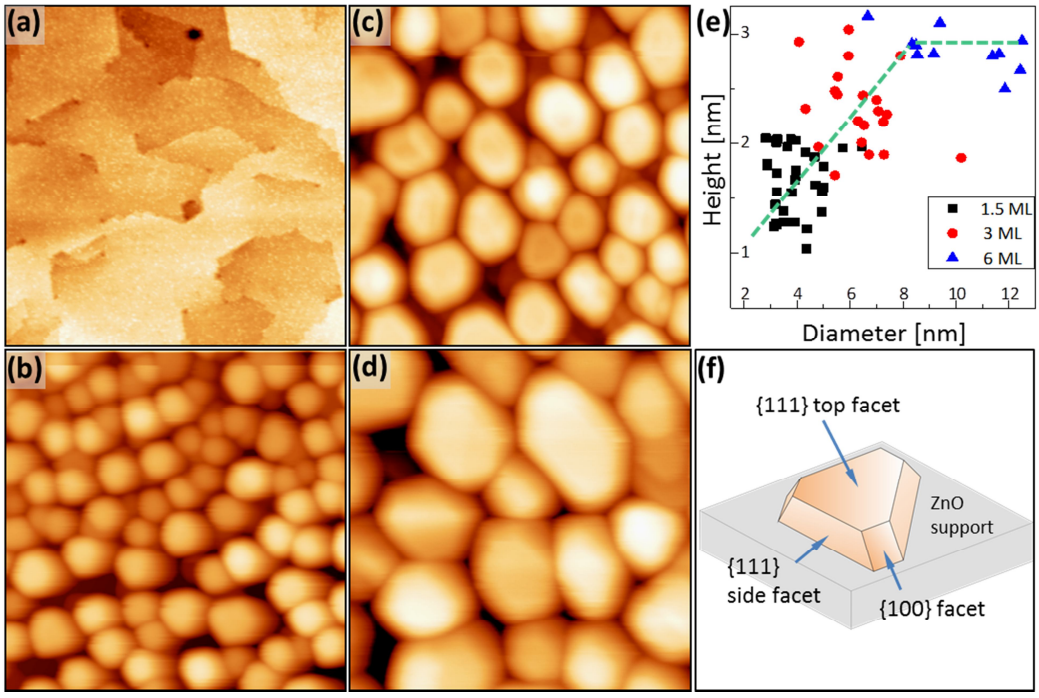

Figure 4.22. (a) STM topographic images of a 25 ML-thick bare ZnO film grown on Au(111) (200 × 200 nm^2, Us = 3.0 V). Similar film after deposition of nominally (b) 1.5 ML, (c) 3.0 ML and (d) 6 ML silver at room temperature (35 × 35nm^2, Us = 3.0 V). (e) Mean height and diameter of Ag deposits for the three depositions in this experiment. The corresponding aspect ratio is 0.4 and a coalescence effect takes place for diameters larger than 8 nm. (f) Model of the hexagonal clusters with top and side facets.

The STM images in Figure 4.23 show the evolution of the Ag-ZnO morphology if the particle ensemble is covered with a top-layer of ZnO. The thickness of the top-layer hereby increases from 2 ML in (a) to 10 ML in (b). Despite the coating, the Ag particles remain distinguishable in all cases and only their shape becomes blurred due to the oxide overlayer. On the other hand, neither density nor mean size of the deposits changes upon embedding in the ZnO matrix. Figure 4.23c finally shows an STM topographic image of an embedded Ag-cluster ensemble (3 ML nominal coverage) after annealing to 500 K in vacuum. Clearly, the particles move towards the surface again upon annealing, where a strong Ostwald ripening process sets in that leads to a decrease in particle density by a factor of 100 (< 2×10^{10} cm^{-2}). Moreover, the particles have grown in lateral dimension to 20-50 nm and developed flat, hexagonal top facets.

This drastic increase of the mean particle size provides further evidence for the weak interface adhesion between Ag and ZnO. In section 4.4.4, we will discuss how the optical properties evolve when preparing Ag particle ensembles with different parameters on top of the ZnO support.

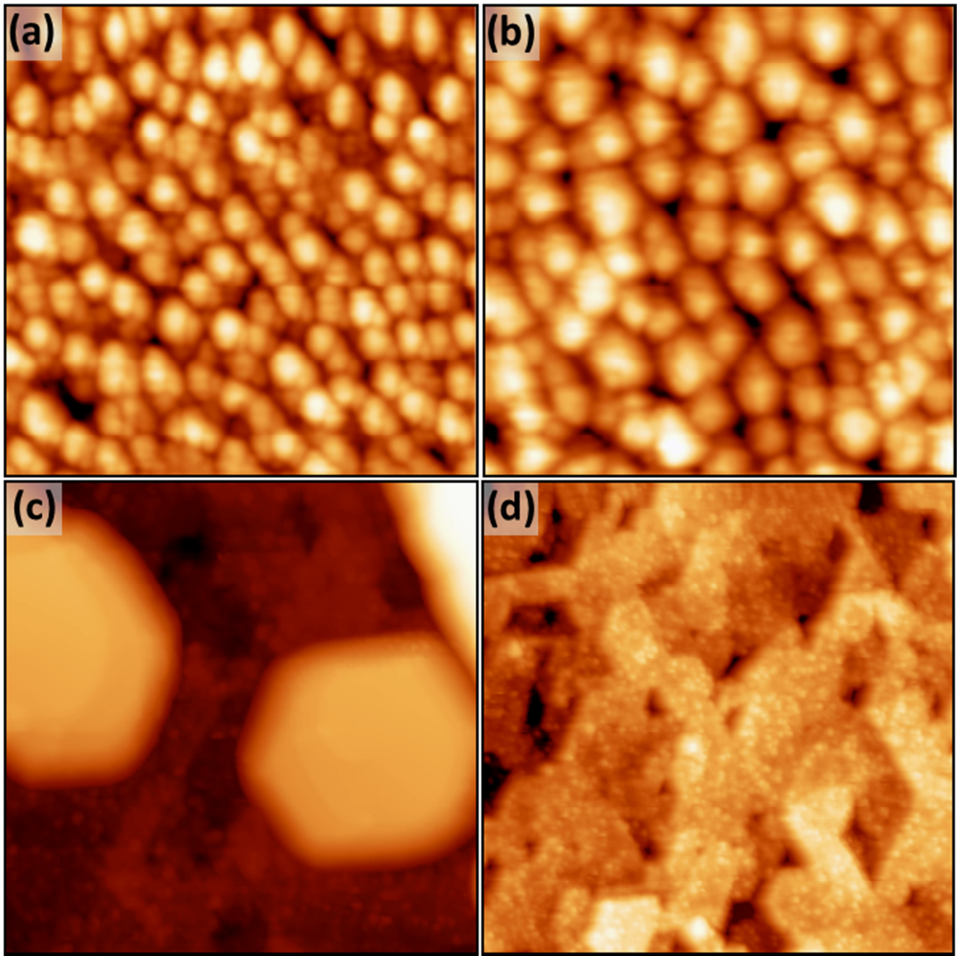

Figure 4.23. STM images of 3 ML silver on ZnO coated with an extra ZnO layer of (a) 2 ML and (b) 10 ML thickness (75×75 nm^2, Us = 3.0 V). Despite the coating, the particles remain discernible. (c-d) Similar sample as in (b) but annealed to (c) 500 K and (d) 700 K after the coating (150×150 nm^2, Us = 3.0 V). Whereas coalescence is the dominating effect at low temperature, the silver evaporates from the surface above 700 K.

4.4.3 Au and Cr Particles on ZnO

In this section, we describe the nucleation of Au and Cr metal particles on polar ZnO(0001) surfaces by analyzing the experimental results obtained from scanning tunneling microscopy (STM). Figure 4.24 shows the evolution of the gold deposits with higher exposure. A significant increase in the gold particle density is observed when compared with the silver particles: $7x10^{12}$ cm^{-2} for Au and $5×10^{12}$ cm^{-2} for Ag, both for 1.5 ML nominal exposure, as described before. In line with the increased particle density, the Au diameter is smaller than the Ag one. This effect is explained by a

stronger adhesion of gold in comparison to silver, which may be traced back to a higher electronegativity of the former. Silver, on the other hand, is known to interact weakly with oxide supports.

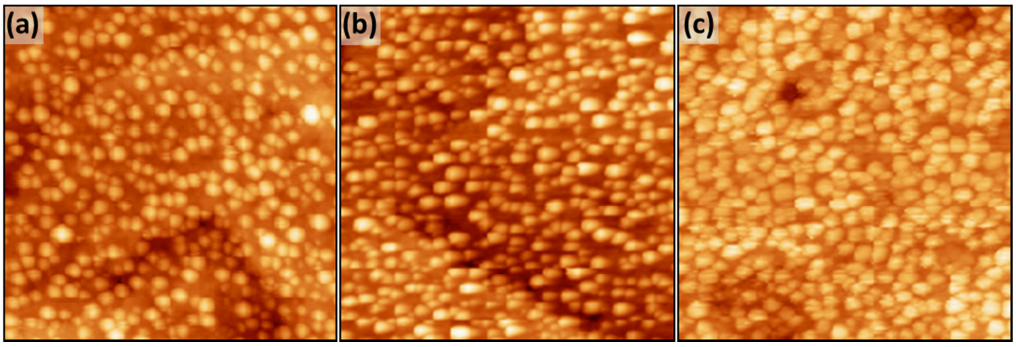

Figure 4.24. STM Images of Au on ZnO support. (a) 1.5 ML, (b) 3ML and (c) 6ML of deposited gold. (80 × 80 nm^2, Us = 4.0 V). In comparison with Ag particles, gold particles are smaller and have a bigger density, as explained in the text.

The next element considered here is Cr, which is a transition metal. Transition metals show a high affinity towards oxygen, although typical heats of oxidation are smaller than for simple metals and largely spread across the periodic table [223]. This phenomenon reflects the influence of the metal *d* states, more precisely of their energy, symmetry, and electron filling, on the reactivity. For this study we have chosen Cr, which is a d^4 material. Similar to Au, Cr clusters grow homogeneously on the surface with a high density ($11x10^{12}$ cm^{-2}), as shown in Figure 4.25. The high density reflects the reactivity of Cr on the polar ZnO surface. To quench the intrinsic polarity of O-terminated ZnO(0001), one positive charge per 2x1 unit cell is required. Cr is an easily oxidable metal, and therefore ideally suited to quench the polarity of ZnO. This Cr density is the highest compared to the other metals grown on the same ZnO(0001) surface (Figure 4.25d). However, the Cr particles exhibit an even larger density of $3x10^{13}$ cm^{-2} when being annealed at 800 K after adding another ZnO layer with 5ML thickness on top, as shown in Figure 4.25c. We think that OH groups partially compensate the surface polarity before the nucleation of the Cr clusters takes place, like in Figure 4.25a and b. On the other hand, the OH groups are gone with the annealing at 800 K and the metal particles are fully responsible for polarity compensation of the ZnO film, leading to the formation of small and rather dense particle ensembles (Figure 4.25c).

We also want to compare of the cluster densities for Au, Ag and Cr for both polar (ZnO) and non-polar oxides (MgO). For MgO substrates, the densities are higher for reactive metals (like the transition metals Fe and Cr) than for Au and Ag [224]. For ZnO as a polar material, the trends are the same $\left(n_{Cr} > n_{Au} > n_{Ag}\right)$, however, absolute densities are much higher as for MgO. This difference reflects the role of polarity for ZnO. Polar oxides exhibit, in general, a stronger adhesion to metals, as the metals help to compensate the electrostatic dipole [163, 165, 167]. On the other hand, many polar oxides hydroxilate spontaneously, and the OH-groups strongly reduce the mobility of the incoming metal atoms. The result is much higher densities as for non-polar oxides. This trend has been confirmed by dosing gold onto a fully hydroxilated MgO(001)

surface (prepared by dosing H_2O at 10^{-3} mbar). Also here, extremely high Au cluster densities were found although MgO(001) is intrinsically a non-polar surface.

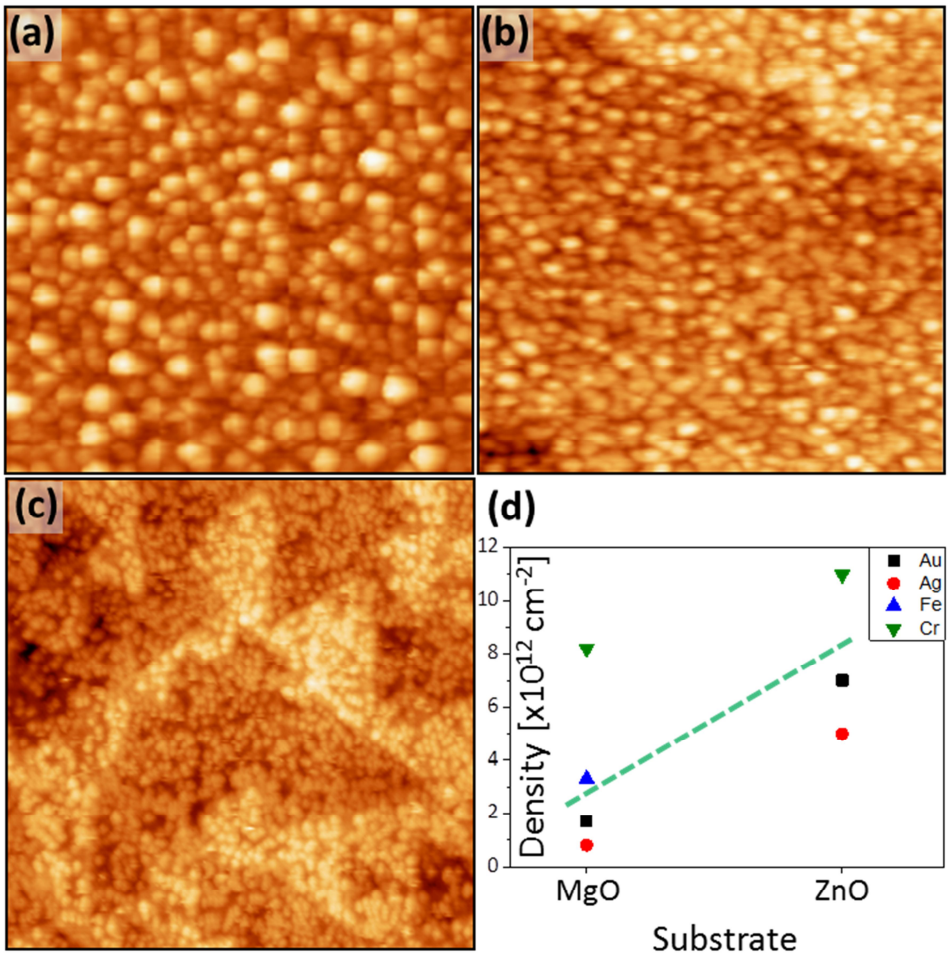

Figure 4.25. STM Images of Cr particles on ZnO: (a) 1.5 ML and (b) 5ML. Image (c) corresponds to 1.5 ML Cr deposited on ZnO with a cover layer of 5ML ZnO and after being annealed in $2x10^{-5}$ mbar O_2 at 800 K. (80×80 nm^2, Us = 4.0 V). (d) Comparison of metal particles densities in non-polar (MgO) and polar (ZnO) surfaces.

4.4.4 Optical Properties of the Ag-ZnO Hybrid System

We studied the optical response of the Ag-ZnO system by means of STM luminescence spectroscopy. The conditions of the measurements are similar to the ones described at the beginning of section 4.3. Figure 4.26 shows the characteristic STM luminescence spectra taken at each step of our experimental series that includes preparation of bare ZnO, deposition and embedding of the Ag particles and several annealing steps. The conclusions drawn from our work are based on several of such runs, all of them showing similar although not identical optical signatures. The black curve at the bottom of Figure 4.26 displays the emission response of bare ZnO, as described in detail in section 4.3.1. Just to remind the reader, the three main peaks (373 nm, 535nm and 730 nm) have been assigned to band-gap recombination, Zn and O vacancies, respectively.

Deposition of nominally 3 ML of silver leads to immediate changes in the optical spectra (Figure 4.26, blue curve). First, all ZnO-related peaks loose about 50% of their intensity, which is readily explained with a capping of the film by the nanoparticles that block the impact of the tip electrons and suppress the oxide luminescence. In addition, two new emission maxima emerge in the spectra, a low-wavelength band at 315 nm (3.9 eV, FWHM 430 meV) and a broad, high-wavelength band at 600 nm (2.1 eV, FWHM 590 meV). The peaks are directly related to the Ag deposits and intensify upon increasing the Ag exposure onto the surface. We will show in the next paragraph that the two maxima are the optical fingerprints of plasmon modes in the Ag deposits. When covering the particle ensemble with a 10 ML thick ZnO ad-layer, the plasmon-related peaks smear out and shift to longer wavelengths. Interestingly, the ZnO emission does not recover at this point, most likely because the top-layer has insufficient crystallographic quality to enable radiative exciton decay.

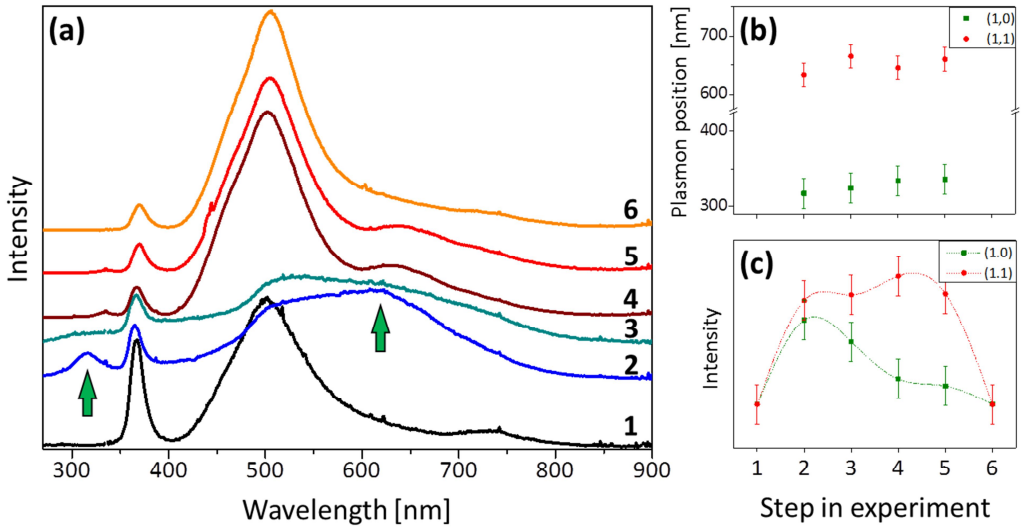

Figure 4.26. (a) STM luminescence spectra of (1) bare ZnO, (2) after 3 ML silver exposure, (3) after coating with 10 ML ZnO and (4-6) after annealing to 500, 600 and 700 K. The insets show the evolution of (b) the position and (c) the intensity of the (1,0) and (1,1) plasmon peaks of silver after substracting the ZnO contribution.

The situation only changes upon gently annealing the sample to temperatures between 350 and 700 K. After a first heating step (red curve), the Ag plasmon peaks sharpen again, as the vacuum environment of the deposits partly recovers at this point. The peaks also experience a red-shift, i.e. the low-wavelength and high-wavelength maxima move to 335 nm (3.7 eV / -0.2 eV) and 640 nm (1.9 eV / -0.2 eV), respectively. These new positions remain constant during further annealing of the sample, however the peak intensity continuously drops. Half of the original intensity is gone after annealing the sample to 500 K and the plasmon emission completely disappears beyond 600 K. Even after silver removal, the ZnO-bands are not fully restored. Whereas the band recombination peak gains only half of its initial height, the Zn-defect emission even intensifies, suggesting that the number of Zn vacancies raises along the preparation series. Possible reasons for this behavior will be discussed in the following section.

Interpretation of the Optical Data

In comparison to the emission peaks observed for bare ZnO films, as for instance the band-recombination and Zn-defect emission lines, the growth of the silver particle ensemble adds a plasmonic component to the optical spectra. From calculations of the energy-dependent polarizability $\alpha(\omega)$ of a metal spheroid in a dielectric matrix, as already introduced in section 2.1.6, the plasmon energy can be estimated by the following equation [73]:

$$\alpha(\omega) \propto \frac{\varepsilon(\omega) - \varepsilon_m}{3\varepsilon_m + 3L_{\perp,\parallel}\,[\varepsilon(\omega) - \varepsilon_m]}. \tag{4.20}$$

Here, $\varepsilon(\omega)$ is the experimentally determined dielectric function of silver [225] and ε_m is the average dielectric constant of the surrounding medium composed of the ZnO film below ($\varepsilon_r = 3.7$) [148] and the vacuum above the deposit ($\varepsilon_r = 1$). The depolarization factors L considered in the formula (4.20) describe the particle shape, as it is derived from experimental aspect ratios. The $L_\perp$ component represents the vertical polarizability of the deposit and accounts for out-of-plane (1,0)-type of plasmons. On the other hand, the $L_\parallel$ factor describes the horizontal polarizability and is used to compute the in-plane (1,1) modes. According to the ellipsoidal model, the different depolarization factors add up to one, as follows:

$$2(L_\parallel) + L_\perp = 1\,. \tag{4.21}$$

For the case of non-embedded, prolate Ag particles described by an aspect ratio of 0.5, the two plasmon modes are calculated to be at $\hbar\omega_{1,0} = 3.8\,eV$ and $\hbar\omega_{1,1} = 2.3\,eV$. Both values agree with the new emission maxima at 3.9 and 2.1 eV, emerging after silver exposure to the ZnO film and they are consequently assigned to the vertical and horizontal plasmon modes of the Ag deposits. Nevertheless, there is a small discrepancy, which is attributed to the disregard of particle-particle interactions that are constructive for in-plane modes, lowering their energy, but destructive for out-of-plane oscillations, as described in section 2.1.6.

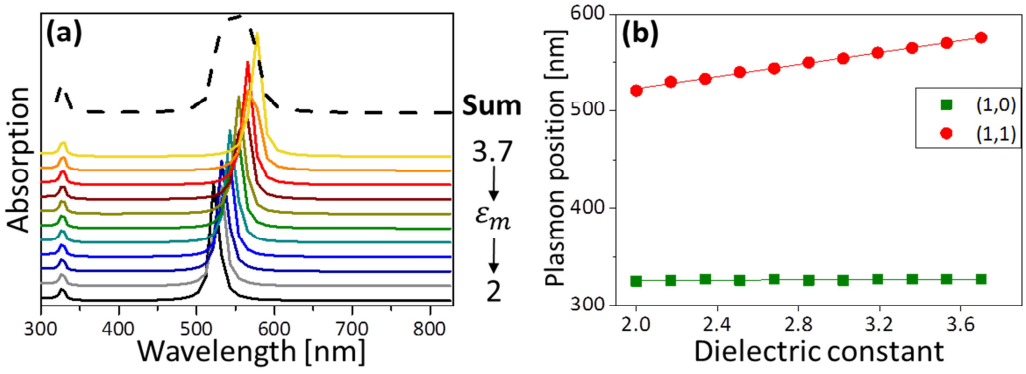

Figure 4.27. (a) Calculated absorption spectra of prolate Ag particles embedded in different dielectric environments. Whereas $\boldsymbol{\varepsilon_m = 2}$ corresponds to a surface-bound deposit, $\boldsymbol{\varepsilon_m = 3.7}$ reflects a particle that is fully embedded in ZnO. (b) Evolution of the (1,0) and (1,1) plasmon energy as a function of the dielectric environment.

This interpretation is in line with experimental data in the literature, as revealed for Ag deposited onto ZnO nanorods or embedded in a ZnO matrix [226]. Prominent luminescence peaks appear at 600nm in both cases and their explanation is found in the excitation of low-lying (1,1) modes in the particles. On the other hand, the high-lying (1,0) plasmon has not been observed so far, most likely because it is situated outside the fundamental ZnO gap and therefore damped by efficient metal-to-oxide energy transfer.

In order to increase the coupling efficiency to excitons in the oxide, the Ag nanoparticles were coated with an extra ZnO layer of 10 ML nominal thickness in the following step of our experiment. We observed that the Ag plasmon modes experienced a substantial broadening and shifted towards higher wavelengths (Figure 4.26, cyan curve). An increasing influence of the dielectric surrounding on the collective excitations controls this behaviour. The as-deposited particles are in contact with the ZnO only at their bottom, while the majority of the Ag surface is exposed to vacuum. Therefore, the effective dielectric constant can be estimated with an average of 35% ZnO and 65% vacuum interface. This consideration yields an effective value of ε_m of 2. In case of a cover ZnO top layer, the vacuum surface gets replaced by a ZnO-Ag interface and the effective dielectric constant therefore increases. Due to the fact that the full dielectric response of the oxide is in place only for layer thickness of the order of the wavelength of light, the increase in ε_m is rather gradual and does not reach the bulk value for ZnO ($\varepsilon_m = 3.7$) [73]. The change in the plasmon response due to the ZnO coating is however evident, both in the experiment and our polarizability simulations (Figure 4.27a). Upon increase of ε_m, the calculated in-plane resonance $\hbar\omega_{1,1}$ undergoes a redshift from 2.3 to 2.1eV, a trend that is clearly resolved in the experimental data as well. At the same time, the peak exhibits a broadening, which is ascribed to be a distribution of layer thicknesses on top of the Ag deposits and the resulting scatter of plasmon frecuencies. For a better illustration of this idea, we have summed over the polarizabilities of Ag particles in different dielectric environments, as shown in Figure 4.27a, dashed line. The subsequent increase of the FWHM of the (1,1) plasmon is in qualitative agreement with the experimental data. It is important to highlight that in addition to the broadening, the (1,0) mode exhibits a loose of its integral intensity when coating the Ag particles. We relate this effect as experimental evidence for an energy transfer between the energetic plasmon mode and electron-hole pairs in the oxide. Unfortunately, the lower emission yield of the ZnO film does not reflect this energy exchange, especially because an increase would be expected from the anticipated role of Ag particles as optical sensitizers, as described in the literature [226-228]. Our interpretation is that the low crystallographic quality of the ZnO over layer is responsible for the missing enhancement effect. Apparently, the room-temperature-grown ZnO offers too many non-radiative recombination channels to feature plasmon-mediated luminescence enhancement. In order to investigate this topic, we have gently annealed the Ag-ZnO hybrid systems in the last stage of this experiment.

Upon annealing, the plasmon signature of the Ag-ensemble reappears and the situation turns to be similar than the one without the ZnO cover layer. The spectra show both the (1,0) and (1,1) resonances as relatively sharp peaks at 335 (3.7 eV) and 640 nm (1.9 eV), respectively, but are systematically red-shifted by about 0.2 eV. STM

topographic images help to understand the reason for this shift. The annealing brings the Ag deposits to float again towards the surface, while the extra ZnO merges with the thick film and partly embeds the nanoparticles. Moreover, the overall size of the deposits increases and their aspect ratio become smaller, as shown in Figure 4.23c. The shift of the plasmon peaks is attributed to the evolution in the particle geometry as well as to the change in the dielectric environment. Whereas flattening of the particle mainly affects the in-plane resonance that shifts to higher wavelength, the out-of-plane mode hardly changes (Figure 4.27b). On the contrary, this mode is more sensitive to the dielectric environment and shifts towards the red as the particle sinks into the oxide film. After the thermal treatment both peaks become sharper, which indicates an increasing structural homogeneity of the system.

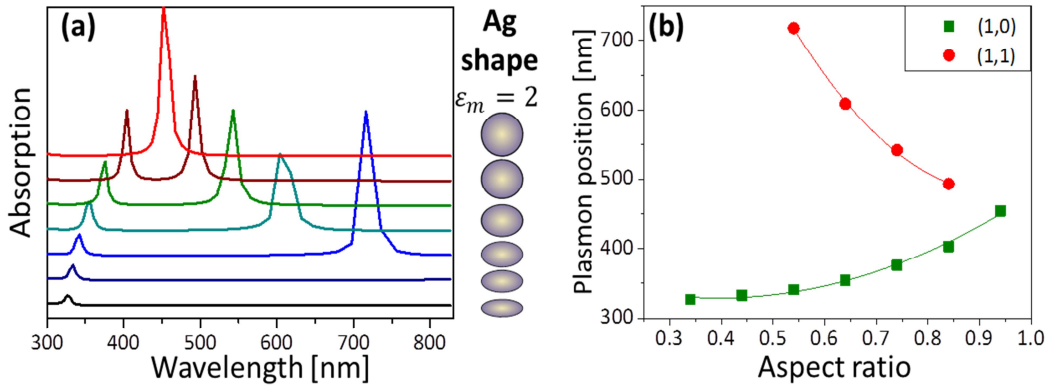

Figure 4.28. (a) Calculated absorption spectra of surface-bound Ag particles of different shape. (b) Evolution of the (1,0) and (1,1) plasmon energy as a function of the particle aspect ratio

Another trend starts dominating the spectral response when the temperature rises: the loss of plasmon intensity due to the evaporation of silver from the film. While the peaks are still discernable after 500 K annealing, only the bare ZnO emission remains after heating to 700 K. However, the ZnO signature does not fully recover even after removal of the ad-metal. Two differences are apparent in comparison with the initial spectra (black curve in Figure 4.26): the band recombination peak has dropped by roughly a factor of three and the Zn vacancy peak has gained intensity. We address the first effect to the loss of crystallographic quality due to the addition of silver and amorphous oxide to the original film. On the other hand, the formation of additional Zn defects explains the second effect. More Zn vacancies might indicate a larger electron density in the lattice (increasing n-type character). Two sources for excess electrons are likely to be present. Traces of silver in the ZnO matrix, either as particles or as single atoms, may serve as electron donors, in agreement with the low Ag workfunction and the high electron affinity of ZnO [229]. On the other hand, Ag ions might have entered the wurtzite lattice in the deposition and embedding procedure, where they substitute some of the Zn ions. In subsequent annealing steps, these weakly bound impurities have left the lattice, increasing the density of cationic defects. Independently of the Ag exposure, we found an increase of the Zn-defect peak when ZnO samples were annealed in an excess of oxygen, as already described in the literature [31].

To sum up, we have prepared different metalic particle ensembles via physical vapor deposition onto a crystalline and atomically flat ZnO film, in order to elucidate the

nature of metal-oxide interactions. Noble metal particles show a higher denstity when they grow on a polar system like ZnO. To make a clear comparison, the particle density values have been determined on a non-polar substrate, such as MgO, being considerably lower. Furthermore, transition metal particles show still higher densities due their larger reactivity and affinity to oxygen. Charge compensation of the polar surface seems therefore to be a decisive factor for the particle growth.

On the other hand, energy transfer processes between plasmonic and excitonic systems have been studied for the silver-ZnO system. We found that as long as the nanoparticles reside on the surface, coupling between both systems is negligible and the superposition of the two plasmon peaks $\hbar\omega_{1,0}$ and $\hbar\omega_{1,1}$ appear on the luminescence spectra. Also the ZnO related peaks due to band-recombination and Zn-vacancy emission are present, as described in detail in section 4.3.1. The coupling between the sub-systems develops when embedding the particle ensemble into an extra ZnO layer. The plasmon resonance follows the changing dielectric environment with a pronounced red-shift and a broadening, whereas the ZnO emission remains essentially constant. We have not observed the expected luminescence enhancement due to energy transfer from plasmonic to excitonic modes. We explain the absence of this coupling with the low quality of the Ag-ZnO interface and the abundance of structural defects in the ZnO overlayer. In addition, the oxide cover is probably too thin to allow for an efficient absorption of the plasmon energy. After annealing, the silver floats to the ZnO surface and the metal-oxide coupling strength decreases again. In order to keep the particles covered even after thermal treatment, ZnO coatings of larger thickness should be used in future. However, the STM turns more and more unsuitable for such kind of experiments, since the Ag particles are inaccessible to topographic and optical measurements with increasing depth below the surface. Thus, the corresponding studies should be performed with classical optical techniques, even though this implies a loss of spatial resolution in comparison to STM techniques.

4.5 Growth of ZnO Nanorods on Au(111)

Besides the properties described in the last sections, ZnO is a versatile functional material that has diverse growth morphologies, such as nanocombs, nanorings, nanohelixes, nanosprings, nanobelts, nanowires and nanocages, and others. The aim of this chapter is to present the results of the investigations related to the growth of ZnO in different environments as presented in section 4.2. Indeed, the present part of the thesis deals with the growth of ZnO nanostructures that have been studied in our group by means of the STM-based techniques presented in section 3.2.1 [117].

4.5.1 ZnO Nanostructures

Nanostructured ZnO materials have received broad attention due to their outstanding performance in electronics, optics and photonics. Since the beginning of the late 1960s, synthesis of ZnO thin films has been an active field due to their broad spectrum of applications. In the last few decades, however, the investigation of one-

dimensional (1D) materials has become a leading edge in nanoscience and nanotechnology [230]. These structures are reduced in size so that they develop novel electrical, mechanical, chemical and optical properties in comparison with thin films. Nanowire structures serve as a good starting point for studying the transport processes in one-dimensionally (1D) confined objects. Not only the understanding of fundamental 1D phenomena benefits from that, but also the development of a new generation of nanodevices with high performance does.

The different surface structures of ZnO could induce anisotropic growth. Under certain thermodynamic conditions, the facet with higher energy is usually smaller in area, while the low-energy facets become larger. For the growth of ZnO in particular, the highest growth rate is along the *c*-axis (Figure 4.1) and the large facets are usually of $\{01\bar{1}0\}$ and $\{2\bar{1}\bar{1}0\}$ type. A few typical growth morphologies of 3D nanostructures of ZnO are shown in Figure 4.29. These structures tend to maximize the areas of the two facets mentioned before, because they are energetically more convenient. The morphology in Figure 4.29d is controlled by polar surfaces that can be grown by introducing planar defects parallel to the polar surfaces [231]. Planar defects and twins are unusually observed parallel to the {0001} plane, but dislocations are rarely seen. By controlling the kinetics, a change of the growth behaviour of ZnO nanobelts becomes possible. The following section aims to present common nanostructures developed in ZnO, such as nanorods, ultralong nanobelts with diverse facets, nanocombs, branched hierarchial structures, nanohelixes and nanorings, among others. The parameters that play a key role for the growth of different structures will also be discussed. Normally, these parameters are the deposition temperatures and pressures as well as carrier gas flux.

Typically, these type of nanostructures are produced following the vapor-liquid-solid (VLS) growth [170]. In this approach, a liquid alloy droplet is formed under reaction conditions. The composition of the alloy droplet involves a metal catalyst component (such as Au, Fe) and a nanowire component (such as Si, III-V compound, II-V compound, oxides). The selection of the metal catalyst comes from the phase diagram that identifies those metals in which the nanowire components are soluble in the liquid phase. Moreover, the chosen component elements should not form solid compounds that are more stable than the desired nanowire phase. For 1D ZnO nanowires grown via a VLS process, the commonly used catalyst is gold [232]. The liquid droplet acts as a preferential site for absorption of the gas phase reactant. In case of supersaturation, it acts as the nucleation site for crystallization. After the liquid becomes supersaturated in the reactant species, nanowire growth begins. It continues, providing that the catalyst alloy remains in a liquid state and the reactant is available. During growth, the catalyst droplet directs the growth direction and defines the diameter of the nanowire. The growth finishes when either the temperature is below the eutectic temperature, or when the catalyst alloy or the reactant is not available any more. As a consequence, a nanowire obtained from the VLS process typically has a solid catalyst nanoparticle at its tip with a diameter comparable to that of the connected nanowires. This fact plays a key role for the interpretation of our UHV experiments. Figure 4.30c shows a SEM image of a nanowire.

The VLS growth mechanism was first proposed by Wagner and Ellis [233] in 1964 for Si whisker growth. Whiskers of Si with diameters of up to one micrometer were grown

by means of hydrogen reduction of $SiCl_4$, with the presence of Au, Pt, Ag, Pd, Cu, and Ni as the catalysts. This method was later improved by Westwater *et al* [234] and Lieber *et al* [235]. They prepared nanometer scale silicon wires by means of pyrolysis of SiH_4 with Au playing the role of the catalyst and laser ablation of $Si_{0.95}Fe_{0.05}$ targets, providing the reactants.

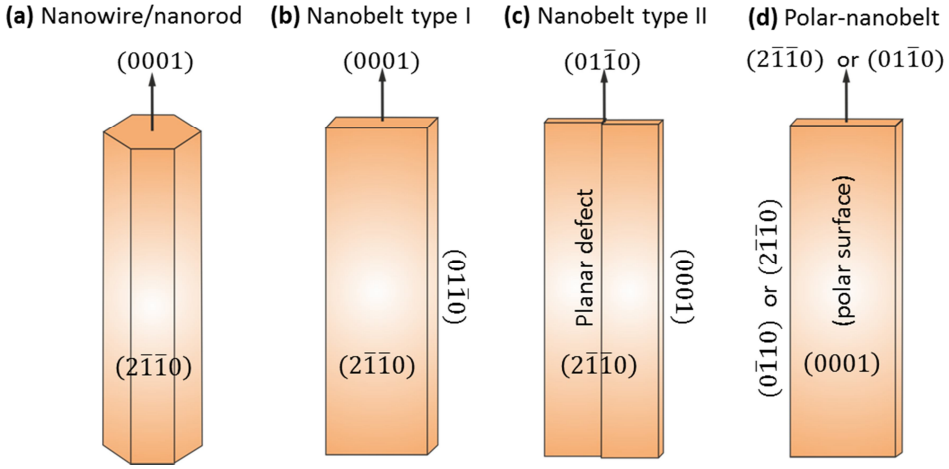

Figure 4.29. Typical growth morphologies of ZnO nanostructures and the corresponding facets [170]

By modifying the composition of the source materials, the morphology of the grown nanostructure changes drastically. This is the case of the hierarchical nanostructures, which show a complex morphology that appears after mixing ZnO and SnO_2 powders in a weight ratio of 1:1 [236]. Similar structures can be achieved for ZnO, in which the arms of crystalline tetrapod staples interlock with each other by forming strong bonds. Tetrapods are nothing more than four arms pointing away from a central point, as shown in Figure 4.30a. ZnO tetrapods play a key role for the stickiness of silicon and Teflon to each other [237].

In addition, "comb-like" structures of ZnO have been reported. However, the mechanism that drives the growth has not been elucidated until recently [238]. The comb structures, as shown in Figure 4.30b, tend to have comb teeth growing along the (0001) direction.

On the other hand, nanobelts are wires that have well-defined geometrical shapes and side surfaces. Nomally, nanobelts are grown by sublimation of ZnO powder without growth catalyst, as it can be seen in Figure 4.30d [239]. Ultranarrow nanobelts, a small version of the first mentioned structure, are used for investigation of the quantum confinement effect [240].

The role of the chemical potential is decisive for the shape of the final structures of this interesting material, as it was introduced in section 4.1.4. Once again, the parameters that are involved in the formation of the structures are the local temperature and the partial pressures. The chemical potential μ_O can be related to the experimental conditions, which can be either Zn-rich, O-rich or anything in between. Therefore, it is explicitly considered as a variable in the formalism. Nonetheless, the thermodynamic equilibrium and the stability of ZnO impose constraints on the chemical potential. The upper bound of the oxygen chemical potential is connected to the energy of oxygen in an O_2 molecule, namely $\mu_O^{max} = 1/2\, E_{tot}(O_2)$. This expression

corresponds to extreme oxygen-rich conditions. Similarly, an upper bound is given to the zinc chemical potential μ_{Zn} and is related to the energy of Zn in bulk zinc, $\mu_{Zn}^{max} = E_{tot}(Zn)$, which corresponds to extreme Zn-rich conditions. At this point, it is important to highlight that μ_O and μ_{Zn} are temperature and pressure dependent [120].

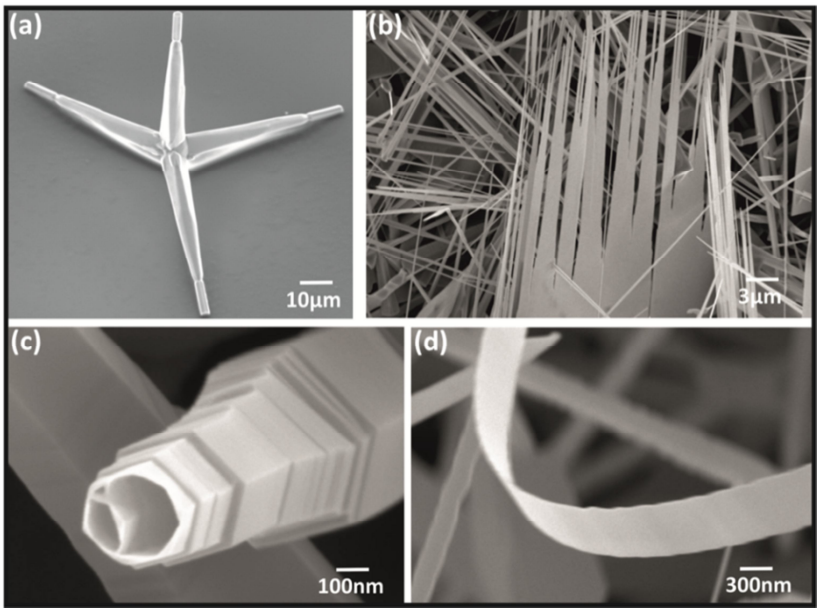

Figure 4.30. SEM images of different ZnO nanostructures: (a) tetrapod [237], (b) nanocombs, (c) nanowire, and (d) nanobelt [241]

As mentioned above, ZnO nanostructures are mostly fabricated by high-throughput techniques, while surface science approaches, e.g. physical vapour deposition in an UHV environment, combined with high-end topographic and spectroscopic characterization are rarely used [242]. In some cases, the atomic structure [168], adsorption characteristics [243], and polarity compensation schemes [169] of crystalline ZnO surfaces have been already characterized by means of scanning tunneling (STM) and atomic force microscopy (AFM). Furthermore, homogeneous oxide films were prepared and characterized at the atomic scale on a variety of metallic and dielectric substrates, such as Pd(111) [161], Au(111) [113], Pt(111) and Al_2O_3 (1010) [125]. However, systematic growth studies of 3D oxide structures, exploiting the full arsenal of surface science methods, are hardly found in the literature. This is a somewhat unsatisfying situation, as surface science techniques provide ultraclean and highly reproducible preparation conditions for oxide nanostructures, as well as various tools for their in-situ characterization. By exploiting these advantages, a deeper insight into fundamental growth properties of ZnO could be achieved and used to extend the existing picture [28, 170].

In this section, the growth behaviour of ZnO on Au(111) is presented in a different modality as showed in section 4.2.2. The switch from a layer-by-layer mode, giving arise to flat, crystalline films, to a 3D regime that leads to the development of nanorodos will be studied. These nanorods are oriented along the surface normal and expose relatively constant height-to-diameter ratios. The crucial parameter controlling the different

growth regimes turns out to be the oxygen chemical potential. Moreover, the nanorod formation is catalyzed by traces of Au that accumulates on the surface of ZnO/Au(111) films at certain conditions. This fact is supported by highly resolved STM data.

The preparation conditions were similar to the ones presented in section 4.2.1. Sublimation of ZnO pellets from an e-beam evaporator was done onto a sputtered and annealed Au(111) single crystal in $5x10^{-6}$ mbar of oxygen. The nominal film thickness was intended to be 25 ML. The crystallinity of the films was ensured by an annealing step for 10 minutes to different temperatures either in vacuum or in O_2 ambience. This last step turned out to be crucial for the dimensionality of the ZnO structures, adopting either 2D other 3D morphologies. Once again, the quality of the films was checked by means of low energy electron diffraction (LEED). The result was an intense, hexagonal spot pattern indicative for the {0001} termination of the wurtzite lattice, as shown in Figure 4.31c, and similar to the ones already presented in Figure 4.7, 4.8 and 4.13.

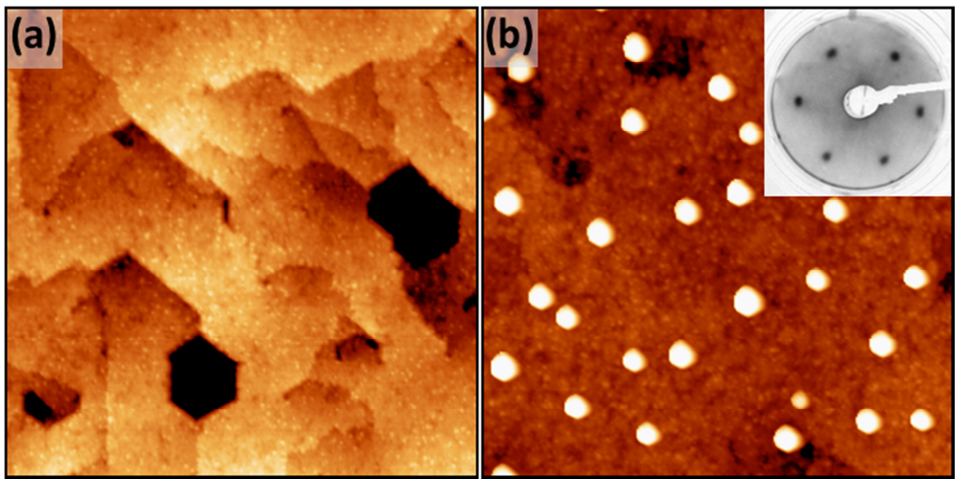

Figure 4.31. (a) and (b) STM images of flat ZnO on Au(111) and a film homogenously covered with ZnO nanorods (Us = 4.0 V, 200 x 200 nm^2). The inset in (b) shows the corresponding LEED pattern of the flat film taken at 100 eV electron energy.

The two manifestations of our ZnO samples flat films versus nanorods are shown in Figure 4.31. Flat films were already analyzed in the previous chapters of this thesis; however, they are presented again for comparison. Whereas a flat film with wide terraces of triangular or hexagonal shape is observed in Figure 4.31a, a nanorod-array sitting on top of a ZnO wetting layer is identified in Figure 4.31b. There is only one dividing preparation step in the two cases and this was the final annealing. While sample (a) was tempered at 700 K in $5x10^{-6}$ mbar of oxygen, sample (b) was vacuum-annealed at 800 K. As it can be seen, this small variation in the annealing procedure is sufficient to induce drastic changes in the growth morphology of the oxide. Both, the ZnO wetting layer and the nanostructures are clearly of crystalline nature, as deduced from the sharp LEED pattern of the film and the distinct geometry of the nanorods, respectively. Top facets of the nanorods are always hexagonal in shape, indicating a {0001} termination similar to that of the film (Figure 4.29a). In a first model, the side facets are assigned to $\{2\bar{1}\bar{1}0\}$ planes, as it is also depicted in Figure 4.29a. These planes are characterized by low formation energies and are often observed in ZnO nanostructures [170, 244]. Depending on the preparation conditions, the experimental

aspect ratio, height-to-diameter, varies between 0.1 and 0.2 for our nanorods, as depicted in Figure 4.32. These last values are considerable smaller than for ZnO nanorods prepared by wet-chemical methods. However, the aspect ratio should be taken as a lower bound, as the rod diameter was not corrected for tip convolution effects.

4.5.2 Impact of the Oxygen Chemical Potential on the ZnO Morphology

Detailed inspection of the data reveals a direct correlation between the geometry of the ZnO nanorods and the specific annealing conditions. In order to enable comparability of all experiments, the concept of oxygen chemical potential μ_O is introduced. As mentioned before, this takes into account the oxygen partial pressure p and the annealing temperature T and is described by the following expression [245]:

$$\mu_O = kTln\left(\frac{p}{p_O}\right). \tag{4.22}$$

In this expression, k stands for the Boltzmann constant and p_O is the atmospheric pressure. The volume ratio $V_{Nanorod}/V_{Film}$ between the nanorods and the absolute amount of deposited material that corresponds to 25 ML in all cases aims to quantify the dimensionality of the ZnO. The nanorod volume is hereby estimated by measuring height and diameter of all ad-structures in a characteristic surface region (e.g. 100x100 nm^2), treating the rods as perfect cylinder. The lateral rod size was not corrected for tip convolution effects, causing V_{rod} to be overestimated by about 25%. However, this systematic error has no consequences for the general conclusions of our analysis, which addresses relative instead of absolute trends.

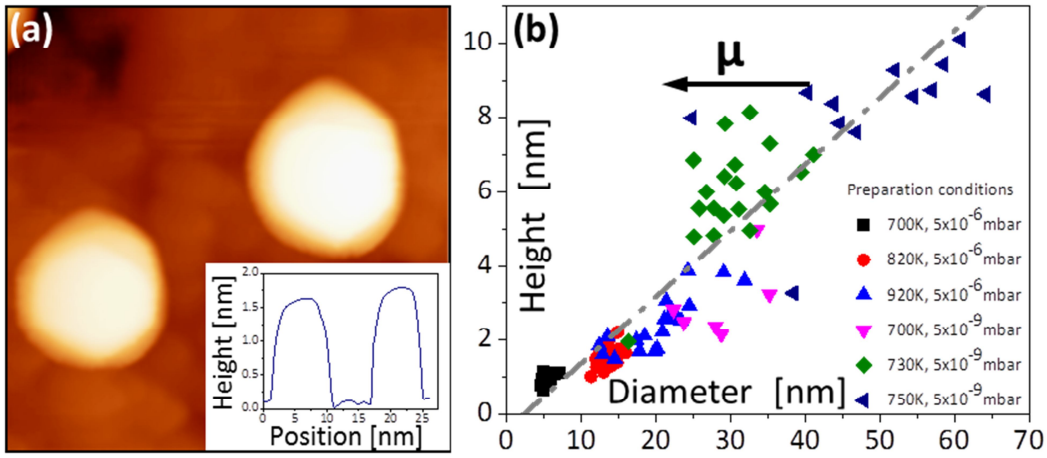

Figure 4.32. (a) Close-up STM image of two nanorods on ZnO/Au(111) (4.0 V, 30 x 30 nm^2). (inset) Height profile across the geometrical middle of the rod. (b) Histogram of height-to-diameter ratios for nanorods produced at different preparation conditions (see symbols). The mean aspect ratio of the rods amounts to 0.15.

Figure 4.33 ilustrates the dependence of the oxide dimensionality on the O_2 chemical potential. Apparently, the nanorod contribution to the total film volume

continuously increases with decreasing O_2 chemical potential. Whereas flat ZnO films develop at low-temperature and/or oxygen-rich annealing conditions on Au(111), pronounced 3D structures are formed upon high-temperature annealing in an O_2-poor environment. A selection of ZnO preparations that depicts this trend is shown in Figure 4.33 a, b and c.

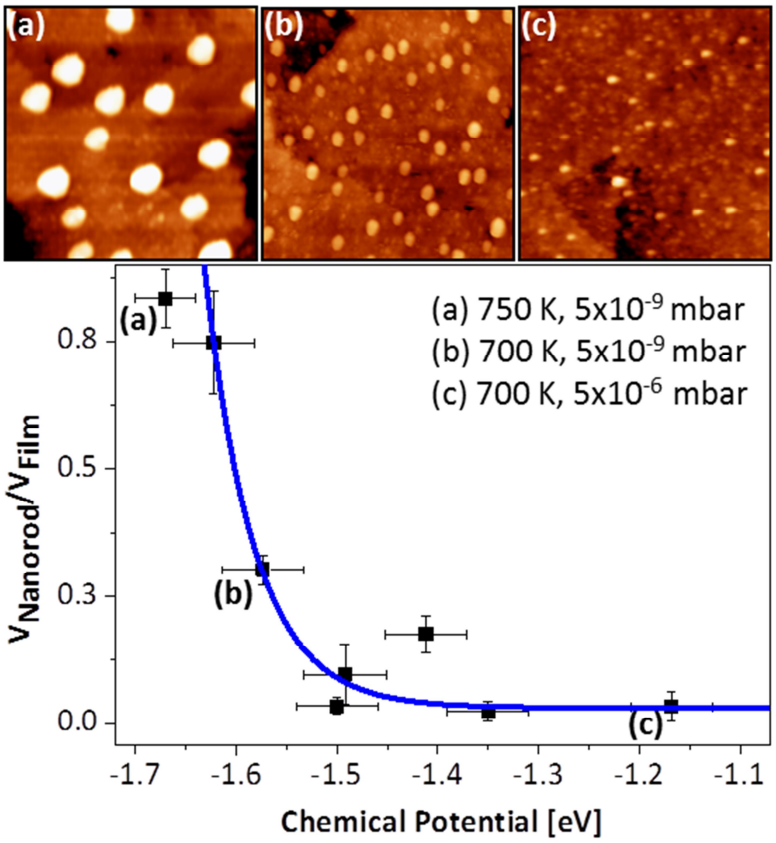

Figure 4.33. Ratio between nanorod volume and total amount of deposited material, plotted as a function of the oxygen chemical potential. An exponential relationship has been fitted as guide to the eye. Inset: images for preparations at (a) 750K and $5x10^{-9}$ mbar, (b) 700K and $5x10^{-9}$ mbar, and (c) 700K and $5x10^{-6}$ mbar (Us = 2.4 V, 100x100 nm^2). Note the varying density and size of the ZnO nanorods.

In addition to the quantification of the topographic behaviour, the material composition of the nanorods has been studied. Indeed, it was demonstrated that nanorods are made of ZnO and do not contain un-reacted Zn metal or gold segregated from the support. This conclusion has been drawn from two different experiments. First, STM conductance spectra have been acquired on top of the nanorods and on the flat films via lock-in techniques (Figure 4.34a). In both cases, the curves clearly reveal the oxide band gap, which is characterized by a broad zero-conductance region around the Fermi level. The conduction-band edge is consistently found at +0.5 V, while the onset of the valence band varies between -1.5 and -2.5 V. This variation depends on the setpoint value for spectroscopy and not on the actual tip position above a nanorod or the flat film. Normally, a more negative band-onset is revealed for a larger setpoint bias (increased tip-sample separation), while the conductivity onset shifts towards the Fermi level in low-bias spectra. This trend suggests that the observed variability is caused by

band-bending effects due to the tip-electric field and provides no indication for the metallicity of the rods. Thus, the semi-conducting ZnO-type character of the different nanostructures is safely assured by the vanishing conductance around the Fermi level in STM conductance data.

The O_2 chemical potential adjusted in the last annealing step also governs the optical properties of the oxide. Figure 4.34b shows two STM luminescence spectra taken either on a homogenous ZnO film (black curve) or a nanorod sample (red curve). The measurements were performed by injecting 150 eV electrons (5 nA current) from the STM tip into a preselected oxide region and accumulating the emitted photons for 300s with the CCD detector. The two spectra display a sharp luminesce peak at 373 nm, readily assigned to the band-band recombination in wurtzite ZnO, as discussed in the previous chapters of this thesis. In addition, two peaks at 535 and 730 nm appear in the optical spectra, which have already been assigned to zinc and oxygen vacancies in section 4.3.1, respectively. According to the different sample preparation, the intensity distribution of the two peaks changes. Upon oxygen-rich annealing, the O-vacancy peak is considerably weaker than the emission from Zn vacancies, indicating that Zn defects occur predominately in the oxide lattice. On the other hand, film preparation at low O_2 chemical potential results in a strong oxygen-defect peak at 730 nm, while zinc vacancies only produce a faint shoulder at 535 nm. The intensity ratio of O to Zn vacancy peaks thus provides direct insight into the oxide stoichiometry, proving that nanorod samples are indeed oxygen poor. It is important to highlight that Zn defects cannot fully be eliminated even at very low O_2 chemical potential, as this defect type ensures the charge neutrality in n-type, hence electron rich ZnO.

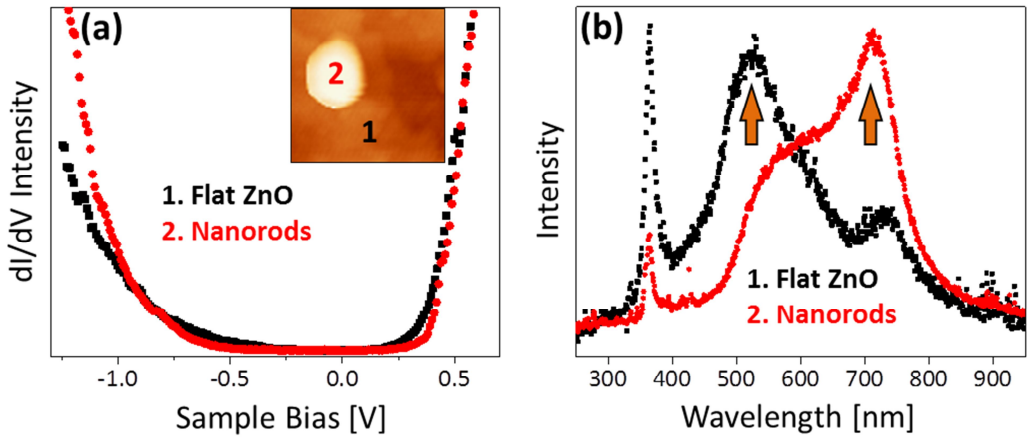

Figure 4.34. (a) STM conductance spectra taken on a single ZnO nanorod and the surrounding flat film. Evidently, both materials have the same chemical identity. (b) STM luminescence spectra of flat ZnO films and films covered with nanorods. Note the different intensities of the 535 and the 730 nm defect peak that are assigned to Zn and O vacancies, respectively.

Based on the presented experimental results, we may conclude that a preferential growth of oxide nanorods takes place normally at low-chemical potentials, whereas flat and homogenous films are formed at oxygen-rich conditions and moderate temperatures. The following scenario aims to explain this behaviour. In our first preparation step, room-temperature deposition of ZnO, a likely amorphous precursor film develops on the Au(111) support. This precursor film does not exhibit any LEED

pattern. Only after annealing in the second step, the Zn and O ions gain sufficient mobility to develop a long-range crystallographic order. Also, the one-to-one stoichiometry of the oxide gets established at this point, a process that involves desorption of excess Zn and dissociation of additional gas-phase O_2 introduced to balance the oxygen loss during heating. The latter process is essential for the final film morphology. At high O_2 chemical potential, enough oxygen is available to saturate all Zn cations and to produce a stoichiometric film exposing the preferred {0001} termination. Information coming from luminescence spectra confirms this idea. The weak oxygen-defect peak with respect to Zn-vacancies clearly indicates that an oxygen surplus in these samples, as depicted in Figure 4.34b (black curve). The situation is different at low O_2 chemical potential, as in this case the oxygen supply becomes the bottleneck for oxide growth. The film contains an abundance of oxygen vacancies, as it can be deduced from the optical spectra [114]. Moreover, the enhanced Zn desorption caused by the lack of oxygen results in a thinning of the film with respect to O_2-rich conditions.

Interestingly, even at O_2-poor conditions the oxygen supply seems sufficient in certain regions of the surface to enable the formation of ZnO nanorods. Traces of Au from the support might help catalysing the oxide growth at these sites. The Au(111) surface features an exceptionally large room-temperature fluxionality due to its dense and highly mobile lattice gas [246]. The diffusing adatoms were already found to be responsible for various surface science phenomena, e.g. the formation of self-assembled thiolate monolayers [247], gold nanofingers [248], or metal-organic complexes [249]. As they have high mobility at 300 K, part of the adatoms remains on the surface during film deposition, while the majority gets buried at the metal-oxide interface. The surface Au species now become active in catalysing further ZnO growth in the final annealing step. Following the vapour-liquid-solid (VLS) mechanism [28, 250], a local alloying of Au and Zn hereby produces a highly active phase for O_2 dissociation, overcoming the lack of oxygen at low O_2 chemical potentials. It should be highlighted at this point that the presence of tiny Au quantities plays no role at high O_2 chemical potentials, when the ZnO growth is not limited by the oxygen supply. At this condition, the oxide film exhibits a layer by layer growth and nanorod formation is of minor importance.

Highly-resolved STM images of individual ZnO nanorods provide indirect evidence for our proposed growth model, as shown in Figure 4.35. On sufficiently large rods, a regular line pattern was detected. This pattern occurs in three domains rotated by 120°. The periodicity of the pattern amounts to 5.5 Å, being twice the spacing of the close-packed O or Zn rows on the {0001} surface. We ascribe this pattern to Au rows that decorate the top facet of the nanorod and might have been involved in catalysing its growth (Figure 4.35c). On the other hand, only a disordered adsorbate phase, but no regular stripe pattern was found on the flat oxide films (Figure 4.35a).

The Au termination of the nanorods fulfils another task. As described in section 4.1.3, the issue of polarity compensation plays an important role in polar oxide films. In this case, the {0001} surfaces of ZnO are polar and the associated dipole moment needs to be cancelled in order to stabilize the 3D islands [251]. As detailed in section 4.2.2, dipole compensation is achieved by generating a surface charge-density σ_{surf} that depends on the bulk charge-density. Mathematically, this fact is described by the following compensation formula [167]:

$$\sigma_{surf} = \sigma_{bulk} \frac{d}{D} . \tag{4.23}$$

Here, *d* and *D* are the Zn-O layer distance (0.63 Å) and the unit cell height of the wurtzite lattice (2.6 Å), respectively. The so calculated surface charge-density, $\sigma_{surf} = +0.5|e|$ might be generated by placing a singly-charged Au ion on every second unit cell, hence producing a 2x1 superstructure, as observed in the STM image shown in Figure 4.35b.

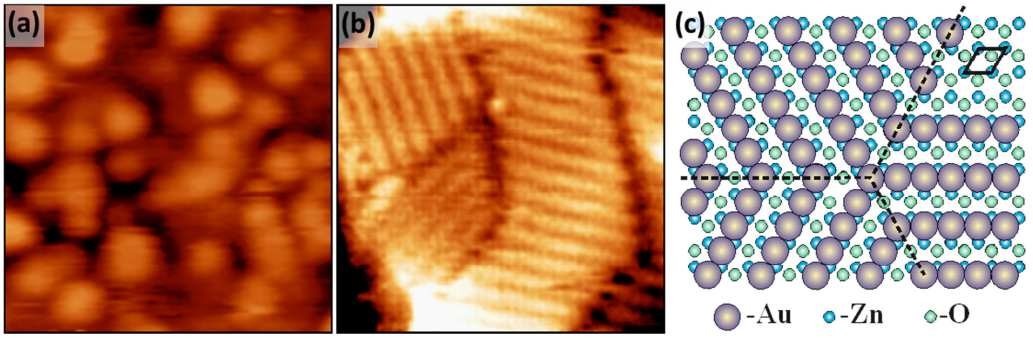

Figure 4.35. (a) High-resolution STM images taken on a flat ZnO film and a nanorod top-facet (Us = 3 V, 6.5x6.5 nm^2). While the flat film exposes a disordered adsorbate phase, made of hydroxyl groups, the nanorod surface shows a characteristic line pattern in three rotational domains. The lines are made of Au atoms, as depicted in the ball model shown in (c).

The actual charge state of the adatoms hereby depends on the stacking sequence of the nanorods. While Au^+ ions would compensate for the polarity of an O-terminated surface, Au^- species should be placed on the Zn-terminated oxide plane. Given the high electronegativity of gold, we consider the latter scenario more likely. It is important to highlight that flat ZnO films were found to be O-terminated [252] and their polarity gets compensated for by a disordered hydrogen ad-layer (Figure 4.35a) [195]. This possibility can be discarded for the top-facets of ZnO rods, which exhibit a corrugation of 2.5 Å, much larger than the one of the hydrogen termination. The large surface corrugation of the nanorods and their mere existence therefore support the idea of an Au-catalysed growth of ZnO on an Au(111) surface.

Finally, since Au is suggested to drive the nanorod formation, we asked the question whether a submonolayer of Au deposited on top of the ZnO film would enhance the formation of the nanorods or not. The result of a typical experiment addressing this topic is shown in Figure 4.36. Right after Au deposition, the surface is characterized by a high density of ultrasmall Au deposits (Figure 4.36a). Their average separation is very small, because Au diffusion is strongly inhibited on the hydroxylated ZnO surface even at room temperature. Upon annealing to 500 K in vacuum, the ad-structures dramatically increase in size, while their number density decreases by an order of magnitude. An obvious explanation is the effect of Ostwald ripening of Au deposits at elevated temperature [253, 254]. However, even a very conservative estimation suggests that the total volume of the deposits has increased. By accounting for the effect of tip convolution, the total volume of the few large deposits on Figure 4.36b has increased by a factor of 5-7 with respect to the many small clusters on Figure 4.36a.

This finding suggests that also at these low temperature conditions (500 instead of 750 K before), ZnO nanorods have formed below the Au particles, increasing the

volume of the ad-structures. Unfortunately, a quantitative analysis of the effect is difficult for the following reasons: *(i)* gold readily desorbs from the surface even at moderate annealing temperatures and we have no means to quantify, how much of the ad-structures in Figure 4.36b is actually made of Au, and *(ii)* we have no means to reach similar growth conditions as for pure ZnO (750 K and higher), due to the low thermal stability of the ad-metal.

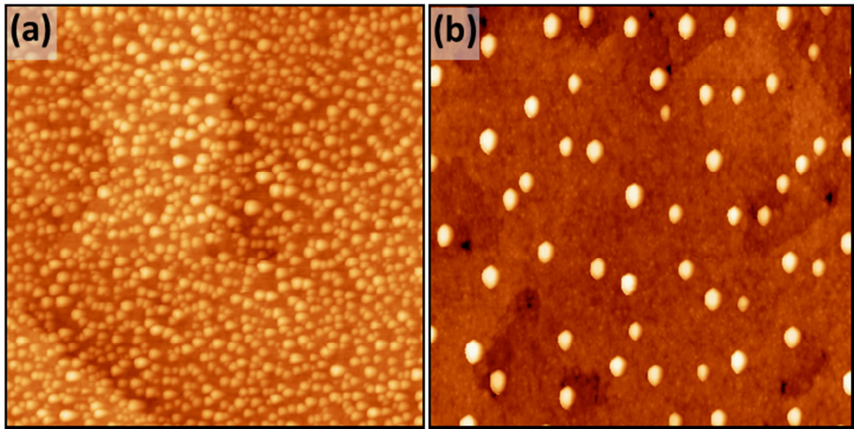

Figure 4.36. (a) ZnO thin film after Au deposition at room temperature and (b) after annealing to 500 K (U_s=3V, 80x80 nm^2). While the number of deposits has decreased from 1.25×10^{13} cm^{-2} to 9×10^{11} cm^{-2}, the total volume of all ad-structures found in image frame has increased by a factor of seven after annealing. The volume estimation is based on a cylindrical shape of the deposits, using height and diameters of the deposits as measured with STM. The latter have been corrected for tip convolution effects. The volume increase in (b) suggests that below the Au deposits ZnO nanorods formation has occurred again, catalyzed by the extra gold on the surface.

However, from the fact that most-likely ZnO containing ad-structures develop at much lower temperature after extra Au deposition, the mechanism described before is clearly promoted, although not on a truly quantity level.

To sum up, we have demonstrated that small changes in the O_2 chemical potential drastically affect the growth of ZnO on an Au(111) support. While a layer by layer growth is observed at oxygen-rich conditions, resulting in flat $(000\bar{1})$-terminated ZnO films, formation of nanorods with large aspect ratio is revealed in an O_2 poor environment. We ascribe this phenomenon to the critical role of the oxygen supply in the high-temperature crystallization step of the oxide. Homogenous films develop only in oxygen excess, while traces of surface gold that help trapping and dissociating the O_2 molecules promote the nanorod growth at oxygen-poor conditions. Indirect evidence for this scenario comes from a distinct line pattern observed on top of the ZnO rods that is compatible with an Au(2×1) ad-layer. In order to confirm the proposed mechanism, the accumulation of gold on the oxide surface needs to be verified either by ion scattering or photoelectron spectroscopy in future.

The growth of ZnO nanorods by physical-vapour deposition in a vacuum environment represents an interesting pathway to fabricate pure nanostructures for optical and catalytic applications. The choice of Au(111) as support material turns out to be particularly suited in this respect, given its high activity in the VLS regime. However, other metal substrates are expected to promote the formation of ZnO nanostructures in a similar way.

Chapter 5

Summary and Outlook

In this work, the impact of the local morphological structure on the optical properties of ZnO(0001) films grown on Au(111) substrates has been studied by means of luminescence spectroscopy with the STM.

In order to investigate the growth of ZnO thin films on a Au(111) support, we have prepared several samples with different amount of deposited oxide. The thickness evolution of the ZnO morphology showed formation of small ZnO nanocrystallites with triangle or hexagonal shape for low material load. For higher loads, a thin film adapting its own lattice parameter was observed right from the beginning. Already at a few-layer thickness, the film developed the wurtzite bulk structure with a small lattice mismatch to the Au(111) support. This mismatch gave rise to a clearly observable Moiré pattern, a situation similar to the known optical effect. Details have been explained by a tetragonal distortion of the wurtzite lattice, in which the vertical parameter was reduced to compensate the film polarity. With increasing film thickness, the Moiré pattern was found to cross over into a homogeneous surface without any long range periodicity. The role of the charge density at the surface has also been discussed and related to the intrinsic polarity of ZnO(0001) and the presence of compensating adsorbates. We also demonstrated that small changes in the O_2 chemical potential drastically affect the growth of ZnO on the gold support. While the formation of nanorods was observed at low chemical potentials, e.g. at vacuum pressures and higher temperatures, flat films develop at high oxygen chemical potential. The effect has been explained by traces of surface gold that help trapping and dissociating the O_2 molecules at oxygen-poor conditions, helping to catalyze the oxide growth as well. Also the electronic structure for both cases, thin films and nanorods, has been analyzed, showing a n-type conductance behavior, coming from hydrogen donor sites in ZnO.

Concerning the optical behaviour, the peaks in the luminescence spectra for ZnO thin films have been measured by STM luminescence spectra on differently prepared samples. The exciton recombination inside the bandgap explains the highest peak in the spectra, which is situated at 373 nm. This peak is the dominant transition in defect-poor materials. Additional peaks come from lattice imperfections that have been intentionally created by different means into the oxide sample. Upon annealing in vacuum, an increase of the intensity at 730 nm was observed. As the temperature effect produces zinc as well as oxygen vacancies in the lattice, we created only oxygen vacancies via two extra methods: photon bombardment with pulsed laser radiation and chemical reduction by exposing the film to atomic hydrogen during growth. Both methods led to an increase of the peak at 730 nm as well, being in agreement with calculations predicting the position of oxygen defect sates in the bandgap with matching energy. The same peak appeared also, with and without nitrogen doping, suggesting that the luminescence cannot be explained with electrons transitions involving the nitrogen doping effects. Instead, oxygen vacancies in the wurtzite lattice are stabilized by the insertion of aliovalent nitrogen ions, enhancing the before

mentioned emission process. A third peak at 535 nm in the luminescence spectra has been assigned to zinc vacancies. These defects have low formation energies due to the necessity to be inserted in the lattice in order to keep the charge balance in the intrinsic n-type structure. Thus, these defects are present with high intensity in almost every preparation, a situation which gives rise to a strong 535 nm peak in almost all spectra. Moreover, our experiments showed a decrease in the 535 nm peak when Zn was co-deposited with the film, confirming our idea. The last of the four peaks that appear in the spectra is the 595 nm emission and has been addressed to two effects: either oxygen interstitials or surface states. The low formation energy of oxygen interstitials grown in O rich conditions calculated by DFT and the fact that this peak is frequently observed in our as grown films supported the first idea. On the other hand, specific surface states might also give arise to a peak at 595 nm. A full explanation for this peak in our films can therefore not be given. In summary, by systematically varying the preparation conditions we were able to identify likely candidates for the underlying lattice defects, which has been the main achievement of this PhD work.

The behaviour of supported metal particles grown on ZnO thin films has also been studied. Particulary interesting is the case of Ag particles that grow with hexagonal shape in the range of a few nanometers in height and width. The plasmon frequencies of silver, corresponding to the in-plane and out-of-plane oscillation modes, have been identified. Upon embedding the particle ensemble into an extra ZnO layer, a coupling between the two systems developed. The plasmon resonance followed the changing dielectric environment, resulting in a red-shift and a broadening of the corresponding peaks. However, we have not observed the expected luminescence enhancement, which should result from energy transfer from plasmonic to excitonic modes. The cover of the particle ensemble seems to be gone after the thermal treatment. Thus, ZnO coatings of larger thickness should be used in the future.

Regarding the SNOM, the primary steps were done within my PhD time. The microscope was able to scan and performed the first steps for the light acquisition, demonstrating the proof of principle of the method in terms of light excitation. Tips were produced and coated as a first approach. However, there is plenty of space for improvements. By means of thermal assisted tip-pulling, less sharp and more reproducible fiber tips may be obtained. Also the coating step should be more reproducible in order to achieve the inset aperture in a controlled way using the same geometry evaporation procedure. In addition, the system should be transferred to a vacuum and low temperature environment in order to allow stable tunneling conditions.

Beyond the capability to probe spatially confined luminescence with the STM to correlate defects, doping and morphological effects, several questions remain open in the ZnO/Au(111) system. An interesting possibility would be the study of p-type doped ZnO films with reproducibility and quality, a fact that has not been achieved so far due to strong self-compensation effects. This might help exploiting the advances of ZnO, as it would facilitate the fabrication of *p-n* heterojunctions and transparent thin film transistors. The STM with its related spectroscopy and its extended configuration to study light emission in a local way would be of extremely importance when addressing such questions in the future.

Bibliography

[1] MOORE, G., *Cramming More Components onto Integrated Circuits.* Electronics Magazine, **1965**, p. 4. Retrieved 2006-11-11.

[2] ERTL, G.; KNÖZINGER, H.; SCHUETH,F.; WEITKAMP,J. (EDS), *Handbook of Heterogeneous Catalysis*. 2008, Weinheim: Wiley-VCH.

[3] TROVARELLI, A., *Catalytic Properties of Ceria and CeO2-Containing Materials.* Catal. Rev.-Sci. Eng. 38, **1996**, p. 439-520.

[4] CONNER, W.; FALCONER, J., *Spillover in Heterogeneous Catalysis.* Chem. Rev. 95, **1995**, p. 759–788.

[5] FREUND, H.-J., *Metal-Supported Ultrathin Oxide Film Systems as Designable Catalysts and Catalyst Supports.* Surf. Sci. 601, **2007**, p. 1438-1442.

[6] FREUND, H.-J, *Oxide Surfaces.* Faraday Discuss. 114, **1999**, p. 1-31.

[7] NILIUS, N., *Properties of Oxide Thin Films and their Adsorption Behaviour Studied by Scanning Tunneling Microscopy and Conductance Spectroscopy.* Surf. Sci. Rep. 64, **2009**, p. 595-659.

[8] NILIUS, N.; ERNST, N.; FREUND,H.-J., *Photon Emission Spectroscopy of Individual Oxide-Supported Silver Clusters in a Scanning Tunneling Microscope.* Phys Rev Lett. 84, **1992**, p. 3994.

[9] SCHROEDER, T.; LEE, T.; ZEGENHAGEN,I.; MAGG,N.; IMMARAPORN,B.; FREUND,H.-J., *Formation of Faceted MoO2 Epilayer on Mo(112) Studied by XPS, UPS and STM.* Surf. Sci. 552, **2004**, p. 85-97.

[10] CARLSSON, A.; NASCHITZKI, M.; BÄUMER,M.; FREUND,H.-J., *The Structure and Reactivity of Al2O3-supported Cobalt-Palladium Particles: A CO-TPD-, STM- and XPS-Study.* J. Phys. Chem. B 107, **2003**, p. 778-785.

[11] KHAN, N.; UHL, A.; SHAIKHUTDINOV,S.; FREUND,H.-J., *Alumina Supported Model Pd-Ag Catalysts: A Combined STM, XPS, TPD and IRAS Study.* Surf. Sci. 600, **2006**, p. 1849-1853.

[12] YULIKOV, M.; STERRER, M.; RISSE,T.; FREUND,H.-J., *Gold Atoms and Clusters on MgO(100) Films; an EPR and IRAS Study.* Surf. Sci. 603, **2009**, p. 1622-1628.

[13] FERNANDEZ-TORRENTE, I.; MONTURET, S.; FRANKE,K.J.; FRAXEDAS,J.; LORENTE,N.; PASCUAL,J.I., *Long-Range Repulsive Interaction between Molecules on a Metal Surface Induced by Charge Transfer.* Phys Rev Lett. 99, **2007**, p. 176103.

[14] FRANKE, K.; PASCUAL, J.I., *Effects of Electron–Vibration Coupling in Transport through Single Molecules.* J. Phys.: Condens. Matter 24, **2012**, p. 394002.

[15] LI, H.; FRANKE, K.J.; PASCUAL,J.I.; BRUCH,L.; DIEHL,R., *Origin of Moiré structures in C60 on Pb(111) and their effect on molecular energy levels.* Phy. Rev. B 80, **2009**, p. 085415.

[16] NILIUS, N., *Diss: Lichemission aus einzelnen oxidgetragenen Metallpartikeln im Rastertunnelmiscroskop*. 2001, Humboldt-Universität zu Berlin: Berlin.

[17] BERNDT, R., *Scanning Probe Microscopy*. Springer Series Nano-science and Technology, ed. Wiesendanger. 1998, Berlin: Springer.

[18] ALVARADO, S; RENAUD, P.; ABRAHAM,D.; SCHÖNENBERGER,C.; ARENT,D.; MEIER,H., *Luminescence in Scanning Tunneling Microscopy on III–V Nanostructures* J. Vac. Sci. Technol. B 9, **1991**, p. 409.

[19] BETZIG, E.; TRAUTMAN, J.; HARRIS,T.; WEINER,J.; KOSTELAK,R., *Breaking the Diffraction Barrier: Optical Microscopy on a Nanometric Scale.* Science 251, **1991**, p. 1468-1470.

[20] HECHT, B.; SICK, B.; WILD,U.; DECKERT,V.; ZENOBI,R.; MARTIN,O.; POHL,D., *Scanning Near-field Optical Microscopy with Apertures Probes: Fundamentals and Applications.* Journal of Chemical Physics 112(18), **2000**, p. 7761-7774.

[21] HARTSCHUH, A., *Tip-Enhanced Near-Field Optical Microscopy.* Angew. Chem. Int. Ed. 47, **2008**, p. 8178-8191.

[22] FORTUNATO, E.; BARQUINHA, P.; MARTINS,R., *Oxide Semiconductor Thin-Film Transistors: a Review of Recent Advances.* Adv. Mater. 24, **2012**, p. 2945.

[23] FORTUNATO, E.; BARQUINHA, P.; PIMENTEL,A.; GONÇALVES,A.; MARQUES,A.; MARTINS,R.; PEREIRA,L., *Wide-Bandgap High-Mobility ZnO Thin-Film Transistors Produced at Room Temperature.* App. Phys. Lett. 85, **2004**, p. 2541.

[24] LEVY, D.; FREEMAN, D.; NELSON,S.; COWDERY-CORVAN,P.; IRVING,L. , *Stable ZnO Thin Film Transistors by Fast Open Air Atomic Layer Deposition.* App. Phys. Lett. 92, **2008**, p. 192101

[25] MA, A.; GUPTA, M.; AFSHAR,A.; SHOUTE,G.; TSUI,Y.; CADIEN,K.; BARLAGE,D., *Schottky Barrier Source-Gated ZnO Thin Film Transistors by Low Temperature Atomic Layer Deposition.* Appl. Phys. Lett. 103, **2013**, p. 253503.

[26] JANOTTI, A.; VAN DE WALLE, C. G., *Native Point Defects in ZnO.* Phys. Rev. B 76, **2007**, p. 165202.

[27] KLINGSHIRN, C., *ZnO: From Basics towards Applications.* Phys. Stat. Sol (b) 9, **2007**, p. 3027-3073.

[28] OZGUR, U.; ALIVOV, Y.I.; LIU,C.; TEKE,A.; RESHCHIKOV,M.A.; DOGAN,S.; AVRUTIN,V.; CHO,S.J.; MORKOC,H., *A Comprehensive Review of ZnO Materials and Devices.* J. Appl. Phys. 98, **2005**, p. 041301.

[29] SELIM, F.A.; WEBER, M.H.; SOLODOVNIKOV,D.; LYNN,K.G., *Nature of Native Defects in ZnO.* Phys Rev Lett. 99, **2007**, p. 085502.

[30] KIM, J.; YU, J.; KIM,T.; JEONG,T.; YOUN,C.; HONG,K., *Electric-Field Effect of Near-Band-Edge photoluminescence in Bulk ZnO.* J. Mater. Sci. 45, **2010**, p. 4036-4039.

[31] TON-THAT, C.; WESTON, L.; PHILLIPS,M.R., *Characteristics of Point Defects in the Green Luminescence from Zn- and O-rich ZnO.* Phys. Rev. B 86, **2012**, p. 115205.

[32] BINNING, G.; ROHER, H.; GERBER,C.; WEIBEL,E., *Surface Studies by Scanning Tunneling Microscopy.* Phys. Rev. Lett. 49, **1982**, p. 57-61.

[33] WIESENDANGER, R., *Scanning Probe Microscopy and Spectroscopy: Methods and Aplications*. 1994, Cambridge: Cambridge University Press.

[34] WIESENDANGER, R., *Scanning Tunneling Microscopy and Spectroscopy: Analytical Methods*. 1998, Berlin, Heidelberg: Springer Verlag.

[35] CHEN, J.C., *Introduction to Scanning Tunneling Microscopy*. 1993, New York, Oxford: Oxford University Press.

[36] STIPE, B.; REZAEI, M.A; HO,W., *Single Molecule Vibrational Spectroscopy and Microscopy.* Science 280, **1998**, p. 1732

[37] LEE, H..J..; HO, W., *Single-Bond Formation and Characterization with a Scanning Tunneling Microscope.* Science 286, **1999**, p. 1719-1722.

[38] PASCUAL, J.I.; JACKIW, J.J.; SONG,Z.; WEISS,P.S.; CONRAD,H.; RUST,H.-P., *Adsorbate-Substrate Vibrational Modes of Benzene on Ag(110) Resolved with Scanning Tunneling Spectroscopy.* Phys. Rev. Lett. 86, **2001**, p. 1050-1053.

[39] PASCUAL, J.I; LORENTE, N.; SONG,Z.; CONRAD,H.; RUST,H.-P., *Selectivity in Vibrationally Mediated Single-Molecule Cemistry.* Nature 423, **2003**, p. 525-528.

[40] WIESENDANGER, R., *Spin Mapping at the Nanoscale and Atomic Scale.* Rev. Mod. Phys. 81, **2009**, p. 1495-1550.

[41] WIESENDANGER, R.; GÜNTHERODT, H.J.; GÜNTHERODT,G.; GAMBINO,J.R ; RUF,R., *Observation of Vacuum Tunneling of Spin-Polarized Electrons with the Scanning Tunneling Microscope.* Phys. Rev. Lett 65, **1990**, p. 247-250.

[42] WIESENDANGER, R.; SHVETS, I.V.; BÜRGLER,D.; TARRACH,G.; GÜNTHERODT,H..J.; COEY,J.; GRÄSER,S., *Topographic and Magnetic-Sensitive Scanning Tunneling Microscope Study of Magnetite.* Science 255, **1992**, p. 583.

[43] BODE, M., *Spin-Polarized Scanning Tunneling Microscopy.* Rep. Prog. Phys. 66, **2003**, p. 523-582.

[44] FRANKE, K.J.; SCHULZE, G.; PASCUAL,J.I, *Competition of Superconducting Phenomena and Kondo Screening at the Nanoscale.* Science 332, **2011**, p. 940-944.

[45] FERNÁNDEZ-TORRENTE, I.; FRANKE, K.J.; PASCUAL,J.I., *Vibrational Kondo Effect in Pure Organic Charge-Transfer Assemblies.* Phys Rev Lett. 101, **2008**, p. 217203.

[46] LIPPMAA, H.; KAWASAKI, M.; OHTOMO,A.; SATO,T.; IWATSUKI,M.; KOINUMA,H., *Observation of SrTiO Step Edge Dynamics by Real-Time High-Temperature STM.* App. Surf. Sci. 130, **1998**, p. 582.

[47] KAMBARA, H.; MATSUI, T.; NIIMI,Y.; FUKUYAMA,H., *Construction of a Versatile Ultralow Temperature Scanning Tunneling Microscope.* Rev. Sci. Inst. 78, **2007**, p. 073703.

[48] MOUSSY, N.; COURTOIS, H.; PANNETIER,B, *A Very Low Temperature Scanning Tunneling Microscope for the Local Spectroscopy of Mesoscopic Structures.* Rev. Sci. Inst. 72, **2001**, p. 128-131.

[49] GURNEY, R.W.; CONDON, E.U., *Wave Mechanics and Radioactive Desintegration.* Nature 122, **1928**, p. 439-439.

[50] MYRACH, P., *Diss: Metal Particles on Thin MgO Films: Morphological and Optical Properties*. 2011, Technische Universität Berlin: Berlin.

[51] BENIA, H. M., *Diss: Spatially Resolved Optical Measurements on Supported Metal Particles and Oxide Surfaces with the STM*. 2008, Humboldt-Universität zu Berlin.

[52] WU, Q. H. ;KANG, J., *Applications of Fast Scanning Tunneling Microscopy: A Review.* Mat. Manufac. Proc. 22, **2007**, p. 22-27.

[53] BESENBACHER, F. ; LAEGSGAARD, E. ; STENSGAARD,I., *Fast-Scanning STM Studies.* Mater. Today 8, **2005**, p. 26-30.

[54] BESENBACHER, F., *Dynamics and Self-Assembly of Organic Molecules on Surfaces Revealed by High-Resolution, Fast-Scanning STM.* J. Bio. Technol. 118, **2005**, p. 33-34.

[55] BARDEEN, J., *Tunneling From a Many Particle Point of View.* Phys. Rev. Lett. 6, **1961**, p. 57.

[56] TERSOFF, J., *Theory and Application for the Scanning Tunneling Microscope.* Phys. Rev. Lett. 50, **1983**, p. 1998.

[57] TERSOFF, J. , *Theory of the Scanning Tunneling Microscope.* Phys. Rev. B 31, **1985**, p. 805.

[58] NAZIN, G.V.; QIU, X. H.; HO,W., *Atomic Engineering of Photon Emission with a Scanning Tunneling Microscope.* Phys. Rev. Lett. 90, **2003**, p. 216110-1

[59] HOFFMANN, G.; MAROUTIAN, T.; BERNDT,R., *Color View of Atomic Highs and Lows in Tunneling Induced Light Emission.* Phys. Rev. Lett. 93, **2004**, p. 076102-1.

[60] STROZECKA, A.; LI, J.; SCHÜRMANN,R.; SCHULZE,G.; CORSO,M.; SCHULZ,F.; LOTZE,C.; SADEWASSER,S.; FRANKE,K.J.; PASCUAL,J.I., *Electroluminescence of Copper Nitride Nanocrystals.* Phys. Rev. B 90, **2014**, p. 195420.

[61] BERNDT, R.; GIMZEWSKI, J., *Inelastic Tunneling Excitation of Tip-Induced Plasmon Modes on Noble-Metal Surfaces.* Phys. Rev. Lett. 67(27), **1991**, p. 3796-3799.

[62] JOHANSSON, P.; MONREAL, R., *Theory for Photon Emission from a Scanning Tunneling Microscope.* Z. Phys. B – Condensed Matter 84, **1991**, p. 269.

[63] IRIE, H.; WATANABE, Y.; HASHIMOTO,K., *Nitrogen-Concentration Dependence on Photocatalytic Activity of TiO2−xNx Powders.* J. Phys. Chem. B. 107, **2003**, p. 5483 – 5486.

[64] OREGAN, B.; GRÄTZEL, M., *A Low-Cost, High-Efficiency Solar-Cell Based on Dye-Sensitized Colloidal TiO2 Films.* Nature 353(6346), **1991**, p. 737 – 740.

[65] LAMBE, J. ; MCCARTHY, S.L., *Light Emission from Inelastic Electron Tunneling.* Phys. Rev. Lett. 37(14), **1976**, p. 923–925.

[66] GIMZEWSKI, J.K.; REIHL, B.; COOMBS,J.H.; SCHLITTLER,R.R., *Photon Emission with the Scanning Tunneling Microscope.* Zeitschr. Phys. B - Cond. Mat. 72, **1988**, p. 497–501.

[67] GIMZEWSKI, J., *Enhanced Photon-Emission in Scanning Tunneling Microscopy.* Europhysics Letters 8(5), **1989**, p. 435–440.

[68] JOHANSSON, P.; MONREAL, R.; APELL,P, *Theory for Light Emission from a Scanning Tunneling Microscope.* Phys. Rev. B 42(14), **1990**, p. 9210–9213.

[69] ADAMS, A.; HANSMA, P. K., *Light Emission from Small Metal Particles and Thin Metal Films Excited by Tunneling Electrons.* Phys. Rev. B 23, **1981**, p. 3597–3601.

[70] JOHANSSON, P., *Light Emission From a Scanning Tunneling Microscope: Fully Retarded Calculation.* Phys. Rev. B 58(16), **1998**, p. 10823–10834.

[71] TAKEMORI, T., *Optical-Response of a Sphere Coupled to a Metal-Substrate.* J. Phys. Soc. Japan 56(4), **1987**, p. 1587–1602.

[72] AIZPURUA, J.; APELL, S.P.; BERNDT,R., *Role of Tip Shape in Light Emission from the Scanning Tunneling Microscope.* Phys. Rev. B 62, **2000**, p. 2065.

[73] KREIBIG, U.; VOLLMER, W., *Optical Properties of Metal Clusters*. Springer Series Materials Science. Vol. 25. 1995, Berlin: Springer.

[74] BARATOFF, A.; PERSSON, B., *Theory of Photon Emission in Electron Tunneling to Metal Particles.* Phys. Rev. Lett. 68, **1992**, p. 3224.

[75] NILIUS, N.; ERNST, N.; FREUND,H.-J., *Tip Influence on Plasmon Excitations in Single Gold Particles in an STM.* Phys. Rev. B 65, **2002**, p. 115421.

[76] MIE, G., *Beiträge zur Optik trüber Medien, speziell kolloidaler Metallösungen.* Ann. Phys. 25, **1908**, p. 377.

[77] FELDHEIM, D.; FOSS, C., *Metal Nanoparticles: Synthesis, Characterization and Aplications*, ed. Dekker. 2001, New York.

[78] ROYER, P; GOUDONNET, J.P.; WARMACK,R.; FERELL,T., *Substrate Effects on Surface-Plasmon Spectra in Metal-Island Films.* Phys. Rev. B 35, **1987**, p. 3753.

[79] ROYER, P.; BIJEON, J.; GOUDONNET,J.P.; INAGAKI,P.; ARAKAWA,E., *Optical Absorbance of Silver Oblate Particles: Substrate and Shape Effects.* Surf. Sci. 217, **1989**, p. 384.

[80] FOSS, C.A.; HORNYAK, G.L.; STOCKERT,J.A.; MARTIN,C.R., *Template-Synthesized Nanoscopic Gold Particles: Optical Spectra and the Effects of Particle Size and Shape.* J. Phys. Chem. B. 98, **1994**, p. 2963.

[81] BERNDT, R.; GIMZEWSKI, J.K.; JOHANSSON,P., *Electromagnetic Interactions of Metallic Objects in Nanometer Proximity.* Phys. Rev. Lett. 71, **1993**, p. 3493.

[82] HOFFMANN, G.; AIZPURUA, J.; APELL,P.; BERNDT,R., *Influence of Tip Geometry in Light Emission from The Scanning Tunneling Microscope.* Surf. Sci. 482-485, **2001**, p. 1159-1162.

[83] MEGURO, K.; SAKAMOTO, K.; ARAFUNE,R.; SATOH,M.; USHIODA,S., *Origin of Multiple Peaks in The Light Emission Spectra of a Au(111) surface induced by The Scanning Tunneling Microscope.* Phys. Rev. B. 65, **2002**, p. 165405.

[84] HALL, E., *The Penetration of Totally Reflected Light into the Rarer Medium.* Phys. Rev. 15(2), **1902**, p. 73-106.

[85] EICHENWALD, A., *Über der Energie bei Totalreflexion.* Ann. Phys. 35, **1911**, p. 1037.

[86] ARZELIES, H., *La reflexion vitreuse.* Ann. Phys. (Paris) 1, **1946**, p. 5-69.

[87] COURJON, D., *Near-Field Microscopy and Near-Field Optics*. 2003: Imperial College Press.

[88] BORN, M.; WOLF, E., *Principles of Optics*. Sixth Edition ed. 1980, Oxford: Pergamon Press.

[89] NOVOTNY, L.; HECHT, B., *Principles of Nano-Optics*. 2006, Cambrigde, UK: Cambridge University Press.

[90] ABBE, E., *The Relation of Aperture and Power in the Microscope.* Journal of Royal Microscopy Society 3, **1883**, p. 790-812.

[91] SYNGE, E., *A Suggested Method for Extending Microscopic Resolution into the Ultra-Microscopic Region.* Philos. Mag 6, **1928**, p. 356.

[92] SYNGE, E., *A Microscopic Method.* Philos. Mag. 11, **1931**, p. 65.

[93] BINNING, G.; ROHER, H., *Scanning Tunneling Microscopy.* Helv. Phys. Acta 55, **1982**, p. 726.

[94] POHL, D.; DENK, W.; LANZ,M., *Optical Stethoscopy: Image Recording with Resolution λ/20.* Appl. Phys. Lett. 44, **1984**, p. 651.

[95] DÜRIG, U.; POHL, D.; ROHNER,F., *Near-Field Optical-Scanning Microscopy.* J. App. Phys. 59, **1986**, p. 3318.

[96] POHL, D., US4, Editor. 1986, 604, 520.

[97] LEWIS, A.; ISAACSON, M.; HAROOTUNIAN,A.; MURAY,A., *Development of a 500 Å Spatial Resolution Light Microscope: I. Light is Efficiently Transmitted Through λ/16 Diameter Apertures.* Ultramicroscopy 13, **1984**, p. 227.

[98] HAROOTUNIAN, A.; BETZIG, E.; ISAACSON,M.; LEWIS,A., *Super-Resolution Fluorescence Near-Field Scanning Optical Microscopy.* App.Phys. Lett. 49, **1986**, p. 674.

[99] BETZIG, E.; ISAACSON, M.; LEWIS,A., *Collection Mode Near-Field Scanning Optical Microscopy.* App. Phys. Lett. 51, **1987**, p. 2088.

[100] HEINZELMANN, H.; HECHT, B.;NOVOTNY,L.; POHL,D., *Forbidden Light Scanning Near-Field Optical Microscopy.* J. Microsc. 177, **1994**, p. 115.

[101] HECHT, B., HEINZELMANN,H.; POHL,D., *Combined Aperture SNOM/PSTM: Best of Both Worlds?* Ultramicroscopy 57, **1995**, p. 228.

[102] FISCHER, U.; POHL, D., *Observation of Single-Particle Plasmons by Near-Field Optical Microscopy.* Physical Rewiev Letters 62, **1989**, p. 458.

[103] FISCHER, U.; POHL, D., *Observation of Single-Particle Plasmons by Near-Field Optical Microscopy.* Phys. Rev. Lett. 62, **1989**, p. 458.

[104] ZENHAUSERN, F.; MARTIN, Y.; WICKRAMASINGHE,H., *Scanning Interferometric Apertureless Microscopy: Optical Imaging at 10 Angstrom Resolution* Science 269, **1995**, p. 1083.

[105] KOGLIN, J.; FISCHER, U.; FUCHS,H., *Scanning Near-Field Optical Microscopy with a Tetrahedral Tip at a Resolution of 6 nm.* J. Biomed. Opt. 1, **1996**, p. 75.

[106] TURNER, D., *US Patent*. 1984, 4,469,554.

[107] HOFFMAN, P.; DUTOIT, B.; SALATHÉ,R.-P., *Comparison of Mechanically Drawn and Protection of Layer Chemically Etched Optical Fiber Tips.* Ultramicroscopy 61, **1995**, p. 165.

[108] STÖCKLE, R.; FOKAS, C.; DECKERT,V.; ZENOBI,R.; SICK,B.; HECHT,B.; WILD,U.P., *High-Quality Near-Field Optical Probes by Tube Etching.* Appl. Phys. Lett. 75, **1999**, p. 160.

[109] LAMBELET, P.; SAYAH, A.; PFEFFER,M.; PHILIPONA,C.; MARQUIS-WEIBLE,F., *Chemically etched fiber tips for near-field optical microscopy: a process for smoother tips.* Appl. Opt. 37, **1998**, p. 7289.

[110] BERNDT, R.; GIMZEWSKI, J., *The Role of Proximity Plasmon Modes on Noble Metal Surfaces in Scanning Tunneling Microscopy.* Surf. Sci. 269, **1991**, p. 556-559.

[111] *Basic Diffraction: Waves, Interference and Reciprocal Space*. Available from: http://www-structmed.cimr.cam.ac.uk/Course/Basic_diffraction/Diffraction.html.

[112] IBACH, I; LÜTH, H., *Solid-State Physics*. 2003, Berlin, Heidelberg: Springer-Verlag.

[113] STAVALE, F.; PASCUA, L.; NILIUS,N.; FREUND,H.-J., *Morphology and Luminescence of ZnO Films Grown on a Au(111) Support.* J. Phys. Chem. C 117, **2013**, p. 10552-10557.

[114] STAVALE, F.; NILIUS, N.; FREUND,H.-J., *STM Luminescence Spectroscopy of Intrinsic Defects in ZnO(000Ī) Thin Films.* J. Phys. Chem. Lett. 4, **2013**, p. 3972−3976.

[115] STAVALE, F.; PASCUA, L.; NILIUS,N.; FREUND,H.-J., *Luminescence Properties of Nitrogen-Doped ZnO.* J. Phys. Chem. C 118, **2014**, p. 13693−13696.

[116] PASCUA, L.; STAVALE, F.; NILIUS,N.; FREUND,H.-J., *Preparation and Analysis of Silver-ZnO Hybrid Systems: A STM and Cathodoluminescence Study.* In Preparation, **2015**.

[117] PASCUA, L.; STAVALE, F.; NILIUS,N.; FREUND,H.-J., *Autocatalytic Growth of ZnO Nanorods From Flat Au(111)-Supported ZnO Films* Phys. Chem. Chem. Phys. DOI: 10.1039/C4CP03730H, **2014**.

[118] LOOK, D.C., *Recent Advances in ZnO Materials and Devices.* Mat. Sci. Eng. B-.Adv. 80, **2001**, p. 383–387.

[119] YAN, R.; GARGAS, D.; YANG,P., *Nanowire Photonics.* Nature Photonics 3, **2009**, p. 569.

[120] JANOTTI, A.; VAN DE WALLE, C.G., *Fundamentals of Zinc Oxide as a Semiconductor.* Rep. Prog. Phys. 72, **2009**, p. 126501.

[121] MANG, A.; REIMANN, K.; RÜBENACKE,ST., *Band Gaps, Crystal-Field Splitting, Spin-Orbit Coupling, and Exciton Binding Energies in ZnO under Hydrostatic Pressure.* Solid State Commun. 94, **1995**, p. 251.

[122] REYNOLDS, D.C, LOOK,D.C.; JOGAI,B., *Optically Pumped Ultraviolet Lasing from ZnO.* Solid State Commun. 99, **1996**, p. 873.

[123] BAGNALL, D. M.; CHEN, Y. F.; ZHU,Z.; YAO,T..; KOYAMA,S.; SHEN,M. Y.; GOTO,T., *Optically Pumped Lasing of ZnO at Room Temperature.* Appl. Phys. Lett. 70, **1997**, p. 2230.

[124] CAO, H.; ZHAO, Y.G.; HO,S.T.; SEELIG,E.W.; WANG,Q.H.; CHANG,R.P., *Random Laser Action in Semiconductor Powder.* Phys. Rev. Lett. 82, **1999**, p. 2278.

[125] HUANG, M.H.; MAO, S.; FEICK,H.; YAN,H.; WU,Y.; KIND,H.; WEBER,E.; RUSSO,R.; YANG,P., *Room-Temperature Ultraviolet Nanowire Nanolasers.* Science 292, **2001**, p. 1897-1899.

[126] SRIKANT, V.; CLARKE, D.R., *On the Optical Band Gap of Zinc Oxide.* J. Appl. Phys. 83, **1998**, p. 5447.

[127] NANTO, H.; SOKOOSHI, H.; USUDA,T., *Smell Sensor Using Zinc Oxide Thin Films Prepared by Magnetron Sputtering.* Solid-State Sensors and Actuators 596, **1991**, p. 24-27.

[128] SCHMIDT, O.; KIESEL, P.; VAN DE WALLE,C.G.; JOHNSON,N.M.; NAUSE,J.; DÖHLER,G., *Effects of an Electrically Conducting Layer at the Zinc Oxide Surface* Japan. J. Appl. Phys. Part 1 44, **2005**, p. 7271.

[129] LOOK, D.C., *Quantitative Analysis of Surface Donors in ZnO.* Surf. Sci. 601, **2007**.

[130] EDA, K., *Zinc Oxide Varistors* Electr. Insul. Mag. IEEE 5(6), **1989**, p. 28.

[131] LARCIPRETE, M.; HAERTLE, D.; BELARDINI,A.; BERTOLOTTI,M.; SARTO,F.; GÜNTER,P., *Characterization of Second and Third Order Otical Nonlinearities of ZnO Sputtered Films.* Appl. Phys. B 82, **2006**, p. 431.

[132] FLORESCU, D.; MOUROKH, L.; POLLAK,F.; LOOK,D.; CANTWELL,G.; LI,X., *High Spatial Resolution Thermal Conductivity of Bulk ZnO (0001).* J. Appl. Phys. 91, **2002**, p. 890.

[133] LOOK, D.; HEMSKY, J.; SIZELOVE,J., *Residual Native Shallow Donor in ZnO.* Phys. Rev. Lett. 82, **1999**, p. 2552.

[134] TUOMISTO, F.; SAARINEN, K.; LOOK,D.C.; FARLOW,G.C., *Introduction and Recovery of Point Defects in Electron-Irradiated ZnO.* Phys. Rev. B 72, **2005**, p. 085206.

[135] SPENCER, M.S., *The Role of Zinc Oxide in Cu/ZnO Catalysts for Methanol Synthesis and the Water–Gas Shift Reaction.* Top. Cat. 8, **1999**, p. 259-266.

[136] WIKIPEDIA. *ZnO*. Available from: http://en.wikipedia.org/wiki/Zinc_oxide.

[137] PHILLIPS, J.C., *Bands and Bonds in Semiconductors*, ed. Alper. 1973, New York Academic Press.

[138] GIRARD, R.; TJERNBERGA, O.; CHIAIAA,G.; SÖDERHOLMA,S.; KARLSSONA,U.; WIGRENB,C.; NYLÉNB,H.; LINDAUB,I., *Electronic Structure of ZnO(0001) Studied by Angle-Resolved Photoelectron Spectroscopy.* Surf. Sci. 373, **1997**, p. 409-417.

[139] SCHRÖER, P.; KRÜGER, P.; POLLMANN,J., *First-Principles Calculation of the Electronic Structure of the Wurtzite Semiconductors ZnO and ZnS.* Phys. Rev. B 47, **1993**, p. 6971.

[140] WIKIPEDIA. *Brillouin Zone*. Available from: http://en.wikipedia.org/wiki/Brillouin_zone.

[141] WANG, Y., *High Resolution Electron Energy Loss Spectroscopy on Perfect and Defective Oxide Surfaces.* Z. Phys. Chem. 222, **2008**, p. 927−966.

[142] MEYER, B.; MARX, D., *Density-Functional Study of Cu Atoms, Monolayers, Films, and Coadsorbateson Polar ZnO Surfaces.* Phys. Rev. B 69, **2004**, p. 235420.

[143] WANG, Y.; MEYER, B.; YIN,X.; KUNAT,M.; LANGENBERG,D.; TRAEGER,F.; BIRKNER,A.; WÖLL,CH., *Hydrogen Induced Metallicity on the ZnO(10$\bar{1}$ 0) Surface.* Phys. Rev. Lett. 95, **2005**, p. 266104.

[144] KING, S.T.; PARIHAR, S.S.; PRADHAN,K.; JOHNSON-STEIGELMAN,H. T.; LYMAN,P.F., *Observation of a (√3 × √3)R30° Reconstruction on O-Polar ZnO Surfaces.* Surf. Sci. Lett. 602, **2008**, p. L131−L134.

[145] PARKER, T.M.; CONDON, N.G.; LINDSAY,R.; LEIBSLE,F.M.; THORNTON,G., *Imaging the Polar (000$\bar{1}$) Source and Non-polar (10$\bar{1}$0) Source Surfaces of ZnO with STM.* Surf. Sci. 415, **1998**, p. L1046−L1050.

[146] KITTEL, C., *Introduction to Solid State Physics*, ed. Wiley. 1976, New York.

[147] VAN DE WALLE, C.G.; NEUGEBAUER, J. , *First-Principles Calculations for Defects and Impurities: Applications to III-Nitrides.* J. Appl. Phys. 95, **2004**, p. 3851.

[148] HANADA, T., *Oxide and Nitride Semiconductors*. Advances in Material Research. Vol. 12. 2009.

[149] PNKOVE, J.; JOHNSON, N., *Hydrogen in Semiconductors, Semiconductors and Semimetals*. Vol. 34. 1991, Boston: Boston Academic.

[150] VAN DER WALLE, C.; NEUGEBAUER, J., *Hydrogen in Semiconductors.* Annu. Rev. Mater. Res 36, **2006**, p. 179-198.

[151] JANOTTI, A.; VAN DE WALLE, C.G., *Hydrogen Multicentre Bonds.* Phy. Rev. B 6, **2007**, p. 44.

[152] KOBAYASHI, A.; SANKEY, O.F.; DOW,J.D., *Deep Energy Levels of Defects in the Wurtzite Semiconductors AIN, CdS, CdSe, ZnS, and ZnO.* Phys. Rev. B 28, **1983**, p. 946-956.

[153] LOOK, D.C.; REYNOLDS, D.C.; LITTON,C.W.; JONES,R.L.; EASON,D.B.; CANTWELL,G., *Characterization of Homoepitaxial P-type ZnO Grown by Molecular Beam Epitaxy.* Appl. Phys. Lett. 81, **2002**, p. 1830.

[154] LIU, L.; XU, J.; WANG,D.; JIANG,M.; WANG,S.; LI,B.; ZHANG,Z.; ZHAO,D.; SHAN,C.-X.; YAO,B.; SHEN,D. Z., *P-Type Conductivity in N-Doped ZnO: The Role of the NZn-VO Complex.* Phys. Rev. Lett. 108, **2012**, p. 215501.

[155] VARLEY, J.B.; JANOTTI, A.; FRANCHINI,C.; VAN DE WALLE,C.G., *Role of Self-trapping in Luminescence and P-type Conductivity of Wide-band-gap Oxides.* Phys. Rev. B 85, **2012**, p. 081109.

[156] LYONS, J. L.; JANOTTI, A.; VAN DE WALLE,C.G., *Why Nitrogen Cannot Lead to P-type Conductivity in ZnO.* Appl. Phys. Lett. 95, **2009**, p. 252105.

[157] TARUN, M.C.; ZAFAR IQBAL, M.; MCCLUSKEY,M.D., *Nitrogen is a Deep Acceptor in ZnO.* AIP Advances 1, **2011**, p. 022105.

[158] LEBANON, G.; BRUCKSTEIN, A. *Energy Minimization Methods in Computer Vision and Pattern Recognition*. in *Third International Workshop, EMMCVPR 2001*. 2001. Sophia Antipolis, France: Springer.

[159] TUSCHE, C.; MEYERHEIM, H.L.; KIRSCHNER,J, *Observation of Depolarized ZnO(0001) Monolayers: Formation of Unreconstructed Planar Sheets.* Phys. Rev. Lett. 99, **2007**, p. 026102.

[160] YANG, G.H.; LIU, G.Y., *New Insights for Self-Assembled Monolayers of Organothiols on Au(111) Revealed by Scanning Tunneling Microscopy.* J. Phys. Chem. B 107, **2003**, p. 8746−8759.

[161] WEIRUM, G.; BARCARO, G.; FORTUNELLI,A.; WEBER,F., SCHENNACH,R.; SURNEV,S.; NETZER,F.P., *Growth and Surface Structure of Zinc Oxide Layers on a Pd(111) Surface.* J. Phys. Chem. C 114, **2010**, p. 15432-15446.

[162] BENEDETTI, S.; TORELLI, P.; VALERI,S.; BENIA,H.M.; NILIUS,N.; RENAUD,G., *Structure and Morphology of Thin MgO Films on Mo(001).* Phys. Rev. B 78, **2008**, p. 195411.

[163] GONIAKOWSKI, J.; GIORDANO, L.; NOGUERA,C., *Polarity of Ultrathin MgO(111) Films Deposited on a Metal Substrate* J. Phys. Rev. B 81, **2010**, p. 205404.

[164] DAVIS, T.J.; VERNON, K.C.; GOMEZ,D.E., *Designing Plasmonic Systems Using Optical Coupling Between Nanoparticles.* Phys. Rev. B 79, **2009**, p. 155433.

[165] GONIAKOWSKI, J.; NOGUERA, C.; GIORDANO,L., *Prediction of Uncompensated Polarity in Ultrathin Films.* Phys. Rev. Lett. 98, **2007**, p. 205701.

[166] PAN, Y.; BENEDETTI, S.; VALERI,S.; NOGUERA,C.; GIORDANO,L.; GONIAKOWSKI,J.; NILIUS,N., *Compensating Edge Polarity: A Means To Alter the Growth Orientation of MgO Nanostructures on Au(111).* J. Phys. Chem. C 116, **2012**, p. 11126–11132.

[167] GONIAKOWSKI, J.; FINOCCHI, F.; NOGUERA,C., *Polarity of Oxide Surfaces and Nanostructures.* Rep. Progr. Phys. 71, **2008**, p. 016501-016556.

[168] OSTENDORF, F.; TORBRÜGGE, S.; REICHLING,M., *Atomic Scale Evidence for Faceting Stabilization of a Polar Oxide Surface.* Phys. Rev. B 77, **2008**, p. 041405(R).

[169] DULUB, O.; DIEBOLD, U.; KRESSE,G., *Novel Stabilization Mechanism on Polar Surfaces: ZnO(0001)-Zn.* Phys. Rev. Lett. 90, **2003**, p. 016102.

[170] WANG, Z.L, *Zinc Oxide Nanostructures: Growth, Properties and Applications.* J. Phys.: Condens. Matter 16, **2004**, p. R829-R858.

[171] DULUB, O.; MEYER, B.; DIEBOLD,U., *Observation of the Dynamical Change in a Water Monolayer Adsorbed on a ZnO Surface.* Phys. Rev. Lett. 95, **2005**, p. 136101.

[172] DULUB, O.; BOATNER, L.A..; DIEBOLD,U., *STM Study of the Geometric and Electronic Structure of ZnO(0001)-Zn, (0001)-O, (1010), and (1120) Surfaces.* Surf. Sci. 519, **2002**, p. 201-217.

[173] DU, M.-H.; BISWAS, K., *Anionic and Hidden Hydrogen in ZnO.* Phys. Rev. Lett. 106, **2011**, p. 115502.

[174] QIU, H.; MEYER, B.; WANG,Y.; WÖLL,C., *Ionization Energies of Shallow Donor States in ZnO Created by Reversible Formation and Depletion of H Interstitials.* Phys. Rev. Lett. 101, **2008**, p. 236401.

[175] SHAO, X.; NILIUS, N.; FREUND,H.-J., *Li/Mo Codoping of CaO Films: A Means to Tailor the Equilibrium Shape of Au Deposits.* J. Am. Chem. Soc. 134, **2012**, p. 2532-2534.

[176] GIMZEWSKI, B., *Inelastic Tunneling Excitation of Tip-Induced Plasmon Modes on Noble-Metal Surfaces.* Phys. Rev. Lett. 67, **1991**, p. 3796-3799.

[177] ZHANGL, B.P.; BINHL, N.T.; SEGAWA,Y.; KASHIWABA,Y.; HAGA,K., *Photoluminescence Study of ZnO Nanorods Epitaxially Grown on Sapphire (110) Substrates.* Appl. Phys. Lett. 84, **2004**.

[178] VANHEUSDEN, K.; WARREN, W.L.; SEAGER,C.H.; TALLANT,D.R.; VOIGT,J.A.; GNADE,B.E., *Mechanisms behind Green Photoluminescence in ZnO Phosphor Powders.* J. Appl. Phys. 79, **1996**, p. 7983-7990.

[179] LI, Y.; CHENG, G.S.; ZHANG,L.D., *Fabrication of Highly Ordered ZnO Nanowire Arrays in Anodic Alumina Membranes.* J. Mater. Res. 15, **2000**, p. 2305-2308.

[180] LIN, X.; HE, X.B.; YANG,T.Z.; GUO,W.; SHI,D.X.; GAO,H.-J.; MA,D.D.D.; LEE,S.T.; LIU,F.; XIE,X.C., *Intrinsic Current-Voltage Properties of Nanowires with Four-Probe Scanning Tunneling Microscopy: A Conductance Transition of ZnO Nanowire.* Appl. Phys. Lett. 89, **2006**, p. 043103-043105.

[181] GORLA, C.R.; EMANETOGLU, N.W.; LIANG,S.; MAYO,W.E.; LU,Y.; WRABACK,M.; SHEN,H., *Structural, Optical, and Surface Acoustic Wave Properties of Epitaxial ZnO Films Grown on (01math2) Sapphire by Metalorganic Chemical Vapor Deposition.* J. Appl. Phys. 85, **1999**, p. 2595-2603.

[182] TAKATA, S.; MINAMI, T.; NANTO,H., *DC EL in Annealed Thin Film of Sputtered ZnO.* Jpn. J. Appl. Phys. 20, **1981**, p. 1759-1762.

[183] TANAKA, S.; TAKAHASHI, K.; SEKIGUCHI,T.; SUMINO,K.; TANAKA,J., *Cathodoluminescence from Fractured Surfaces of ZnO Varistors.* J. Appl. Phys. 77, **1995**, p. 4021-4024.

[184] KNUTSEN, K. E.; GALECKAS, A.; ZUBIAGA,A.; TUOMISTO,F.; FARLOW,G.C.; SVENSSON,B.G.; KUZNETSOV,A.YU., *Zinc Vacancy and Oxygen Interstitial in ZnO Revealed by Sequential Annealing and Electron Irradiation.* Phys. Rev. B 86, **2012**, p. 121203.

[185] JANOTTI, A.; VAN DE WALLE, C. G., *Oxygen Vacancies in ZnO.* Appl. Phys. Lett. 87, **2005**, p. 122102.

[186] PALA, R.; METIU, H., *Oxygen-Vacancy Formation in Doped ZnO Very Thin Films.* J. Phys. Chem. C. 111, **2007**, p. 12715-12722.

[187] DUPUIS, A.-C.; ABU-HAIJA, M.; RICHTER,B.; KUHLENBECK,H.; FREUND,H.-J., *V2O3(0001) on Au(111) and W(110): Growth, Termination and Electronic Structure.* Surf. Sci. 539, **2003**, p. 99-112.

[188] TREVISANUTTO, P.E.; SUSHKO, P.V.; SHLUGER,A.; BECK,K.M.; HENYK,M.; JOLY,A.G.; HESS,W.P. , *A Mechanism of Photo-Induced Desorption of Oxygen Atoms from MgO Nano-Crystals.* Surf. Sci. 593, **2005**, p. 210-220.

[189] STERRER, M.; DIWALD, O.; KNOZINGER,E.; SUSHKO,P.V.; SHLUGER,A.L., *Energies and Dynamics of Photoinduced Electron and Hole Processes on MgO Powders.* J. Phys. Chem. B. 106, **2002**, p. 12478-12482.

[190] BERGER, T.; STERRER, M.; DIWALD,O.; KNÖZINGER,E., *The Color of the MgO Surface A UV/Vis Diffuse Reflectance Investigation of Electron Traps.* J. Phys. Chem. B. 108, **2004**, p. 7280-7285.

[191] KNUDSEN, J.; MERTE, L.R.; GRABOW,L. C.; EICHHORN,F. M.; PORSGAARD,S.; ZEUTHEN,H., VANG,R.T.; LÆGSGAARD,E.; MAVRIKAKIS,M.; BESENBACHER,F., *Reduction of FeO/Pt(111) Thin Films by Exposure to Atomic Hydrogen.* Surf. Sci. 604, **2010**, p. 11-20.

[192] EVANS, S. M.; GILES, N. C.; HALLIBURTON,L. E.; KAPPERS,L. A., *Further Characterization of Oxygen and Zinc Vacancies in Electron-Irradiated ZnO.* J. Appl. Phys. 103, **2008**, p. 043710.

[193] SHALISH, I.; TEMKIN, H.; NARAYANAMURTI,V., *Size-Dependent Surface Luminescence in ZnO Nanowires.* Phy. Rev. B 69, **2004**, p. 245401.

[194] SUSHKO, P.V.; SHLUGER, A.L., *Electronic Structure of Excited States at Low-Coordinated Surface Sites of MgO.* Surf. Sci. 421, **1999**, p. L157-L176.

[195] LAURITSEN, J.V. ET AL., *Stabilization Principles for Polar Surfaces of ZnO.* ACS Nano 5, **2011**, p. 5987-5994.

[196] TORBRÜGGE, S.; OSTENDORF, F.; REICHLING,M., *Stabilization of Zinc-Terminated ZnO(0001) by a Modified Surface Stoichiometry.* J. Phys. Chem. C 113, **2009**, p. 4909-4914.

[197] LAUTENSCHLAEGER, S. ET AL, *Optical Signatures of Nitrogen Acceptors in ZnO.* Phys. Rev. B 85, **2012**, p. 235204.

[198] KRÖGER, F.A.; VINK, H.J., *Relations between the Concentrations of Imperfections in Crystalline.* Solids Solid State Physics 3, **1956**, p. 307-435.

[199] MYRACH, P.; NILIUS, N.; LEVCHENKO,S. ; GONCHAR,A.; RISSE,T.; DINSE,K.-P.; BOATNER,L.A.; FRANDSEN,W.; HORN,R.; FREUND,H.-J.; SCHLÖGL,R.; SCHEFFLER,M., *Temperature-Dependent Morphology, Magnetic and Optical Properties of Li-doped MgO.* ChemCatChem 2, **2010**, p. 854-862.

[200] YE, Z.Z.; CHEN, L.L.; ZHAO,B.H..; HE,H.P., *Photoluminescence in Heavily Doped ZnO:N:In Films.* Appl. Phys. Lett. 92, **2008**, p. 231913.

[201] CHE, M., BENNETT,C.O., *The Influence of Particle Size on the Catalytic Properties of Supported Metals.* Adv. Catal. 36, **1989**, p. 55-172.

[202] BÄUMER, M.; FREUND, H.-J., *Metal Deposits on Well-ordered Oxide Films.* Prog. Sur. Sci. 61, **1999**, p. 127-198.

[203] POPPA, H., *Nucleation, Growth, and TEM Analysis of Metal Particles and Clusters Deposited in UHV.* Catal. Rev.-Sci. Eng. 35, **1993**, p. 359.

[204] ZINKE-ALLMANG, M.; FELDMAN, L.C.; GRABOW,M., *Clustering on Surfaces.* Surf. Sci. Rep. 16, **1992**, p. 377.

[205] VAN CAMPEN, D.; HRBEK, J., *Silver on Alumina: Adsorption and Desorption Study of Model Catalysts.* J. Phys. Chem. 99, **1995**, p. 16389–16394.

[206] XU, X; GOODMAN, D. , *Metal Deposition onto Oxides: An Unusual Low Initial Sticking Probability for Copper on SiO2.* Appl. Phys. Lett. 61, **1992**, p. 1799.

[207] VENABLES, J.A.; SPILLER, G.; HANBÜCKEN,M., *Nucleation and Growth of Thin Films.* Rep. Prog. Phys. 47, **1984**, p. 399.

[208] CAMPBELL, C.T., *Ultrathin Metal Films and Particles on Oxide Surfaces: Structural, Electronic and Chemisorptive Properties.* Surf. Sci. Rep. 27, **1997**, p. 1.

[209] GOODMAN, D., *Model Catalysts: From Extended Single Crystals To Supported Particles.* Surf. Rev. Lett. 2, **1995**, p. 9.

[210] DIEBOLD, U.; PAN, J.; MADEY,T., *Ultrathin Metal Film Growth on TiO2(110): an Overview.* Surf. Sci. 331-333, **1995**, p. 845.

[211] HENRY, C.R., *Surface Studies of Supported Model Catalysts.* Surf. Sci. Rep. 31, **1998**, p. 231.

[212] CHATAIN, D.; COUDURIER, L.; EUSTATHOPOULOS,N., *Wetting and Interfacial Bonding in Ionocovalent Oxide-Liquid Metal Systems* Rev. Phys. Appl. 23, **1998**, p. 1055.

[213] PEDEN, C.; KIDD, K.; SHINN,N., *Metal/Metal-Oxide Interfaces: A Surface Science Approach to the Study of Adhesion* J. Vac. Sci. Technol. A 9, **1991**, p. 1518.

[214] NOGUERA, C., *Physics and Chemistry at Oxide Surfaces*. 1996, Cambridge: University Press.

[215] OULTON, R.F.; SORGER, V.J.; ZENTGRAF,T.; MA,R.M.; GLADDEN,C.; DAI,L.; BARTAL,G.; ZHANG,X., *Plasmon Lasers at Deep Subwavelength Scale.* Nature 461, **2009**, p. 629-632.

[216] HILL, M.; MARELL, M.; LEONG,E.; SMALBRUGGE,B.; ZHU,Y.; SUN,M.; VELDHOVEN,P.J.; GELUK,E.; KAROUTA,F.; OEI,Y.; NOTZEL,R.; NING,C.Z.; SMIT,M.K., *Lasing in Metal-Insulator-Metal Sub-Wavelength Plasmonic Waveguides.* Opt Express 17, **2009**, p. 11107-11112.

[217] XIAO, X.; REN, F.; ZHOU,X.; PENG,T.; WU,W.; PENG,X.; YU,X.; JIANG,C., *Surface Plasmon-Enhanced Light Emission Using Silver Nanoparticles Embedded in ZnO.* Appl Phys Lett 97, **2010**, p. 071909.

[218] CHEN, T.; XING, G.; ZHANG,Z.; CHEN,H.; WU,T., *Tailoring the Photoluminescence of ZnO Nanowires Using Au Nanoparticles.* Nanotechnology 19, **2008**, p. 435711.

[219] PARK, J.Y.; YUN, Y.S.; HONG,Y.S.; OH,H.; KIM,J.J.; KIM,S.S., *Synthesis, Electrical and Photoresponse properties of Vertically Well-Aligned and Epitaxial ZnO Nanorods on GaN-Buffered Sapphire Substrates.* Appl. Phys. Lett. 87, **2005**, p. 123108.

[220] ZHANG, Y.; JIA, H.; WANG,R.; CHEN,C.; LUO,X.; YU,D.; LEE,C. , *Low-Temperature Growth and Raman Scattering Study of Vertically Aligned ZnO Nanowires on Si Substrate.* Appl. Phys. Lett. 83, **2003**, p. 4631.

[221] BENEDETTI, S; MYRACH, P.; DI BONA,A.; VALERI,S.; NILIUS,N.; FREUND,H.-J., *Growth and Morphology of Metal Particles on MgO/Mo(001): A Comparative STM and Diffraction Study.* Phys. Rev. B 83, **2011**, p. 125423-1-10.

[222] HANSEN, K.; WORREN, T.; STEMPEL,S.; LÆGSGAARD,E.; BÄUMER,M.; FREUND,H.-J.; BESENBACHER,F.; STENSGAARD,I., *Palladium Nanocrystals on Al2O3: Structure and Adhesion Energy.* Phys. Rev. Lett. 83, **1999**, p. 4120.

[223] LIDE, D.R., *CRC Handbook of Chemistry and Physics*, ed. Press. 2010, FL.

[224] BROWN, M.; FUJIMORI, Y.; RINGLEB,F.; SHAO, X.; STAVALE, F.; NILIUS, N.; STERRER, M.; FREUND, H.-J., *Oxidation of Au by Surface OH: Nucleation and Electronic Structure of Gold on Hydroxylated MgO(001).* J. Amer. Chem. Soc. 133, **2011**, p. 10668-10676.

[225] PALIK, E.D., *Handbook of Optical Constants of Solids* 1985, Orlando: Academic.

[226] ROY, R.K.; BANDYOPADHYAYA, S; PAL,A.K., *Surface Plasmon Resonance in Nanocrystalline Silver in a ZnO Matrix.* Eur. Phys. J. B 39, **2004**, p. 491-498.

[227] SU, L.; QIN, N.; XIE,W.; FU,J.; BAO,D. , *The Surface-Plasmon-Resonance and Band Bending Effects on the Photoluminescence Enhancement of Ag-Decorated ZnO Nanorods.* J. App. Phys. 116, **2014**, p. 063108.

[228] JIMÉNEZ, J.; LYSENKO, S.; LIU,H. , *Photoluminescence Via Plasmon Resonance Energy Transfer in Silver Nanocomposite Glasses* J. App. Phys. 104, **2008**, p. 054313.

[229] SCHLESINGER, R.; XU, Y.; HOFMANN,O.; WINKLER,S.; FRISCH,J.; NIEDERHAUSEN,J.; VOLLMER,A.; BLUMSTENGEL, S.; HENNEBERGER,F.; RINKE,P.; SCHEFFLER,M.; KOCH,N., *Controlling the Work Function of ZnO and the Energy-Level Alignment at the Interface to Organic Semiconductors with a Molecular Electron Acceptor.* Phys. Rev. B 87, **2013**, p. 155311.

[230] XU, S.; WANG, Z.L., *One-Dimensional ZnO Nanostructures: Solution Growth and Functional Properties.* Nano. Res. 4, **2011**, p. 1013–1098.

[231] DING, Y.; KONG, X.Y.; WANG,Z.L., *Doping and Planar Defects in the Formation of Single-Crystal ZnO Nanorings.* Phy. Rev. B 70, **2004**, p. 235408.

[232] HUANG, M. ; WU, Y.; FEICK,H.; TRAN,N.; WEBER,E.; YANG,P., *Catalytic Growth of Zinc Oxide Nanowires by Vapor Transport.* Adv. Mater. 13, **2001**, p. 113-116.

[233] WAGNER, R.; ELLIS, W., *Vapor-Liquid-Solid Mechanism of Single Crystal Growth* Appl. Phys. Lett. 4, **1964**, p. 89.

[234] WESTWATER, J.; GOSAIN, D.; TOMIYA,S.; USUI,S.; RUDA,H., *Growth of Silicon Nanowires via Gold/Silane Vapor–Liquid–Solid Reaction.* J. Vac. Sci. Technol. B 15, **1997**, p. 554.

[235] MORALES, A.; LIEBER, C., *A Laser Ablation Method for the Synthesis of Crystalline Semiconductor Nanowires.* Science 279 **1998**, p. 208-211.

[236] GAO, P.; WANG, Z., *Self-Assembled Nanowire−Nanoribbon Junction Arrays of ZnO.* J. Phys. Chem. B 106, **2002**, p. 12653.

[237] JIN, X.; STRUEBEN, J.; HEEPE,L.; KOVALEV,A.; MISHRA,Y.; ADELUNG,R.; GORB,S.; STAUBITZ,A., *Joining the Un-joinable: Adhesion Between Low Surface Energy Polymers Using Tetrapodal ZnO Linkers.* Advances Materials DOI: 10.1002/adma201201780, **2012**.

[238] HASHIMOTO, S.; YAMAGUCHI, A., *Growth Morphology and Mechanism of a Hollow ZnO Polycrystal.* J. Am. Ceram. Soc. 79, **1996**, p. 1121.

[239] PAN, Z.; DAI, Z.; WANG,Z *Nanobelts of Semiconducting Oxides.* Science 291, **2001**, p. 1947.

[240] SINGH, D.P., *Synthesis and Growth of ZnO Nanowires.* Sci. Adv. Mat. 2, **2010**, p. 245-272.

[241] YAP, Y.K. *Nanowires, Nanobelts, and Novel Nanostructures*. Available from: http://www.phy.mtu.edu/yap/nnnn.html.

[242] BATYREV, E.; VAN DEN HEUVEL, J.C., *Modification of the ZnO(0001)–Zn Surface Under Reducing Conditions.* Phys. Chem. Chem. Phys. 13, **2011**, p. 13127-13134.

[243] MEYER, B.; MARX, D.; DULUB,O.; DIEBOLD,U.; KUNAT,M.; LANGENBERG,D.; WÖLL,C., *Partial Dissociation of Water Leads to Stable Superstructures on the Surface of Zinc Oxide.* Angew. Chem. Int. Ed. 43, **2004**, p. 6641.

[244] LIU, D.; XIANG, Y.; LIAO,Q.; ZHANG,J.P.; WU,X.; ZHANG,Z.; LIU,L.; MA,W.; SHEN,J.; ZHOU,W.; XIE,S., *A Simple Route to Scalable Fabrication of Perfectly Ordered ZnO Nanorod Arrays* Nanotechnology 18, **2007**, p. 405303.

[245] ALBERTY, R., *Physical Chemistry*. Sixth ed. 1983: John Wiley & Sons.

[246] POIRIER, G.; PYLANT, E., *The Self-Assembly Mechanism of Alkanethiols on Au(111).* Science 272, **1996**, p. 1145-1148.

[247] YU, M.; BOVET, N.; SATTERLEY,C.; BENGIO,S.; LOVELOCK,K.; MILLIGAN,P.; JONES,R.; WOODRUFF,D.; DHANAK,V., *True Nature of an Archetypal Self-Assembly System: Mobile Au-Thiolate Species on Au(111).* Phys. Rev. Lett. 97, **2006**, p. 166102.

[248] YIN, F.; PALMER, R.; GUO,Q., *Critical Stability of Gold Nanofingers on a Zero-Gradient Stepped Surface*. J. Phys.: Condens. Matter 21, **2009**, p. 445001.

[249] YANG, B.; LIN, X.; PAN,Y.; NILIUS,N.; FREUND,H.-J.; HULOT,C.; GIRAUD,A.; BLECHERT,S.; TOSONI,S.; SAUER,J., *Stabilizing Gold Adatoms by Thiophenyl Derivates: A possible Route Towards Metal Redispersion.* J. Am. Chem. Soc. 134, **2012**, p. 11161–11167.

[250] WANG, X.; SUMMERS, C.; WANG,Z., *Large-Scale Hexagonal-Patterned Growth of Aligned ZnO Nanorods for Nano-optoelectronics and Nanosensor Arrays.* Nano Lett. 4, **2004**, p. 423–426.

[251] STAEMMLER, V.; FINK, F.; MEYER,B.; MARX,D.; KUNAT,M.; GIROL,S.; BURGHAUS,U.; WÖLL,C., *Stabilization of Polar ZnO Surfaces: Validating Microscopic Models by Using CO as a Probe Molecule.* Phys. Rev. Lett. 90, **2003**, p. 106102.

[252] FREUND, H.-J.; NILIUS, N.; RISSE,T.; SCHAUERMANN,S.; SCHMIDT,T., *Innovative Measurement Techniques in Surface Science.* ChemPhysChem 12, **2011**, p. 79.

[253] BOISTELLE, R ; ASTIER, J.P., *Crystallization Mechanisms in Solution.* J Cryst. Growth 90, **1988**, p. 14-30.

[254] OSTWALD, W., *Studien über die Bildung und Umwandlung fester Korper.* Z. Phys. Chem. 22, **1897**, p. 289.

List of Figures

Curriculum Vitae

For reasons of data protection, the curriculum vitae is not included in the online version.

List of Publications

1. Stavale,F.; Pascua,L.; Nilius,N.; Freund,H.-J. *From Embedded Nanoislands to Thin Films: Tophographic and Optical Properties of Eropium Oxide on MgO(001) Films*. Phys. Rev. B 86, **2012**, p. 085448.
2. Stavale,F.; Pascua,L.; Nilius,N.; Freund,H.-J., *Morphology and Luminescence of ZnO Films Grown on a Au(111) Support.* J. Phys. Chem. C 117, **2013**, p. 10552-10557.
3. Stavale,F.; Pascua,L.; Nilius,N.; Freund,H.-J., *Luminescence Properties of Nitrogen-Doped ZnO.* J. Phys. Chem. C 118, **2014**, p. 13693−13696.
4. Pascua,L.; Stavale, F.; Nilius, N.; Freund,H.-J., *Autocatalytic Growth of ZnO Nanorods From Flat Au(111)-Supported ZnO Films*. Phys. Chem. Chem. Phys. DOI: 10.1039/C4CP03730H, **2014**.
5. Pascua,L.; Stavale,F.; Nilius,N.; Freund,H.-J., *Preparation and Analysis of Silver-ZnO Hybrid Systems: An STM and Cathodoluminescence Study*. In Preparation, **2015**.

Conferences Contributions

1. IMPRS Workshop on Nanoscience and Technology: *Preparation and Characterization of ZnO Thin Films grown on Au(111).* Halle, Germany, 2012.
2. 12th International Conference on Atomically Controled Surfaces, Interfaces and Nanostructures: *Preparation and Characterization of ZnO Thin Films grown on Au(111)*. Tsukuba, Japan, 2012.

Acknowledgements

I would like to thank everybody who contributed to the success of this thesis.

First of all I would like to thank Herr Prof. Dr. Hans-Joachim Freund for trusting me and giving me the oportunity to do a PhD work in physics in spite of my engineering background. I would like to thank him also for providing all the means necessary to perform the experiments for this thesis and for his scientific guidiance. Besides, I would like to express my great respect and esteem for his person, for his wide knowledge, experience and kindness.

I am very thankful to Frau Prof. Dr. Katharina Franke for agreeing to referee this thesis and for giving me the opportunity to present the progress of my work in her research seminar.

I am deeply grateful to Herr Prof. Dr. Niklas Nilius for his truly tireless support throughout all stages of this thesis, particularly for keeping doing it after moving out of the institute. I want to thank him for the nice time I spent working with him during my PhD and for his patience and kindness.

I would like to thank Herr Dr. Markus Heyde for his support and useful advices, particularly in the last stage of the experimental work of this thesis.

I would like to thank particulary Herr Dr. Fernando Stavale for the nice and productive colaboration we made together and for all the concepts he taught me concerning experimental details when I was just a starter PhD student. Also many thanks to and Klaus Peter Vogelgesang for his kindness and support for practical issues in the every day life in the laboratory.

My next thanks are dedicated to the International Max Planck Reseach School (IMPRS) and its members. I particulary want to thank Frau Bettina Menzel for her lovely kindness and her uncountable advices for my stay in Berlin.

Particular thanks from my side go to Herr Christian Stiehler and Herr Emre Emmez, who were colleagues at the beginning and turned to be closed friends along my time at the institute. For their company, support and advices in both professional and personal fields I am profoundly thankful.

I would like to remark the guidance of two of my former supervisors in Argentina, Frau Dr. Liliana Fraigi and Frau Laura Malatto, who supported and encouraged me with the idea to make doctoral studies in physics being engineer.

Last but not least I would like to thank the members of my present swimming team “BSV Medizin Marzahn”, in particular Herr Alex Hänsel und Herr René Asmus. Their passionate support in competitions as well as in dialy training sesions were really a way to keep a balance, contributing namely directly to achieve concentration and therefore to the success of this thesis.

Selbständigkeitserklärung

Hiermit erkläre ich, die vorliegende Arbeit selbständig verfasst und nur unter Verwendung der angegebenen Literatur und Hilfsmittel angefertigt zu haben.

Berlin, den 23.04.2015

Leandro Pascua Arcusin